An infrared/submillimetre perspective on Active Galactic Nuclei

Annemieke Janssen

München 2016

An infrared/submillimetre perspective on Active Galactic Nuclei

Annemieke Janssen

Dissertation
an der Fakultät für Physik
der Ludwig–Maximilians–Universität
München

vorgelegt von
Annemieke Janssen
aus Delft

München, den 27. Oktober 2016

Zusammenfassung

Die vorliegende Dissertation gibt einen Einblick in Aktive Galaktische Kerne (AGN) im ferninfraroten / sub-millimeter Wellenlängenbereich. Es werden zwei Aspekte behandelt: Die Möglichkeit, den molekularen Torus über hochangeregte CO Rotationsübergänge zu detektieren, und die Diagnostik molekularer Materieausströme (outflows) mit Hilfe von OH, [CII] und CO Spektren.

Hochangeregte CO Rotationslinien entstehen in dichten und warmen Regionen und könnten Rückschlüsse auf das den AGN umgebende Gas erlauben, welches für die Absorption der Röntgenstrahlung des AGN verantwortlich ist. Ob dies mittels Übergängen wie CO(40-39) möglich ist wurde an Hand von Beobachtungen des Compton-dichten AGN NGC 1068 untersucht. Eine tiefe Beobachtung mit dem Instrument 'Photodetector Array Camera and Spectrometer' (PACS) an Bord des 'Herschel Space Observatory' ergab aber eine Nicht-Detektion dieser Linie. Die Erklärung liefert ein Strahlungstransport-Modell der von Röntgenstrahlung dominierten Regionen: Unter der Annahme eines für AGN typischen Röntgenspektrums ist die CO(40-39) Linie erst hell genug um beobachtbar zu sein wenn das Gas eine Säulendichte von $N_{\mathrm{H}} \approx 10^{25}\,\mathrm{cm}^{-2}$ erreicht. Enthält das Gas aber auch Staub, absorbiert dieser bei einer so hohen Säulendichte die CO(40-39) Emission vollständig. Hochangeregte CO Rotationslinien erscheinen daher zur Torus-Diagnostik eher ungeeignet.

Das zweite Thema betrifft molekulare Materieausströme auf Galaxien-Skala in nahen Ultraleuchtkräftige Infrarot-Galaxien (ULIRGs). Die Entdeckung und Charakterisierung molekularer Materieausströme spielt eine entscheidende Rolle für das Verständnis der Galaxienentwicklung. Die 22 ULIRGs in unserer Stichprobe sind Verschmelzungen zweier gasreicher Galaxien, die aktiv Sterne formen und Aktive Kerne haben. Die meisten Objekten haben Materieausströme die sich schnell bewegen ($> 1000\,\mathrm{km\,s^{-1}}$ in OH $119\,\mu\mathrm{m}$) und die auf Grund ihrer hohen Geschwindigkeit und dem Verhältnis von Geschwindigkeit zu AGN-Helligkeit vom Aktiven Kern angetrieben werden müssen. Wir untersuchen ob sich die Materieausströme auch in einer Verbreitung der Basis der Feinstruktur-Linie von ionisiertem Kohlenstoff [CII] bei $158\,\mu\mathrm{m}$ widerspiegeln. 14 von 22 Objekten weisen eine solche breite Basis auf. Wenn nur die Objekte verglichen werden, die sowohl einen Materieausstrom in OH119 als auch in [CII] besitzen, finden wir sowohl eine Korrelation der Ausströmgeschwindigkeiten in [CII] und OH119, als auch der Massen. Wir schliessen daraus, dass [CII] die molekularen Materienausströme gut repräsentiert, was besonderes nützlich ist bei hohen Rotverschiebung, wo die CO(1-0) und OH119 Linien schwieriger zu

beobachten sind.

ULIRG IRAS F08572+3915 ist eine ULIRG mit einem besonderes schnellen und massereichen molekularen Materienausstrom. Wir analysieren diese Galaxie im Detail und verwenden dazu hochaufgelöste CO(1-0) Beobachtungen mit NOEMA (früher auch bekannt als 'Plateau de Bure Interferometer'). Das Objekt zeigt einen bi-konischen Materienausstrom, ausgerichtet entlang der kinematischen Hauptachse der Galaxien-Scheibe. Möglicherweise bewegt sich der Materieausstrom an der Scheibe entlang und trennt dabei Gas ab. Räumlich aufgelöste Beobachtungen von Na I D, Hα and warmem H$_2$ zeigen, dass die atomaren und ionisierten Phasen des Ausstroms mit dem molekularen Ausstrom überlappen. Die CO Beobachtungen zeigen auch einen zweiten Materieausstrom etwa 6 kpc von der Galaxie entfernt. Wenn auch dieser Materieausstrom vom Aktiven Kern angetrieben wurde, bedeutet dies eine Variabilität des AGN auf einer Zeitskala von einigen Megajahren. Der zweite Materieausstrom verlangsamt sich mit einer Rate von $\sim$ $300\,\mathrm{km\ s^{-1}\,kpc^{-1}}$, möglicherweise als Folge der Gravitationskraft und der Abwesenheit eines konstanten Antriebs.

Abstract

This thesis presents a Far Infrared / submillimeter view on local Active Galactic Nuclei (AGN). Two aspects are discussed: the potential to detect the molecular torus through high rotational transitions in CO, and the driving of molecular outflows.

High-J CO lines arise from dense and warm regions, and could therefore trace the gas around AGN that is hold responsible for absorbing the X-rays from the AGN. Whether this is possible with lines as high as CO(40-39), was tested on the nearby Compton-thick AGN NGC 1068. A deep observation with the Photodetector Array Camera and Spectrometer (PACS) onboard the Herschel Space Observatory resulted in a non-detection of CO(40-39). A radiative transfer model of X-ray dominated regions clarifies the non-detection: with an X-ray input spectrum typical of AGN, the CO(40-39) line only reaches the detection limit at a column density $N_{\mathrm{H}} \approx 10^{25}\,\mathrm{cm}^{-2}$. If any dust is present in the gas, it will absorb the CO(40-39) emission over such a large column density. Very high CO rotational lines are therefore not ideal tracers of AGN tori.

The second topic concerns galaxy-scale molecular outflows in local Ultra Luminous Infrared Galaxies (ULIRGs). The 22 ULIRGs in our sample are gas-rich mergers with active star formation and AGN activity. Most of these sources have fast ($> 1000\,\mathrm{km\ s}^{-1}$) outflows as detected in OH $119\,\mu$m, thought to be AGN-driven based on their high velocity and their relation between outflow velocity and AGN luminosity. Here it is investigated whether these outflows are traced well through broad wings in the [CII] fine structure line at $158\,\mu$m. Fourteen out of 22 objects show broad wings in [CII]. Taking only those objects with an outflow detected in both [CII] and OH119, we find a trend between two outflow velocities, as well as between the outflow masses derived from both tracers. We conclude that [CII] is a good tracer of molecular outflows. This is particularly useful at high redshift, where other tracers like OH119 and CO(1-0) are harder to observe.

IRAS F08572+3915 is one of the ULIRGs which has a particularly fast and massive molecular outflow. It is studied here in more detail, using high spatial resolution observations of CO(1-0) which were taken with NOEMA (formerly known as Plateau de Bure Interferometer). We find that the source hosts a biconical outflow, aligned with the kinematic major axis of the disk. Possibly the outflow is coplanar, stripping gas off the disk. Spatially resolved observations of Na I D, Hα and warm H$_2$ show that the atomic and ionized gas overlap with the molecular outflow. The CO observations also reveal a second outflow, at about 6 kpc from the galaxy. If this is an AGN-driven outflow as well, it would imply AGN variability over time-scales of a few megayears. The outflow is slowing down

at a rate of $\sim 300\,\mathrm{km\ s^{-1}\,kpc^{-1}}$, perhaps as result of gravitational pull and the absence of a driving mechanism.

Contents

List of Figures

List of Tables

Chapter 1

Introduction

In the optical, galaxies appear as a large collection of stars. Some galaxies, however, contain a compact region in their center, which emits radiation that can not be attributed to stars. Some other, highly energetic, process must be going on. These galaxies are said to harbour an 'Active Galactic Nucleus' (AGN)[1].

AGN were discovered in the early twentieth century, through broad optical emission lines with widths of several thousand kilometers per second (Seyfert (1943), although there were several earlier detections). In the early times of AGN-related research, Woltjer (1959) estimated that 4% of the spiral galaxies (Sa and Sb) contain an AGN. Based on these 4% one may have concluded that AGN are a rare phenomenon, and not relevant for the galaxy population as a whole. However, with the growing insight that AGN are powered by gas accretion onto Super Massive Black Holes (SMBHs), and that (probably) all galaxies contain a SMBH in their center, it becomes clear that in principle every galaxy may go through active phases during its evolution.

1.1 Active Galactic Nuclei

AGN are compact regions in the centers of galaxies, and are called 'active' because they can produce enough radiation to outshine the entire host galaxy. They are the result of gas accretion onto Super Massive Black Holes (SMBH): black holes with masses of 10^6-10^{10} $M_\odot$, which reside in the centers of galaxies (Kormendy & Ho, 2013; McConnell & Ma, 2013). Potentially all galaxies contain a central SMBH, but it is not possible to prove this for each individual galaxy because it requires the presence of a visible tracer (like a gas cloud or a star) at parsec-scale from the black hole. Every galaxy that contains a SMBH could in principle go through 'active phases' (when the galaxy would be classified as an AGN) and 'quiescent phases' (when the galaxy would be classified as a normal galaxy). How frequent are these active phases, or in other words, what is the incidence of AGN among galaxies? The answer depends strongly on the AGN tracer that is used and on the redshift of the

---

[1]Information for the introduction is taken from the following books: Burton et al. (1992); Peterson (1997); Lawson (2000); Tielens (2005); Netzer (2013)

galaxy, but ranges from a few % to as high as ~ 40 % if also the galaxies with enhanced low-ionization lines in their centers (LINERs) are interpreted as AGN (Ho, 2008). With the universe's age of about 10^{10} years and an incidence of 10%, this implies on average a total duty cycle of $\sim 10^9$ years.

1.1.1 Mechanism

The primary emission from the AGN is thought to arise from an accretion disk around the SMBH. Gas in the vicinity of the black hole first has to lose angular momentum before it can approach the black hole and form an accretion disk. There are both internal 'secular' and external processes that may help driving the gas toward the central black hole, like galaxy mergers and galactic bars. Once in the disk, part of the gas loses more angular momentum through viscosity, with the result that it is driven further toward the black hole in which it will finally disappear. Emission from the accretion disk is the most direct way to see this process. Depending on the black hole mass, the disk radiation peaks in the Ultra Violet (UV; $\sim$ 100-300 nm) or X-rays. For a black hole mass of $10^8\,M_\odot$, the disk's radiation peaks in the soft X-ray regime (around 0.1 keV or 13 nm). However, some photons inverse Compton scatter to higher energies, by fast electrons in the hot corona surrounding the disk.

1.1.2 Observables

Because the UV light is easily absorbed by dust, and can arise from star formation as well as from an AGN, AGN surveys often select their targets in the X-rays. But the AGN initiates several other observable processes, with a wide range of physical scales and wavelengths.

Starting close to the accretion disk, these are:

- Broad optical lines (like C IV $\lambda\lambda$1548, 1551, Hα, Lyα, Si IV $\lambda\lambda$1394, 1403 and several others) with a FWHM of $> 500\,\mathrm{km\ s^{-1}}$ from the broad-line region (BLR). Forbidden lines are not observed, because the density in the BLR is $\sim 10^{10}\,\mathrm{cm^{-3}}$.

- Near Infrared to Mid Infrared (NIR; $\sim$ 1-5 μm, MIR; $\sim$ 5-20 μm) emission at pc-scales from a structure that is optically thick to the optical and sometimes also to the X-rays, and therefore obscures the accretion disk and the BLR from our view. This structure is often called the 'torus'.

- Narrow optical lines with FWHM $\sim 400\,\mathrm{km\ s^{-1}}$, observed in Ly$\alpha$, C IV $\lambda\lambda$1548, 1551, [OIII] λ5007 and other lines from the Narrow line region (NLR). In case the BLR is obscured from our view, the NLR is a good alternative AGN tracer. Usually, the line ratios ([OIII] λ5007)/(Hβ λ4861) and ([NII] λ6583)/(Hα λ6563) are higher than in star-forming regions. A comparison of these line ratios is done with a 'Baldwin-Philips-Terlevich diagram', which is widely used to separate star forming regions from AGN and shocks.

Scale	Observables
< 0.01 pc	UV from the accretion disk + X-rays from the corona
0.1-1 pc	Optical emission from the Broad Line Region
0.1-10 pc	NIR and MIR emission from the torus
100 pc	Optical and MIR emission from the Narrow Line Region
1 -10 kpc	radio jets

Table 1.1: Order of magnitude scales at which certain AGN related phenomena are observed, for a black hole mass of $\sim 10^8 \, M_\odot$. The sizes increase with increasing black hole mass and AGN luminosity.

- Mid Infrared (MIR) spectra show several features in addition to the torus emission, most importantly the presence of highly ionized lines like [OIV] at 25.89 μm.

- AGN may show compact radio emission at the location of the accretion disk, sometimes in combination with kpc-scale radio lobes or jets. The extended radio emission is mostly observed in galaxy clusters or massive elliptical galaxies.

All these processes take place at different spatial scales. Table 1.1 gives an overview of the approximate scales in a galaxy with a SMBH mass of $\sim 10^8 \, M_\odot$.

1.1.3   Role of AGN in galaxy evolution

Although the mass of the central SMBH is small compared to the stellar mass in the bulge ($M_{\rm BH} \approx 10^{-3} M_{\rm Bulge}$; Häring & Rix (2004); McConnell & Ma (2013)), the SMBH may have a significant effect on the entire host galaxy. To see how this is possible, we follow a simple comparison as given by Fabian (2012).

The released energy of an accreted mass M onto a black hole is $\eta M c^2$, with the radiative efficiency $\eta \approx 0.1$. On the other hand, the binding energy of the bulge is $M\sigma^2$, with the velocity dispersion $\sigma < 400 \, {\rm km \, s^{-1}}$. Therefore, if a SMBH has gained all its mass from gas accretion, it has radiated in total $\eta \frac{M_{\rm BH}}{M_{\rm Bulge}} (\frac{c}{\sigma})^2 > 50$ times as much energy as the binding energy of the bulge.

What does this released energy do to the host galaxy? If the energy couples efficiently to the gas in the host galaxy, it could heat gas and drive outflows, which would explain a number of observations: 1) Metal-rich gas is found in the halos of galaxies, which could have been brought there by outflows. 2) The central galaxies in clusters have old stellar populations; somehow the accretion of cold gas or the formation of new stars is slowed down (this is also called 'quenching of star formation'). 3) The black hole mass is tightly related to the velocity dispersion of the stars in the bulge; the $M_{\rm BH}$-σ_* relation. This can be explained if black holes and their host galaxies 'co-evolve'. Clearly, AGN feedback is not the only possible answer to these issues. Galaxy mergers could explain why galaxy mass scales with black hole mass. Active star formation could also drive outflows. And gas streams flowing toward the massive galaxy's center may be shock heated when falling

onto the deep potential well, thereby preventing fuel for star formation from reaching the galaxy. However, including AGN feedback in cosmological simulations solves at once several discrepancies between the models and the observations, and is therefore frequently invoked.

AGN feedback covers roughly two processes: the first is the presence of extended radio jets, and the second is the driving of outflows with radiation from the AGN (Fabian, 2012). The first case is also called 'kinetic mode' or 'radio mode' feedback, and involves hot gas that is sometimes observed in the X-rays. The second case is also called 'radiative mode' or 'quasar mode' feedback. In this short, but powerful, phase, the radiation from the AGN either heats the surrounding Interstellar Medium (ISM) until it pushes the surrounding gas out, or it injects momentum in the ISM when it is absorbed by dust. Both mechanisms are able to drive an outflow.

1.2 The far-infrared/submillimeter view

Each wavelength range reveals a different aspect of the AGN. This thesis concentrates on line observations in the Far Infra Red (FIR) and submillimeter regime, covering a range roughly from 50 μm to 3 mm. This is the range where molecules are observed through their rotational lines, and atoms and ions through fine structure lines. In order to observe the FIR lines, we need telescopes which operate in space, in order to overcome absorption in the earth atmosphere. In the submillimeter, we need interferometers in order to reach the required sensitivity and spatial resolution. The last decade has seen major advances on the performance of these telescopes, making observations possible that could not have been done before.

We used the PACS instrument on the Herschel Space Observatory to observe the fine structure line [CII] and high-J rotational lines of CO, and NOEMA on the Plateau de Bure in Grenoble to observe the rotational line CO(1-0).

The high-J CO rotational lines might trace the warm gas in the optically thick torus, while the line profiles of [CII] and CO(1-0) reveal the presence of outflows. This will be discussed in more detail in Section 1.3 of the Introduction.

1.2.1 CO rotational lines

The most abundant molecule in the molecular Interstellar Medium (ISM) is H_2. H_2 is hard to observe directly, because it has no dipole moment, and therefore no electric dipole transitions: it only has the much weaker electric quadrapole transitions which may be used to trace warm (500-1000 K) H_2. Therefore, rotational lines of the abundant CO molecule ($H_2/CO = 10^4$-10^5) are usually used to trace cool and relatively dense molecular gas.

The energy levels scale as $\propto J(J+1)$, with J the rotational level. The energy of the first level corresponds to 5.5 Kelvin, and has a critical density of $10^3\,\mathrm{cm^{-3}}$. Excitation up to $J = 49$ ($T \approx 7 \times 10^3$ K , $n_{crit} \approx 10^7$-$10^8\,\mathrm{cm^{-1}}$) has been observed in shocks associated
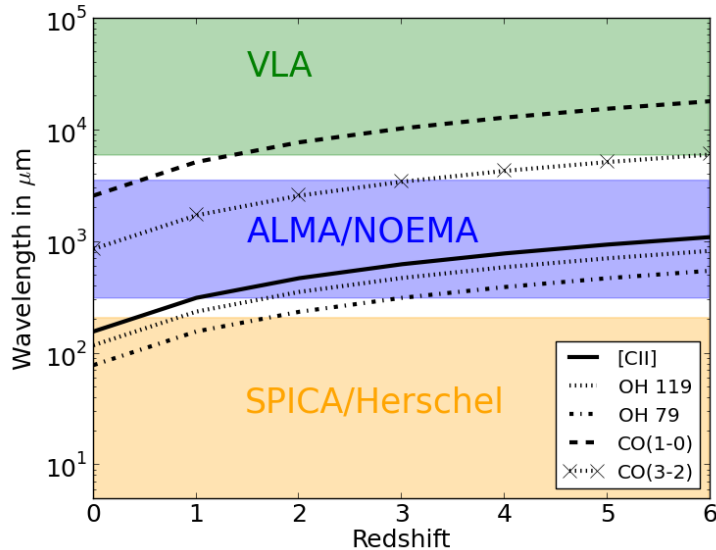
Figure 1.1: Observed wavelength of several tracers of molecular gas, as function of redshift. The background colors show which telescopes can be used: the Very Large Array in the radio, ALMA and NOEMA in the submillimeter, till 2013 Herschel, and in the future perhaps Spica for the FIR regime.

with outflows from protostars (Herczeg et al., 2012). So the rotational lines of CO trace a wide range of ISM conditions.

The Submillimeter telescope NOEMA can observe CO rotational lines up to $J = 3$, and ALMA up to $J = 7$ at $z = 0$. Higher levels lie in the FIR regime, and need to be observed with a space telescope like the Herschel Space Observatory. Figure 1.1 gives an overview of several tracers of molecular gas, their observed wavelength as function of redshift, and which telescopes can be used to observe them.

1.2.2 The fine structure line [CII]

The fine structure line [CII] at 157.74 μm is one of the brightest lines in FIR spectra of galaxies.

It arises from the electron in the valence shell (n=2, l=1, s=1/2) of the singly ionized carbon atom. The vector sum of the orbital angular momentum ($\vec{L}$) and spin ($\vec{S}$) give the total momentum ($\vec{J}$), which can be 1/2 or 3/2. The transition between these 2 levels is the fine structure line [CII], and is written as ${}^2P_{3/2} \to {}^2P_{1/2}$. The excitation temperature is 92 K, and the critical density is $\sim 3.2 \times 10^3 \, \text{cm}^{-3}$ in a neutral medium.

C^+ is a tracer of Photon Dominated Regions (PDRs; also called Photo-dissociation Regions), which are surfaces of molecular clouds illuminated by UV radiation from for example stars. Because carbon has a lower ionization potential than hydrogen (11.26 eV versus 13.6 eV), it remains ionized to larger distances than the hydrogen. C^+ may therefore
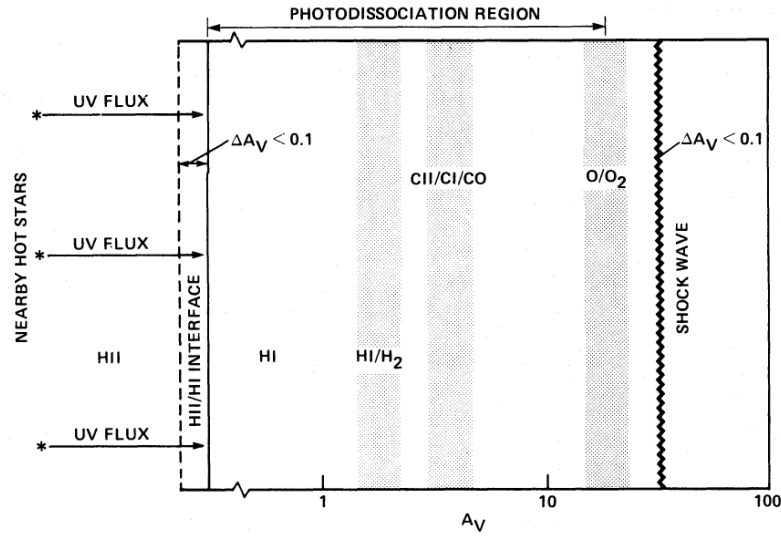
Figure 1.2: A schematic overview of a Photodissociation Region, and which tracers may be found at a certain distance from the cloud edge. On the x-axis is the dust extinction at visual wavelengths, in magnitudes. Figure adopted with permission from Tielens & Hollenbach (1985).

trace both the ionized and the neutral gas. Figure 1.2 shows a schematic overview of the gas in a PDR. One side is illuminated with UV photons, which ionize a small layer of gas. Further in, hydrogen becomes atomic and molecular. Even further, ionized carbon becomes neutral and forms molecules like CO. There are two other mechanisms that heat the ISM; X-rays (from AGN, resulting in an X-ray Dominated Region or XDR) and shocks (from stellar winds or jets). C^+ may trace these regions as well.

1.2.3   Herschel/PACS

The Herschel Space Observatory (Pilbratt et al., 2010) was launched together with Planck on 14 May 2009, and started routine science operations in autumn 2009. The telescope was built to study dust in the ISM and around stars, and cooling of the ISM through rotational lines and fine structure lines. This makes Herschel an ideal telescope for studying star formation and galaxy evolution. A picture is shown in Figure 1.3. It is a 3.5 m diameter passively cooled Cassegrain telescope, and has three instruments on board: PACS, SPIRE and HIFI. Together, these instruments cover wavelengths of 55-672 μm. In April 2013, the mission ended because the telescope ran out of Helium as planned, and could therefore not be cooled anymore.

This thesis makes use of observations made with the Photodetector Array Camera and Spectrometer (PACS; Poglitsch et al. (2010)). PACS could operate as an imaging photometer and as an integral field spectrometer. The photometer simultaneously observed a field of view of 3.5′ by 1.75′ in 2 bands: a red band covering 130-210 μm, and a blue or
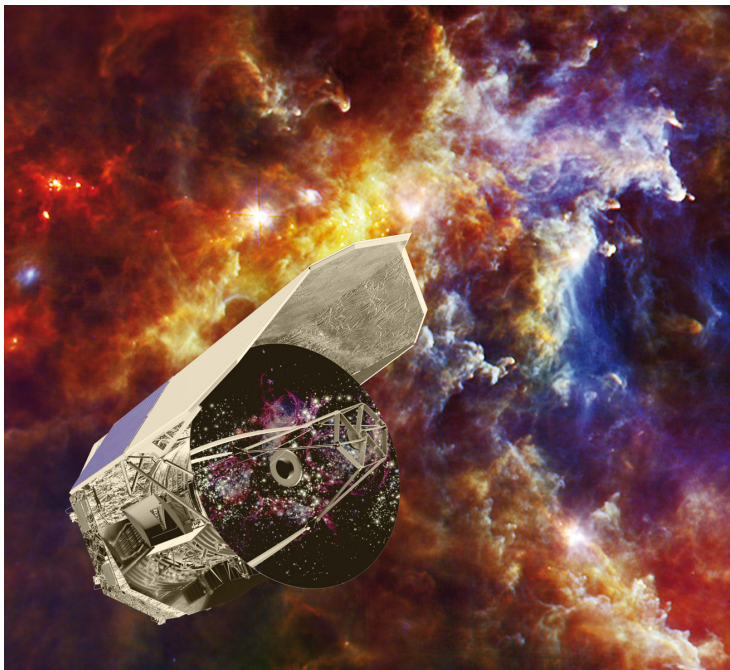
Figure 1.3: An artists impression of the Herschel Space Observatory, with in the background the Rosette molecular cloud as imaged by the PACS and SPIRE instruments. Credit for image: ESA

green band covering 60-85 μm and 85-130 μm respectively. The integral field spectrometer covered a total Field of View of $47'' \times 47''$ with 5×5 pixels, and had a spectral range of 55 to 210 μm.

An earlier successful spectroscopic space mission in the FIR was the Infrared Space Observatory (Kessler et al., 1996). But this mission did not have the sensitivity and spectral resolution to detect broad wings in the line profiles, nor the spatial resolution to isolate a single galaxy in a crowded part of the sky. Currently, the 'Stratospheric Observatory for Infrared Astronomy' (SOFIA) is the only observatory with spectroscopy in the FIR (Young et al., 2012), while Spica – the next space mission that will match the resolution and exceed the sensitivity of Herschel – is still under consideration.

1.2.4 NOEMA

Radio telescopes tend to have large dishes: with a large dish one can observe fainter objects and resolve smaller structures, and both are needed in the radio regime. The resolution of a telescope is taken to be the radius of the Airy disk, which is $1.22\frac{\lambda}{D}$ with λ the wavelength and D the diameter of the dish, in the ideal case of two point sources, emitting incoherent radiation. Where a 0.2 meter optical telescope resolves Hα ($\lambda = 656.3$ nm) at $0.8''$, a telescope with a diameter of almost 800 meter is needed to achieve the same resolution at 2.6 mm; the wavelength of the CO(1-0) transition. Apart from the practical issues

with a kilometer-sized dish, radio telescopes suffer from standing waves, caused by radio waves scattering off the telescope structure onto the receiver (Briggs et al., 1997). Both issues are solved in an interferometer, in which several antennas are placed apart to work simultaneously. The signals from all antennas are combined to reach a resolution inversely proportional to the distance between the antennas, rather than the diameter of a single dish.

The difficulty is to combine the light from the different antennas in phase, and receive enough flux on each antenna to allow splitting of the signal prior to combination with signals from other antennas. This would be facilitated if the signals could be digitally sampled and stored, but the frequency is too high for that in the millimeter regime (~ 100 GHz). Therefore, the signal received by each antenna is transferred to a lower frequency, by mixing it with a 'Local Oscillator' signal which is tuned to lie close to the frequency of interest. Combining the two wave signals results in new signals both at a frequency $\omega_{obs} + \omega_{LO}$ and at $\omega_{obs} - \omega_{LO}$. In the last case, this brings the observed frequency down to one that can be amplified, transported, sampled and saved digitally (the whole process is called heterodyne detection). For example, $\omega_{obs} = 115$ GHz and $\omega_{LO} = 111$ GHz, so the line will be observed at 4 GHz. This signal is amplified before it is correlated with signals from the other telescopes. Then the correlated signal is recorded and calibrated.

Correlated signals are recorded from every pair of antennas. In case the two incoming waves interfere coherently, the recovered power is at its maximum, while the recovered power is zero for incoherent interference. These 'recovered powers' or 'visibilities' are a function of distance between the antennas, usually expressed in the parameters u and v (in meters). One may analyse the uv visibilities directly, and derive whether the source is point-like, Gaussian-like or disk-like, and to estimate its extent. With sufficient uv data, one may also reconstruct an image of the source. This is done by Fourier transforming the visibilities, as described by the van Cittert-Zernike theorem.

This thesis makes use of observations done at the submillimeter interferometer NOEMA (formerly known as the Plateau de Bure Interferometer PdBI). NOEMA is located in the Alps near Grenoble, and consists currently of seven antennas with 15 meter diameter dishes. Figure 1.4 shows six of these antennas. With a maximum distance of 760 meter along the East-West track, the telescope can reach a spatial resolution of 0.7″ for the CO(1-0) line. In 2012 it started an upgrade which will double the number of antennas from 6 to 12, extend the longest baseline from 0.8 km to 1.6 km, and increase the bandwidth from 8 GHz to 32 GHz. A previous upgrade to the 'WideX' correlator – with an increased bandwidth from ~ 1 GHz to ~ 4 GHz – made the study of fast outflows possible. In order to cover a large enough wavelength range to separate the outflow emission (sometimes exceeding 1000 km s^{-1}) and continuum emission, a bandwidth of a few GHz is required at the rest frequency of the CO(1-0) transition. One of the first uses of this new technique is presented in Feruglio et al. (2010).

Submillimeter telescopes like NOEMA, ALMA, SMA and others, are used to study the cold (or distant) universe, including protostellar systems and protoplanetary systems, distant galaxies, and complex molecules.

Figure 1.4: The NOEMA interferometer in compact configuration, before the upgrade which will increase the number of antennas from 6 to 12. Image adopted from IRAM website.

1.3   This thesis

This thesis treats two aspects of AGN; the excitation of high rotational levels of CO in the torus, and the driving of molecular outflows.

1.3.1   Can the torus be detected in high-J CO lines?

Antonucci & Miller (1985) postulated the presence of an obscuring structure around the accretion disk and BLR of the AGN NGC 1068, in order to explain the observed polarized X-ray emission. If this obscuring structure is a part of all AGN, and has the shape of a torus, it would explain why about half of the AGN are detected in X-rays and show broad lines (type-1 AGN), while others are not (type-2 AGN). This obscuring structure is often called 'the torus', even if its precise shape and physical size are unknown. The optical emission from the Broad Line Region is absorbed by dust with cross sections of 10^{-21}-10^{-22} cm^2/H-atom (Draine, 2003). X-rays on the other hand, are absorbed by oxygen and iron in the gas. Cross section for X-ray absorption are $\sigma = 10^{-20}$-10^{-24} cm^2/H-atom for photon energies ranging from 0.1 keV to 10 keV (Ryter, 1996). Most type-2 AGN can therefore be detected in hard X-rays, unless the torus has a column density $> 10^{24}$ cm^{-3}, in which case the AGN is called Compton-thick (as is the case in the prototypical Seyfert 2 galaxy NGC 1068).

   The warm dust acts like a blackbody, with its spectrum peaking in the Mid Infrared. High spatial resolution observations ($< 0.1''$) are needed in order to resolve the torus in a nearby AGN like NGC 1068. This has been done for example with the MIDI instrument

at the Very Large Telescope Interferometer (VLTI), using 2 telescopes and observing from 8-13 μm. Using MIDI, López-Gonzaga et al. (2014) find several components at 1-10 pc scale, at the position of the AGN in NGC 1068.

Alternatively one may target the gas instead of the dust. In chapter 2 we investigate a way to detect the X-ray absorbing gas through high-J CO lines. Krolik & Lepp (1989) suggested that lines around CO(40-39) and higher may be used for this purpose. If several lines are detected, they could even be used to derive the temperature and density in the X-ray obscuring gas. However, the region from which this emission is expected to arise is small, and sensitive observations are necessary. A deep integration around the CO(40-39) line in NGC 1068 was therefore taken with PACS. The line was not detected, and we investigate how this upper limit constrains the conditions in / the geometry of the gas in the torus, using an XDR model. We conclude the following: In order to produce observable amounts of CO(40-39), both strong X-rays and a large column density of $\sim 10^{25}\,\mathrm{cm}^{-2}$ are required. However, if the gas contains any dust, this will absorb most of the CO(40-39) emission, because dust has a cross section of $\sigma = 1.3 \times 10^{24}\,\mathrm{cm}^2$ H-atom at the wavelength of the CO(40-39) transition (under conditions similar to those in the Milky Way; Draine (2003)).

Therefore, the high-J CO lines are not ideal tracers of the molecular AGN torus. They are probably better tracers of shocks, as mentioned earlier. However, in the mean time the molecular torus in NGC 1068 has been detected in another way. García-Burillo et al. (2016) present ALMA observations of NGC 1068 in CO(6-5), which reveal a ~ 10 pc diameter disk, in accordance with the size derived from dust emission. Gallimore et al. (2016) use the same transition to find ~ 300 km s^{-1} emission aligned perpendicular to the major axis of the torus, as given by the H$_2$O maser disk. They interpret this as a biconical outflow from the torus.

1.3.2 Broad wings in [CII] as a tracer of molecular outflows

It is only recently that galaxy-scale outflows gained much attention, which can be explained by two developments: the recent need for these outflows to explain the observations as discussed in Section 1.1.3, and the frequency with which these outflows are detected. Sensitive observations are needed in order to detect outflows in line emission, because the outflow is typically a hundred times fainter than the host galaxy. Moreover, the observed velocity range must be large enough to allow separation of the high-velocity emission of the outflow and the continuum emission. Since the moment that these sensitive observations are performed frequently, outflows are found to be common in AGN hosts and star forming galaxies, and appear in ionized, atomic and molecular phases.

Chapter 3 discusses 22 local Ultra Luminous InfraRed Galaxies (ULIRGs). Most of the galaxies in this sample are known to have molecular outflows, as traced by blueshifted absorption in the rotational OH line at 119 μm (observed with Herschel/PACS). In some objects, redshifted emission is visible as well, resulting in a so-called 'P-Cygni profile'. An example is given in Figure 1.5. This combination of blueshifted absorption and redshifted emission is a clear sign of an outflow. Although OH is a good tracer of these molecular
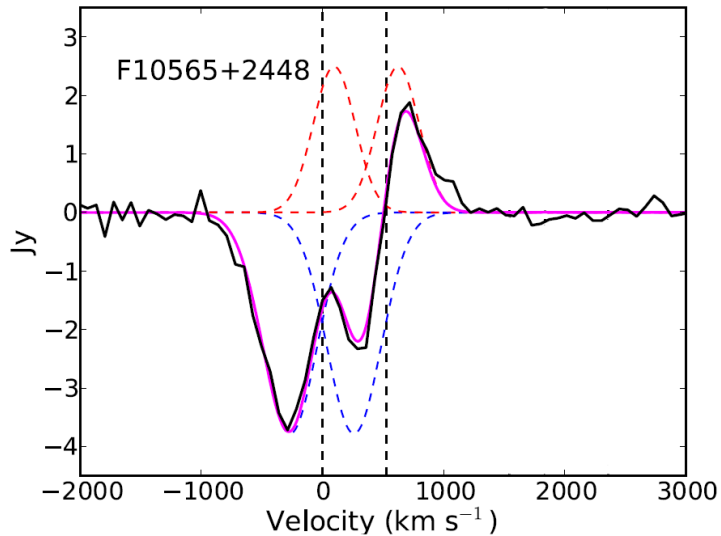
Figure 1.5: The P-Cygni line profile of the OH119 doublet in the ULIRG IRAS 10565+2448. The dotted vertical lines show the rest wavelengths of the doublet. The line profile has been fitted with a combination of a redshifted- and a blueshifted-component. This line profile is expected from spherically symmetric outflows, with the blueshifted absorption arising from gas moving toward us, and redshifted emission from gas moving away from us. Figure adopted with permission from Veilleux et al. (2013).

outflows, it can only be used in objects with a bright FIR background because it is observed in absorption. We therefore consider [CII] as an alternative tracer, which reveals outflows through broad line wings in emission. An additional advantage of [CII] might be that it moves into the ALMA bands at $z \approx 1$, whereas OH119 only does so at $z \approx 2$ (Figure 1.1).

In order to test whether [CII] is a suitable tracer of molecular outflows, we compare the outflow velocity and mass, as derived from the broad wings in the [CII] line profile, to those derived from OH119. There is a linear relation between the velocities, as is expected when [CII] traces the same outflow as OH119. Moreover, the outflow masses traced by [CII] and OH119 follow a 1:1 relation, although with significant scatter and large uncertainties. We conclude that [CII] is a reliable tracer of (molecular) outflows.

Are these outflows AGN-driven? Local ULIRGs are mergers of gas-rich galaxies, exhibiting enhanced star formation and AGN activity. The AGN may be weak or buried in large amounts of gas. Genzel et al. (1998) conclude that star formation dominates the bolometric luminosity of a sample of ULIRGs (which partly overlaps with the sample used here), based on the line ratio [OIV]/[NeII] and the strength of the $7.7\,\mu$m PAH feature. There are however several reasons to believe that AGN play a significant role in powering the outflows in our sample. First of all, the outflow velocities exceed $1000\,$km s^{-1} in some cases, which is very fast for a star-formation driven outflow. Furthermore, the outflow velocities and rates correlate with the AGN luminosity: this is found for OH by Sturm et al. (2011b); Veilleux et al. (2013), and for CO(1-0) by Cicone et al. (2014) (the samples

are partially different but all involve ULIRGs).

1.3.3 Spatially resolving the molecular outflow in IRAS F08572+3915

A good understanding of the outflow extent and geometry requires spatially resolved observations. This is not possible with PACS, because the beam size is $\sim 12''$ at $158\,\mu$m (the rest wavelength of [CII]) and $\sim 9.5''$ at $119\,\mu$m (the rest wavelength of OH119), corresponding to scales of 4 kpc to 22 kpc for the objects in the ULIRG sample discussed in Chapter 3. The outflows appear unresolved at this scale.

Instead, submillimeter observations of the broad wings in CO(1-0) may be used to trace the molecular outflow, as interferometers like NOEMA can achieve subarcsecond resolution.

Ideally, we would like to compare the outflow velocity and mass as derived from CO(1-0) to those derived from OH119 or [CII], as described in Chapter 3, in order to verify that all lines trace more or less the same outflow. But retrieving the spectra for all 22 objects is time consuming, and may take another few years. It has been done for a few objects however (Cicone et al., 2014), of which IRAS F08572+3915 stands out as hosting a particularly massive and fast outflow.

In Chapter 4 we present deep, subarcsecond resolution, observations of the CO(1-0) line in IRAS F08572+3915. The receding and the approaching part of the outflow are spatially resolved, and are offset from the galaxy's center in opposite directions, consistent with a biconical outflow. The approaching part of the biconical outflow overlaps spatially with the outflows detected in warm H_2, $H\alpha$ and Na I D. Moreover, the receding outflow is spatially resolved into two components: the second component is an isolated blob at $\sim 5''$ from the galaxy's center, and displays a velocity gradient. If moving at a constant speed of 900 km s^{-1}, and projection effects in speed and distance to the galaxy's center cancel out, this outflowing component could be a ~ 0.7 Myr lasting outflow event starting ~ 6 Myr ago, possibly caused by a previous AGN burst.

1.3.4 Summary of conclusions

The high sensitivity and spectral resolution achieved by PACS at the Herschel Space Observatory allowed us to search for faint high-J CO lines and high-velocity wings in the [CII] line profile. We also used the submillimeter interferometer NOEMA to spatially resolve the molecular outflow in a nearby ULIRG. In summary, the conclusions are:

- The CO(40-39) line is not an ideal tracer of the molecular torus, mostly because in an X-ray Dominated Region the column density required to produce observable amounts of emission is $\sim 10^{25}\,$cm^{-2}.

- Broad wings in the [CII] line profile may be used as tracer of molecular outflows: the outflow velocity and gas mass derived from these wings scales linearly with those found from OH119.

- The massive molecular outflow in the nearby ULIRG IRAS F08572+3915 is bursty, rather than continuous. It has a bicone-shaped geometry (as opposed to a full shell or individual clouds), and is aligned with the galaxy's disk (rather than perpendicular to the disk).

Chapter 2

A deep Herschel/PACS observation of CO(40-39) in NGC 1068: a search for the molecular torus

2.1 Introduction

Low-J rotational lines (up to J $\approx$ 7) of CO have long been used as a tracer for molecular gas. With the Herschel Space Telescope[1] (Pilbratt et al., 2010) it was possible to observe CO lines of higher J levels, extending the CO spectral line energy distribution (SLED) to J = 50 (for J $\rightarrow$ J $-$ 1). The PACS instrument (Poglitsch et al., 2010) on board Herschel samples the highest frequencies, with 13 < J < 50, which we will call the high-J CO lines. These lines with wavelengths 186.0 μm < λ < 52.85 μm arise from states $\sim$ 500-7,000 K above ground, with critical densities of $\sim$ 10^6-10^8 cm^{-3}, and are thus good tracers of the photon dominated regions (PDR) in the warm and dense interstellar matter (ISM) around stars, in shocks, or in the X-ray dominated regions (XDRs) of AGN.

AGN unification models require a structure that obscures the UV and optical emission from the broad line region of Type-2 AGN from our view (Antonucci & Miller, 1985). Further, Compton-thick AGN, like NGC 1068 (Elvis & Lawrence, 1988), require an X-ray absorbing medium with a column density of at least $N_H = 10^{24}$ cm^{-2}, potentially in the form of molecular gas. These two effects are often assumed to be caused by a dusty torus, although the gas and the dust are not necessarily distributed in the same way. In this

---

[1]Herschel is an ESA space observatory with science instruments provided by European-led principal investigator consortia and with important participation from NASA.

paper, we investigate whether high-J CO lines can trace the X-ray absorbing gas (from now on called 'the torus'), be it in the form of a classical torus (Krolik & Begelman, 1988; Krolik & Lepp, 1989) or of a more clumpy and more extended cloud structure. The CO emission from a parsec-scale torus was first modeled by Krolik & Lepp (1989) (hereafter KL89), who found that the line fluxes should scale as J^3 up to J$\approx$ 58 (in this particular model for NGC 1068), and with absolute fluxes proportional to the total absorbed hard X-ray luminosity. More recent torus models have envisioned a dynamical structure of small clouds distributed over several parsecs surrounding the AGN (Nenkova et al., 2002; Hönig et al., 2006). However, these newer clumpy torus models do not yet incorporate a gas phase and have been used so far only to predict the dust emission from an AGN.

In Hailey-Dunsheath et al. (2012) (hereafter HD12) we carried out a detailed analysis of the full CO SLED of NGC 1068 up to J = 30 (for higher J only upper limits were found). We concluded that two components are responsible for the CO SLED between $10 < J < 31$: the $\sim$200 pc diameter ring and the northern streamer, both traced by H$_2$ 1-0 S(1) observations (Müller Sánchez et al., 2009). Would the molecular torus, if it exists, be observable in the $J > 30$ lines? In order to answer this question, we carried out an additional, deeper, observation of CO(40-39).

The paper is organized as follows: a description of the existing multiwavelength observations of NGC 1068 is given in section 2.2. Section 2.3 covers the PACS observations and data reduction and presents the full (55-200 μm) spectrum of the central spatial pixel (spaxel). Section 2.4 describes updates on the PDR, XDR, and shock fits presented in HD12, including the new upper limit on CO(40-39) and a small correction to the CO SLED. A brief description of the XDR code used to model the torus emission is given in section 2.5. A discussion of the results follows in section 2.6.

2.2   NGC 1068

NGC 1068 is a Seyfert 2 galaxy at a distance of 14.4 Mpc, implying a 72 pc arc sec^{-1} scale (Bland-Hawthorn et al., 1997). Because of its proximity and luminosity, NGC 1068 is a favorable object for testing hypotheses on Seyfert galaxies.

Early X-ray observations showed emission from the AGN nucleus, but only in scattered light (Elvis & Lawrence, 1988) because the AGN is completely obscured from our view by a column of $N_H = 10^{25}\,\mathrm{cm}^{-2}$ (Bauer et al., 2014). The intrinsic 1-100 keV luminosity, estimated from the observed scattered X-rays, lies between $10^{43}\,\mathrm{erg\,s}^{-1}$ and $10^{44}\,\mathrm{erg\,s}^{-1}$. The largest uncertainty in the X-ray luminosity is the fraction of X-rays that is scattered into our line of sight. Pier et al. (1994) give a comparison of different methods to determine this fraction, from which we derive an intrinsic luminosity $L_{1-100\,\mathrm{keV}} = 10^{43.5}\,\mathrm{erg\,s}^{-1}$, and a spectral slope $F_\nu \sim \nu^{-1}$ (or photon index $\Gamma = 2$).

Further out from the obscuring torus, the AGN is surrounded by a ring of molecular gas with a radius of $\sim 1''$-$5''$ (72-360 pc), also called the circumnuclear disk (CND). The CND is observed in CO and H$_2$ (Schinnerer et al., 2000; Müller Sánchez et al., 2009), and observations of SiO, HCN and CN suggest an X-ray driven chemistry (Lepp & Dalgarno,

1996; Usero et al., 2004; García-Burillo et al., 2010).

Inside this shell, the near-infrared integral field spectrograph SINFONI provided 0.075″ resolution observations of H_2 1-0 S(1), which reveal two streamers within 0.4″ (30 pc; Müller Sánchez et al. (2009)). The southern streamer lies between us and the AGN's center. The SINFONI observations furthermore reveal the presence of the northern streamer (0.4″ or 30 pc north of the AGN's center), which may fuel the central black hole.

A ring of H_2O masers, with a radius of ~ 20 mas (1.5 pc), is centered at the AGN (Gallimore et al., 1996). The water masers trace densities $n_H > 10^7\,\mathrm{cm}^{-3}$, and could well locate the inner edge of a molecular torus. The dust in the torus, on the other hand, is best observed in the IR continuum. The NGC 1068 nucleus has been observed several times with the mid-infrared interferometer (MIDI) in order to determine the dust distribution. López-Gonzaga et al. (2014) presented the most recent observations, which resolve the central 1-10 pc of the AGN. The observations are best fit with three gray bodies with a Gaussian intensity distribution: a $\sim 1.4\,\mathrm{pc} \times 0.5\,\mathrm{pc}$ component of 700 K, a $\sim 3\,\mathrm{pc} \times 2\,\mathrm{pc}$ component of ~ 300 K, and a component offset to the west (by 1.7 pc) and north (by 5.6 pc) with a projected size of $\sim 14\,\mathrm{pc} \times 3.5\,\mathrm{pc}$ and a temperature of ~ 360 K.

2.3   PACS Observations and Data Reduction

The CO ladder of the NGC 1068 nucleus has been observed up to J = 30 with the Photo detector Array Camera and Spectrometer (PACS) on board the Herschel Space Observatory, and is described in HD12. Here we present a deeper observation taken around $\lambda = 65.94\,\mu\mathrm{m}$, where we expect the CO(40-39) line with a rest wavelength $\lambda = 65.69\,\mu\mathrm{m}$ to be at a system velocity of $v_{\mathrm{LSR}} = 1125\,\mathrm{km\,s^{-1}}$. The observations were taken as part of our GT Key Project SHINING; the OBSIDs are listed in Table 2.1. Among the high-J CO lines, CO(40-39) is particularly suitable because the spectra of bright galaxies have little contamination from other lines around $\lambda = 65.69\,\mu\mathrm{m}$. Moreover, the line traces gas with densities $> 10^6\,\mathrm{cm}^{-3}$ and temperatures > 500 K (Table 2.2), and distinguishes a highly excited (HE) component from the gas in the CND and streamers.

We used HIPE 11 for the data reduction. The previous data were analyzed with HIPE 6 (HD12), so we re-reduced some of the J $\leq$ 30 lines with HIPE 11. The high-J lines detected in NGC 1068 are all consistent with the scenario that they arose in the central spatial pixel that covers the central $\sim (9''.4)^2$ or $(700\,\mathrm{pc})^2$ of NGC 1068. Therefore, the data reduction discussed here applies to the central spaxel only. The spectra were reduced with the standard pipeline for a "chopped line scan and short range scan with background normalization", including the point source correction factor (Poglitsch et al., 2010), and setting the up-sample parameter to 1 and the over-sample parameter to 2. We found that the CO(30-29) flux should be slightly modified, so we now measure $(2 \pm 1) \times 10^{-17}\,\mathrm{W\,m^{-2}}$, instead of $(4.2 \pm 1.9) \times 10^{-17}\,\mathrm{W\,m^{-2}}$. There is one other small modification we make to the error bars published in HD12: the error in CO(22-21) is larger than 30% of the total flux. This line is observed at the edges of two adjacent spectral scans, and therefore the uncertainty in the flux is larger than in other lines. The modified line flux is $(4^{+4}_{-1.4}) \times$

OBSID	Blue Band	Red Band
	μm	μm
1342203129	65.0-70.5	130.2-141.2
1342203128	58.5-66.0	117.4-132.0
1342203127	52.0-59.5	103.8-119.4
1342203126	94.6-98.0	188.6-196.0
1342203125	91.0-95.1	181.4-190.4
1342203124	87.3-91.5	174.0-183.0
1342203123	83.2-87.7	166.0-176.0
1342203122	78.9-83.7	157.0-167.7
1342203121	74.4-79.4	148.0-159.0
1342203120	70.0-75.0	139.6-150.0
1342259623	65.4-66.5	...
1342259624	65.4-66.5	...

Table 2.1: OBSIDs and covered wavelength of the full Herschel/PACS scan of NGC 1068. All observations for the full spectrum have been performed on observational day (OD) 460. The last two OBSIDs are from the deeper observations on CO(40-39).

Transition	Rest Wavelength	Upper Limit	n_{crit}	E_{upper}/K_B
	(μm)	(10^{-17} W m^{-2})	(cm^{-3})	(K)
CO(40-39)	65.69	2	10^7	4×10^3

Table 2.2: Details of the CO(40-39) line.

$10^{-17}\,\mathrm{W\,m^{-2}}$.

The CO(40-39) line observations have been reduced with the same pipeline and parameter setting as described above. Figure 2.1 shows the region of the CO(40-39) line in the rest frame with a spectral resolution of $0.04\,\mu$m. There is no clear emission at $\lambda = 65.69\,\mu$m, but there could be an absorption feature around $\lambda = 65.6\,\mu$m. Potential absorbers are ^{18}OH $\Pi_{3/2} - \Pi_{3/2}\frac{9^+}{2} - \frac{7^-}{2}$ at $65.69\,\mu$m, the CO(40-39) line itself, H_2O^+ $3_{31} - 2_{20}\,7/2 - 5/2$ at $65.61\,\mu$m, and NH_2 at $65.57\,\mu$m. From our PACS observations of other galaxies at both $65\,\mu$m and $120\,\mu$m the line flux ratio of ^{16}OH to ^{18}OH is always found to be equal to or greater than 10 (González-Alfonso et al., 2012, 2014). Because there is no ^{16}OH absorption visible in Figure 2.1 at $65.28\,\mu$m, ^{18}OH cannot be responsible for the absorption feature at $\lambda = 65.6\,\mu$m. Moreover, if identified with ^{18}OH or CO(40-39), the line would be blue-shifted by $400\,\mathrm{km\,s^{-1}}$ with respect to the host galaxy, while the highest velocity features in the AGN nucleus are the water masers, with $\sim 300\,\mathrm{km\,s^{-1}}$ (Gallimore et al., 1996).

Absorption by NH_2 is unlikely because it should have several features of comparable intensity as indicated in Figure 2.1, and these are not observed. Moreover, the other NH_2 lines in NGC 1068 are faint. See Figure 2.2 for the full (55-200 μm) PACS spectrum from the central spaxel of NGC 1068. H_2O^+ absorption cannot be excluded completely, with the $65.61\,\mu$m line the strongest of the three lines in Figure 2.1, but it would be an exception
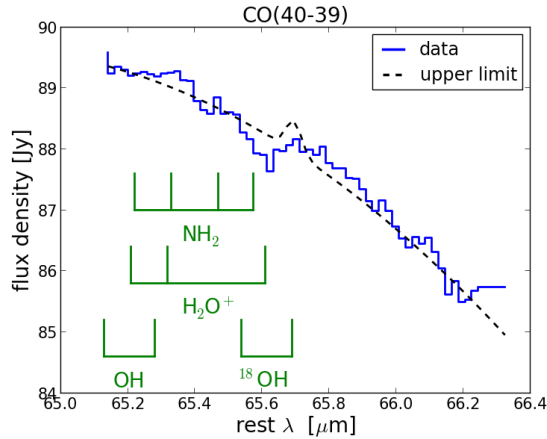
Figure 2.1: Continuum fit and 3σ upper limit: A Gauss profile with a flux of 2×10^{-17} W m^{-2} and a FWHM of 250 km/s illustrates the 3σ upper limit of the CO(40-39) line, at the system velocity of NGC 1068 and a rest wavelength of $65.69\,\mu$m. The feature around 65.6 μm is considered an artifact.

in an otherwise emission dominated spectrum. A detailed analysis of the PACS spectra of NGC 1068 and other objects will be given in Fischer et al. (in preparation).

Therefore, we assume that the feature around $\lambda = 65.6\,\mu$m is an artifact, and treat it as noise. This results in a noise level of 0.12 Jy, and a 3σ upper limit on CO(40-39) of 2×10^{-17} W m^{-2}, for a line width of $250\,$km s^{-1} (HD12). Figure 2.1 shows the upper limit superposed on the spectrum. If the feature is masked out during the fit, the 3σ upper limit becomes 1×10^{-17} W m^{-2}, and the absorbed flux is 4×10^{-17} W m^{-2}. The feature could have absorbed the blue part of the CO(40-39) line, but it is hard to quantify by how much. Because there is no red wing visible, the artifact would have to be coincidentally just equal to that of a possible CO(40-39) emission line in order to mask it. We find this scenario unlikely and use the aforementioned upper limit of 2×10^{-17} W m^{-2} for our analysis. The CO SLED with the upper limit and the modifications to HD12 is given in Figure 2.3.

2.4   PDR, XDR, and shock models

With the slightly modified CO(30-29) value and the new CO(40-39) upper limit we repeated our PDR, XDR, and shock fits with the same models as in HD12. For comparison we briefly summarize the main results from HD12 here. The observed CO SLED was analyzed with large velocity gradient- (LVG), shock, PDR, and XDR models. Only the PACS data were fitted; the $3 < J < 14$ CO lines that trace the colder gas were analyzed by Spinoglio et al. (2012). The PACS SLED is best explained with two components: a moderately excited (ME) component with $T_{kin} \approx 169\,$K, $n_{H_2} \approx 10^{5.6}\,$cm^{-3} and a total mass of $M_{H_2} \approx 10^{6.7}\,M_\odot$, and a highly excited component with $T_{kin} \approx 571\,$K, $n_{H_2} \approx 10^{6.4}\,$cm^{-3} and a total mass of $M_{H_2} \approx 10^{5.7}\,M_\odot$. The ME component can arise from X-ray- or shock-heated gas in the
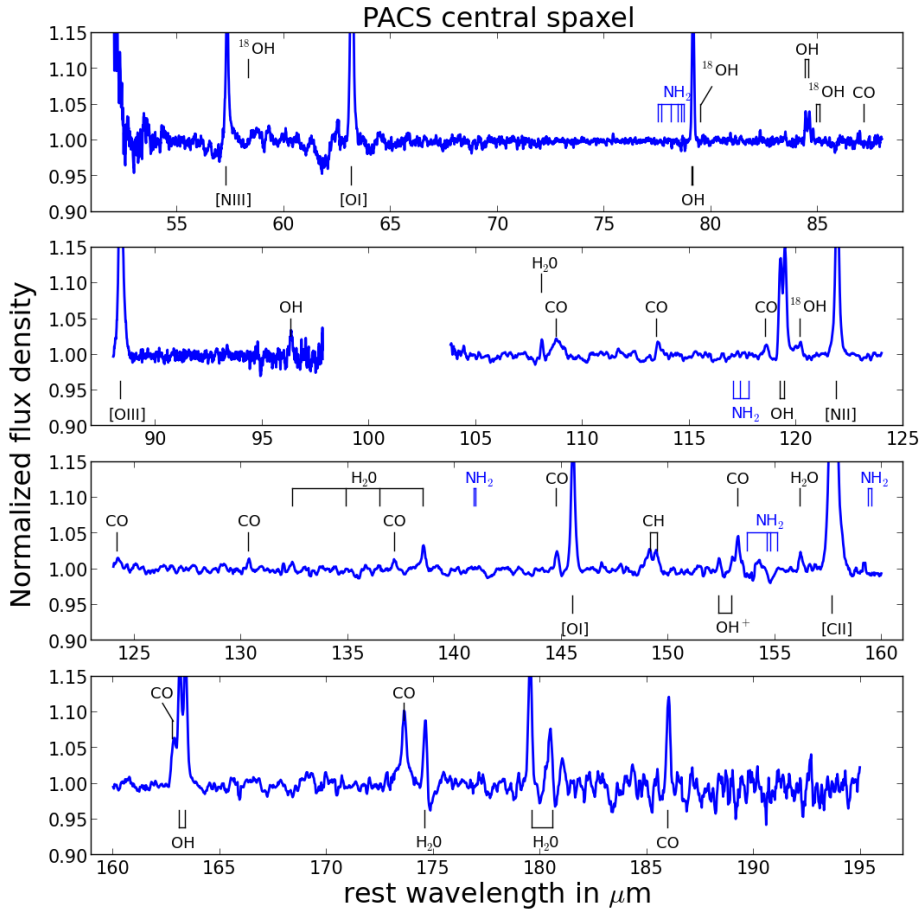
Figure 2.2: Full PACS spectrum of the central spaxel. The wavelengths of the brightest NH_2 lines are indicated in the spectrum to show that they are very faint (if detected at all). At 119 μm, the flux ratio is $^{16}OH/^{18}OH \approx 10$, so if no ^{16}OH is observed at 65.28 μm, the ^{18}OH line cannot cause the absorption at 65.6 μm. 61 μm to 63 μm is a known region with artifacts in the relative spectral response function.

CND, while the HE component can arise from either the CND or the northern streamer. In order to determine whether the HE component arises from the CND or the northern streamer, we followed H12 and compared the PACS CO line shifts with the SINFONI observations of H_2 1-0 S(1). The PACS HE lines are blueshifted by $59 \pm 20 \, \mathrm{km \, s^{-1}}$, which best matches the $\sim 25 \, \mathrm{km \, s^{-1}}$ blueshift of the northern streamer.

To fit our new results, we use the XDR grid from Meijerink et al. (2007). This grid contains the CO line emission for gas with densities of $n_H = 10^4$-$10^{6.5} \, \mathrm{cm^{-3}}$ and X-ray fluxes $F_X = 1.6$-$160 \, \mathrm{erg \, cm^{-2} \, s^{-1}}$. In HD12, the HE component was best fit with $F_X = 160 \, \mathrm{erg \, cm^{-2} \, s^{-1}}$, i.e. the maximum value in the grid. This time we used an extended grid with $F_X = 9$-$510 \, \mathrm{erg \, cm^{-2} \, s^{-1}}$ (R. Meijerink, private communication).

Table 2.3 and Figure 2.3 show the parameters of the best XDR, PDR, and shock fits. Only detected lines were used during the fit, but the best fits were in all cases consistent with the upper limits of the high-J CO lines. The XDR fit of the HE component is slightly different from HD12, primarily due to the lower value for CO(30-29) and to the extension of the grid: the best fit now has an input X-ray flux $F_X = 510 \, \mathrm{erg \, cm^{-2} \, s^{-1}}$, which is again the high endpoint of the grid. We tested whether an even higher X-ray input flux would better fit the HE component, using a different XDR grid (described in Section 2.5.1), that contains X-ray fluxes up to $F_X = 10^6 \, \mathrm{erg \, cm^{-2} \, s^{-1}}$. For a thermal X-ray input spectrum like that in the grid from Meijerink, the CO SLEDs from the two codes agree within 20% for J < 30. In this model an input flux of $F_X = 10^3 \, \mathrm{erg \, cm^{-2} \, s^{-1}}$ could still fit the HE component, but is no improvement over the fit with $F_X = 510 \, \mathrm{erg \, cm^{-2} \, s^{-1}}$.

Our shock modeling uses a two-component fit: the ME C-shock model is from Flower & Pineau Des Forêts (2010), and the HE C-shock model is from Kaufman & Neufeld (1996). The lower value of the CO(30-29) line has a small effect on the best fit of a shock model to the HE component. The HE component can now be fit with a 30 km s^{-1} velocity, instead of 40 km s^{-1}. The effect on the PDR modeling is small (using the PDR model from Meijerink et al. (2007)). A PDR cannot be ruled out, but it is hard to match the J = 30 line without overproducing the lower J lines. A single PDR component only marginally fits the entire SLED (see Figure 2.3). Because the kinematics of the lines suggest two components, we discard this option. The PDR fit to the HE component ($J \geq 19$) alone is slightly improved with the lower CO(30-29) flux, but is not as good as an XDR or shock fit.

The upper panel in Figure 2.3 also shows the expected CO emission from a parsec-scale molecular torus with $N_H = 10^{24} \, \mathrm{cm^{-2}}$ and $f_{cov} f_{x44} = 0.08$, as predicted by KL89, where $f_{cov} = 0.25$ is the surface covering factor of the torus and $F_X = F_{x44} \times 10^{44} \, \mathrm{erg \, cm^{-2} \, s^{-1}}$. This is further discussed in section 2.5.2.

We conclude that the revised value for CO(30-29) and the new upper limit on CO(40-39) do not significantly change the results from HD12. They found that the ME component can arise from X-ray or shock-heated gas in the CND, while X-ray heated gas in the northern streamer is the preferred explanation for the HE component, based on the fits and the kinematics.
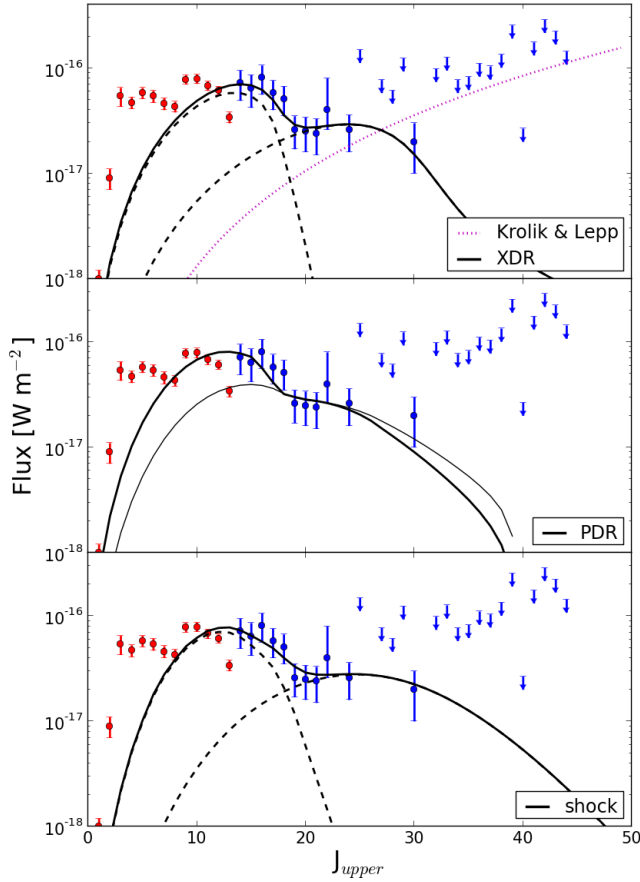
Figure 2.3: Best XDR, PDR, and shock fits to the CO SLED. Red points indicate Plateau de Bure Interferometer data (J from 1 to 3, with beam size ranging from $0.6''$ to $2.5''$; Krips et al. (2011)) and Spire data (J from 4 to 13, with beam sizes ranging from $17''$ to $42''$; Spinoglio et al. (2012)), blue points represent PACS data (J > 13, with beam size ranging from $11''$ to $14''$; HD12). Only the PACS observations were used for the fits. Upper panel: A two-component XDR fit with an extended grid of Meijerink et al. (2007), and expected CO emission from an X-ray heated molecular torus with $N_H = 10^{24}\,\mathrm{cm}^{-2}$ and $f_{cov}f_{x44} = 0.08$ (KL89). Central panel: PDR fit to the full PACS SLED (thick line), and a PDR fit to the $J \geq 19$ observations (thin line). Lower panel: a two-component shock fit. The model parameters of all fits are discussed in the text and in Table 2.3.

	ME	HE	Full	χ^2
XDR	$n_H = 10^{5.25}\,\mathrm{cm}^{-3}$	$n_H = 10^{6.5}\,\mathrm{cm}^{-3}$	...	
	$F_X = 9\,\mathrm{erg\,cm}^{-2}\,\mathrm{s}^{-1}$	$F_X = 510\,\mathrm{erg\,cm}^{-2}\,\mathrm{s}^{-1}$	...	1.23
	$A \approx (108\,\mathrm{pc})^2$	$A \approx (20\,\mathrm{pc})^2$	...	
PDR	...	$n_H = 10^{6.5}\,\mathrm{cm}^{-3}$	$n_H = 10^{6}\,\mathrm{cm}^{-3}$	
	...	$G_0 = 10^5$	$G_0 = 10^5$	2.16
	...	$L_{FUV} \approx 3 \times 10^9 L_\odot$	$L_{FUV} \approx 10^{10} L_\odot$	
C-shock	$n_0 = 2 \times 10^5\,\mathrm{cm}^{-3}$	$n_0 = 10^6\,\mathrm{cm}^{-3}$	...	
	$v = 20\,\mathrm{km\,s}^{-1}$	$v = 30\,\mathrm{km\,s}^{-1}$	...	1.88
	$A \approx (150\,\mathrm{pc})^2$	$A \approx (19\,\mathrm{pc})^2$	...	

Table 2.3: Parameters for the best fits with XDR-, PDR-, and shock-models. The XDR and PDR models are from Meijerink et al. (2007), with the XDR grid extended to $F_X = 510\,\mathrm{erg\,cm}^{-2}\,\mathrm{s}^{-1}$. Two models were employed for the shock-fit: the ME component is modeled with Flower & Pineau Des Forêts (2010), and the HE component with Kaufman & Neufeld (1996) (like in HD12). A is the illuminated area. The χ^2 values apply to the 2 component XDR- and shock- fit, and to the full PDR fit.

2.5 XDR model of the NGC 1068 nucleus

In the previous section we have attributed the HE component of the high-J CO SLED to the northern streamer, at about 30 pc from the nucleus. If this is correct then we have not detected CO emission from the putative torus that is required by AGN unification models. In this section we want to address the following question: what does the upper limit on CO (40-39) tell us about the existence or non-existence of a torus? If there is such a torus, is it reconcilable with the upper limit, and what can be learned about its physical parameters (like size, density, distance from the center)?

In the following sections we model the molecular torus as a semi-infinite slab or as a system of such slabs, with strong irradiation from X-rays. The intrinsic X-ray luminosity $L_{1-100\,\mathrm{keV}} = 10^{43.5}\,\mathrm{erg\,s}^{-1}$ indicates that input fluxes up to $F_X = 10^6\,\mathrm{erg\,cm}^{-2}\,\mathrm{s}^{-1}$ are needed to account for gas as close as ~ 0.5 parsec from the AGN. Differing from the previous section (and from HD12) we here use our own XDR code as described in Bruderer et al. (2012) (including benchmark tests), with updates in Bruderer (2013). This code, originally developed for the analysis of protoplanetary disks, was extended to the higher X-ray input fluxes we need here.

2.5.1 XDR grid

In the model, X-rays with photon energies between 1 and 100 keV deposit energy in the gas, which has two effects: they heat the dust and drive ionization reactions. The code iterates on radiative, thermal, and chemical processes, until all are balanced. From this balanced situation, the gas temperature and CO rotational line emission is written out as a function of distance and column density into the slab.

In a semi-infinite slab model, the observer is located on the same side as the X-ray source. X-rays enter the semi-infinite slab from one side and deposit their energy in the gas. CO is emitted in all directions, but only the CO emission toward the observer is calculated. CO can become optically thick between the point of emission and the observer (we did not assume the gas to have a large velocity gradient); in this case the attenuated CO emission is given. NGC 1068 is however a type-2 AGN, so the gas is located between the observer and the X-ray source. To check whether the location of the observer introduces a large uncertainty in our results, we extracted the optical depths as a function of column density from the XDR code, for all CO lines. With these optical depths, the unattenuated CO emission was calculated as a function of column density, as well as the attenuated CO emission toward an observer on the opposite side of the slab. Indeed, for some combinations of density and X-ray flux, the CO becomes very optically thick and the observed CO emission differs by more than an order of magnitude from one side of the slab to the other. For the parameters that are relevant for this paper however, the difference is at most 30% in CO line flux at column densities $< 10^{25} \, \mathrm{cm}^{-2}$. Another potential issue is geometrical dilution; this is discussed further in Section 2.5.3.

The expected CO emission is calculated for a grid of semi-infinite slabs with densities of $n \in [10^2, 10^{2.5} \, ... \, 10^9] \, \mathrm{cm}^{-3}$ and $F_X \in [10^{-4}, 10^{-3} \, ... \, 10^6] \, \mathrm{erg \, cm}^{-2} \, \mathrm{s}^{-1}$. The input SED is a power law with the shape $F_\nu \propto \nu^{-1}$, which best matches the observed XDR spectrum of NGC 1068 (Pier et al., 1994). We also ran the grid for a softer intrinsic spectrum (spectral index of -2 instead of -1). In this case, the X-ray absorption and CO emission take place within smaller column densities than for the hard X-ray spectrum.

Line absorption by dust particles is not taken into account because this depends strongly on the geometry and viewing angle. Since we do not know the geometry of gas structures in the central few parsecs of NGC 1068, we rather assume no line absorption by dust. This can be done safely up to a column $N_H = 8.5 \times 10^{23} \mathrm{cm}^{-2}$, where the dust becomes optically thick at 66 μm (Draine, 2003). At higher column densities, the results from our model are thus upper limits to the line fluxes (see Section 2.5.4).

In all grid points, the line emission is calculated up to a column of $N_H = 10^{26} \, \mathrm{cm}^{-2}$ into the slab. High-J CO emission arises from a certain combination of density n, X-ray flux F_x, and column density, best represented by the effective ionization parameter ξ_{eff}. ξ_{eff} is calculated from formula 12 in Maloney et al. (1996); $\xi_{eff} = 4\pi \frac{F_x}{n \, N_{22}^{\phi+1}}$, with N_{22} the column density in units of $10^{22} \, \mathrm{cm}^{-2}$, $\phi = (\alpha - 1)/\gamma$, in which $\alpha = -1$ is the spectral index, and $\gamma = 8/3$ is a parameter that reflects that we are interested in the high-energy X-rays (E > 1 keV). The high-J CO lines (around J = 40) are well produced for an effective ionization parameter $\xi_{eff} \approx 0.02$. ξ_{eff} is calculated for three grid points with $n = 10^7 \, \mathrm{cm}^{-3}$, and $F_X = 10^4, 10^5$ or $10^6 \, \mathrm{erg \, cm}^{-2} \, \mathrm{s}^{-1}$, and plotted in Figure 2.4, together with the gas temperature and the H and CO abundances. The central grid point produces most CO(40-39) emission: at higher F_X, the gas remains hot and the CO abundance remains low, while at lower F_X the gas quickly becomes molecular and cools rapidly.

Although H_2 is the main collision partner of CO in a molecular gas, atomic hydrogen also contributes to the collisional excitation of CO if the gas is partly atomic or ionized. Because
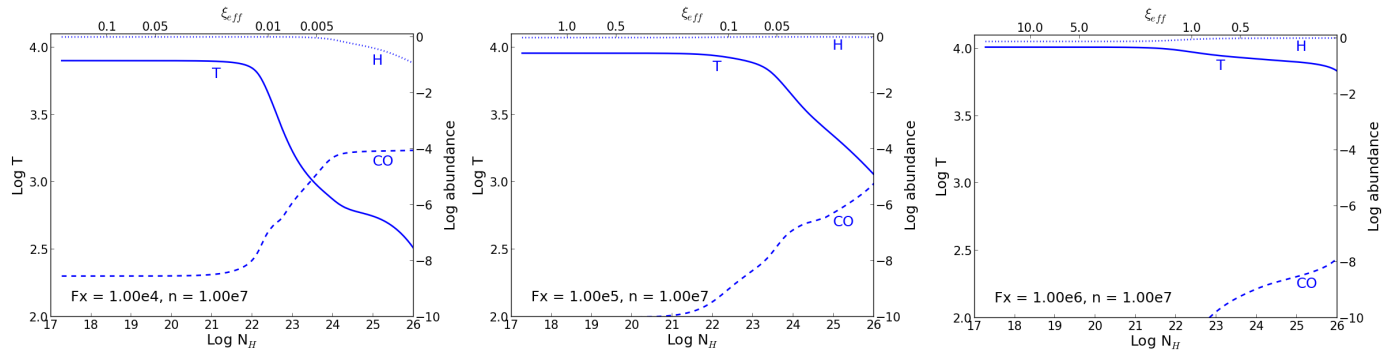
Figure 2.4: Gas temperature, effective ionization parameter, and CO and H abundances are plotted as function of column density into the slab. The density is $10^7\,\mathrm{cm}^{-3}$ in all the figures. Left: $F_X = 10^4\,\mathrm{erg\,cm}^{-2}\,\mathrm{s}^{-1}$, the gas has become molecular around $N_H = 10^{24}\,\mathrm{cm}^{-2}$. Middle: $F_X = 10^5\,\mathrm{erg\,cm}^{-2}\,\mathrm{s}^{-1}$; the gas becomes slowly molecular and produces most CO(40-39) emission around $N_H = 10^{25}\,\mathrm{cm}^{-2}$, with $\xi_{eff} \approx 0.02$ (see Figure 2.5). Right: $F_X = 10^6\,\mathrm{erg\,cm}^{-2}\,\mathrm{s}^{-1}$; even at $N_H = 10^{26}\,\mathrm{cm}^{-2}$, there is too little CO to produce observable CO(40-39) emission.

collision rates between H and CO are currently still uncertain, they are approximated by the H_2 collision rate, scaled with the reduced mass of the colliding particles. The next section treats the CO SLED that results from our model.

2.5.2 An X-ray irradiated slab

A model of a torus with a smooth plane-parallel slab that is intensively radiated with X-rays was already given by KL89, who concluded that most of the torus cooling happens in (very) high J CO lines (with J up to ~ 57). However, a certain column density is required to produce observable CO fluxes, because the gas has a stratified structure: the first layer, through which the X-rays enter the gas, is fully ionized with temperatures of a few thousand Kelvin. The CO forms only further into the slab, and cools the gas rapidly.

In the following discussion the illuminated slab has a covering factor of 0.25 since 20-25% of all AGNs are Compton-thick (Malizia et al., 2009; Burlon et al., 2011) and its illuminating X-ray flux depends solely on the intrinsic luminosity of NGC 1068 ($10^{43.5}\,\mathrm{erg\,s}^{-1}$, assuming an isotropically radiating source) and the distance toward the AGN. The absolute emitted CO line fluxes of these scenarios are subject to large uncertainties (Röllig et al., 2007), especially at high energy levels. One of the reasons for the uncertainties is that the main collision partner for CO, H_2, forms on dust grains. The H_2 abundance thus depends strongly on the dust abundance, its composition, and its temperature, which are all uncertain parameters. Moreover, the dust and gas temperatures decouple in the extreme conditions considered here, with $T_{\mathrm{dust}} \sim$ a few 100 K, and $T_{\mathrm{gas}} \sim$ a few 1000 K. So unlike in the study of protoplanetary disks, where absolute line fluxes can be given within a factor of a few (Bruderer et al., 2012), we adopt an uncertainty of 1 order of magnitude
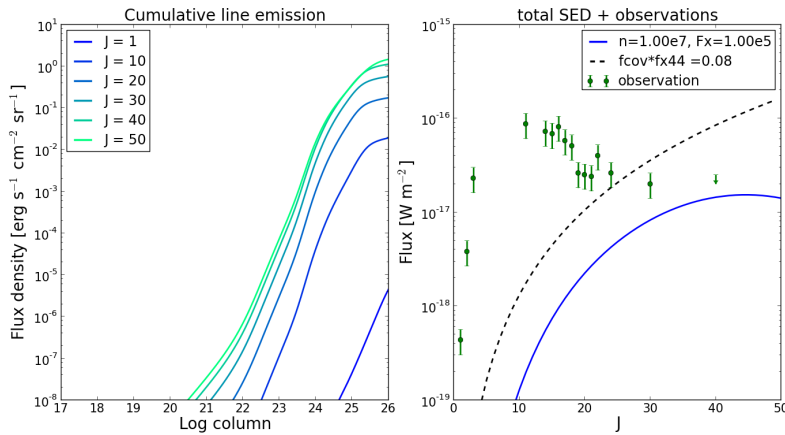
Figure 2.5: Left: Cumulative line emission from an X-ray irradiated slab with a density of $10^7 \, \text{cm}^{-3}$ and $F_X = 10^5 \, \text{erg} \, \text{cm}^{-2} \, \text{s}^{-1}$. Right: the CO SLED from a 8.3 pc^2 sized structure, at a distance of 14.4 Mpc, and with $N_H = 10^{25} \, \text{cm}^{-2}$, is plotted together with the prediction by KL89 with $f_{cov} f_{x44} = 0.08$. The difference between the two models is a factor eight for CO(40-39).

in the modeled line fluxes.

A general discussion on what part of parameter space can be constrained by the upper limit is given in Section 2.6. But first we analyze a simple slab model with parameters based on the water masers described in Gallimore et al. (1996). In this model, the gas has a density $n = 10^7 \, \text{cm}^{-3}$ and an impinging X-ray flux of $10^5 \, \text{erg} \, \text{cm}^{-2} \, \text{s}^{-1}$, because the water masers imply gas densities of $\geq 10^7 \, \text{cm}^{-3}$ at 1.5 pc from the nucleus. These are the same parameters as used by KL89, and with an intrinsic X-ray flux $F_X = 10^{43.5} \, \text{erg} \, \text{s}^{-1}$, they represent a torus with inner radius of 1.6 pc (our intrinsic luminosity and spectral range differs slightly from KL89). Our model prediction of the CO(40-39) flux is a factor a ~ 8 lower than presented in KL89 – with $f_{cov} f_{x44} = 0.08$ to account for a covering factor 0.25 – as can be seen in the right panel of Figure 2.5. The reason is that KL89 assume the high-J CO lines to be optically thick up to J ~ 57, and therefore the luminosity of the line $L_J \propto \nu^3 \propto$ J^3. Instead, we calculate the optical depth as function of column density into the slab, and find that the CO(40-39) line does not become optically thick within $N_H = 10^{25} \, \text{cm}^{-2}$. For larger column densities our model converges toward the KL89 prediction (but needs $N_H > 10^{26} \, \text{cm}^{-2}$ to match it). At $N_H = 10^{24} \, \text{cm}^{-2}$, as used in KL89, the CO(40-39) flux differs by a factor 100 between the 2 models. It clearly matters at what column density the high-J CO lines become optically thick.

The upper limit corresponds to a column density of $N_H = 1.5 \times 10^{25} \text{cm}^{-2}$, which is still similar to the expected obscuring gas column density in NGC 1068 (Bauer et al., 2014). So although the CO(40-39) line traces the gas we are interested in ($n \sim 10^7 \, \text{cm}^{-3}$, $N_H \sim 10^{25} \, \text{cm}^{-2}$, located within a few pc of the AGN), the observation did not reach the required sensitivity to constrain the gas distribution.
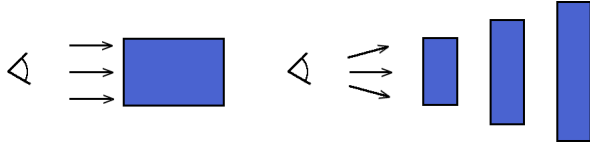
Figure 2.6: Schematic overview of the torus models. The cartoon on the left represents one slab with a column density $10^{25}\,\mathrm{cm}^{-2}$, the cartoon on the right a three-layer model with a volume filling factor of 0.5. The column through these three slabs is also $10^{25}\,\mathrm{cm}^{-2}$, but the layers have been scaled in height to keep a constant covering factor. The density of all the slabs is constant, while the X-ray flux decreases with distance from the central source to account for geometrical dilution.

2.5.3   A clumpy cloud system

In the above scenario the gas is distributed smoothly. There are however indications that the dust in a torus is distributed in clouds, and most recent torus models treat a clumpy, rather than a smooth, dust distribution (see Hönig et al. (2006) for such a model of NGC 1068).

Assuming that also the gas could be distributed in clouds, we approximate a clumpy torus with 10 plane-parallel slabs. The slabs have the same density as in our previous example and the layer closest to the source receives an X-ray input flux of $10^5\,\mathrm{erg\,cm}^{-2}\,\mathrm{s}^{-1}$. All other layers lie at larger distance from the source, and are obscured by the intermediate layers, as shown in Figure 2.6. The total column density along the line of sight to the source is $10^{25}\,\mathrm{cm}^{-2}$, and the illuminated surface of the slabs increases with distance to the source, to keep a covering factor of 0.25. The total amount of gas has therefore increased with respect to the previous example.

The first layer receives the highest X-ray flux, while layers further away from the center receive lower X-ray fluxes due to geometrical dilution and due to X-ray absorption in the intermediate layers. The geometrical dilution is accounted for by taking the grid point with the X-ray flux that corresponds to the geometrically diluted – but unattenuated – X-rays from the central source. In case this flux lies between two grid points, the CO SLED is interpolated between these grid points. Each layer thus has a cumulative line distribution attached to it (as shown in the left panel in figure 2.5), from which the line emission is extracted between two column densities. For example, the emission of the first layer could thus be extracted from $N_H = 0 \rightarrow 10^{24}\,\mathrm{cm}^{-2}$, and that of the second from $N_H = 10^{24} \rightarrow 2 \times 10^{24}\,\mathrm{cm}^{-2}$. This accounts for the X-ray attenuation by intermediate layers because the XDR model calculates the X-ray attenuation as function of column density.

The 10 slabs have column densities of $10^{24}\,\mathrm{cm}^{-2}$. The distance between the slabs is determined by the volume filling factor Φ_V: $\Phi_V = 0.5$ implies that a 0.03 pc thick layer is followed by a 0.03 pc thick gap. Figure 2.7 shows the CO SLED with $\Phi_V = 1$, 0.5, and 0.2. The three plots look very similar, there is no sign of a lower output flux or change in SLED for lower Φ_V. The reason is that the increasing layer surface compensates the geometrical
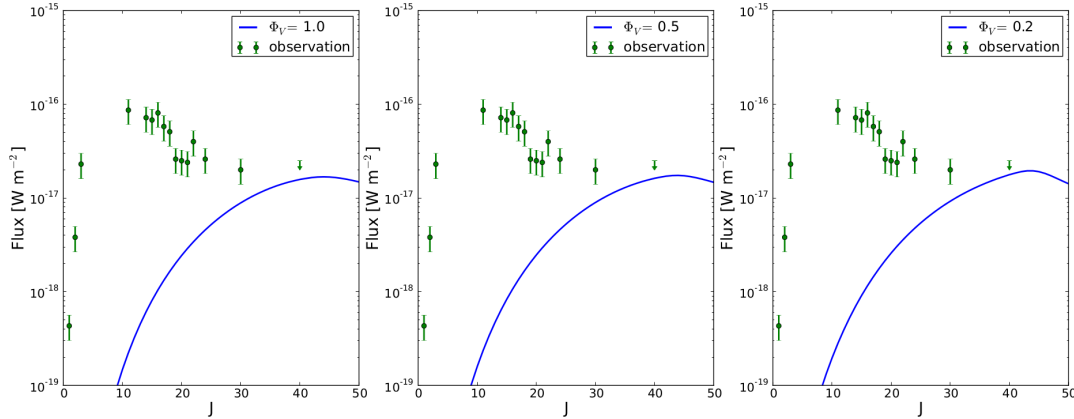
Figure 2.7: 10 plane parallel slabs approximate a torus with $\Phi_V = 1$, 0.5, or 0.2. The total column density through the slabs is $10^{25}\,\mathrm{cm}^{-2}$. Because the increasing slab size compensates the geometrical dilution, the total SLED looks similar in these three cases.

dilution (both $\propto r^2$). Only when Φ_V becomes very small ($\Phi_V \sim 0.05$), the outermost layers are located so far from the X-ray source that the CO SLED changes significantly. We therefore conclude that the volume filling factor is of little importance in our case.

It is also worth noting that the layered model with $\Phi_V = 1$ looks very similar to the single slab model that was presented in Section 2.5.2. Geometrical dilution is thus not important for the grid point with $n = 10^7\,\mathrm{cm}^{-3}$, $F_X = 10^5\,\mathrm{erg\,cm}^{-2}\,\mathrm{s}^{-1}$ and $N_H = 10^{25}\,\mathrm{cm}^{-2}$. The same applies to the other grid points that are used in this paper.

2.5.4   Line absorption by dust

Figure 2.5 shows that column densities of $\sim 10^{25}\,\mathrm{cm}^{-2}$ are needed to match the CO(40-39) upper limit in NGC 1068. Within such high column densities, dust absorbs significant fractions of the line fluxes, and especially affects the high-J CO lines.

For simplicity, we assume that the gas and dust follow the same distribution, and that the dust resembles galactic dust. The dust cross-sections are taken from Draine (2003) and follow $\sigma[\mathrm{cm}^{-2}\mathrm{per\ H\text{-}atom}] \propto \lambda^{-2}$ at the relevant wavelengths [2]. In this case the position of the observer with respect to the slab does matter for the final SLED. The right panel in Figure 2.8 shows the CO SLED when the torus is located between the X-ray source and the observer, taking line absorption by dust into account. The modeled CO(40-39) emission decreased by a factor 10. Because we do not know the real dust distribution in NGC 1068, we do not include line absorption by dust in the remainder of this paper, but keep in mind that it can attenuate the CO(40-39) flux by a factor of 10.

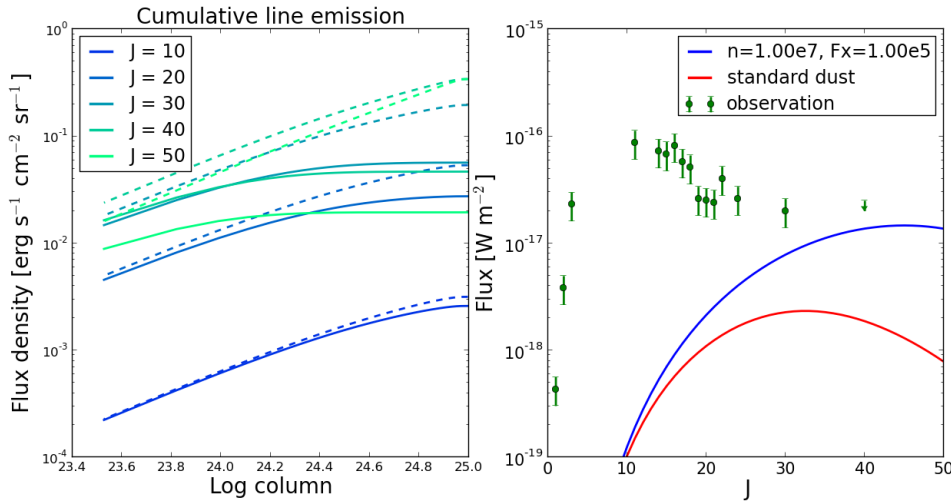[2]Actual cross-sections for Milky Way, R_V= 3.1 are found on: `http://www.astro.princeton.edu/~draine/dust/dustmix.html`

Figure 2.8: Line absorption by dust in a slab with $n = 10^7$ cm^{-3} and $F_X = 10^5$ erg cm^{-2} s^{-1}, calculated for a torus located between the X-ray source and the observer. Left panel: the broken lines indicate unattenuated line emission, while the solid lines indicate attenuated line emission. Right panel: dust attenuates the CO(40-39) emission by a factor of 10.

2.6 Results and Discussion

A smooth molecular torus (with $n = 10^7$ cm^{-3}, at 1.6 pc from a $L_{1-100\,\text{keV}} = 10^{43.5}$ erg s^{-1} source and with a column density $N_H = 1.5 \times 10^{25}$ cm^{-2}) could have been observable in CO(40-39) within the sensitivity of the PACS observation. But the uncertainty in the model at these high-J lines is an order of magnitude. Moreover the dust could attenuate the CO(40-39) line flux by a factor 10, so this scenario is not strongly constrained by the upper limit.

Can we exclude anything else? Is there any grid point where the CO emission exceeds the upper limit by more than an order of magnitude? Figure 2.9 shows the cumulative CO(40-39) emission as function of column density and $\frac{F_X}{n}$. At $N_H > 10^{25}$ cm^{-2} the uncertainty rises above 30% for a gas located between the X-ray source and the observer. Line absorption by dust is not taken into account. The white broken line illustrates where the observed upper limit is matched for an illuminated area of $4\pi r^2$, with $r = 5$, 1.6, or 0.5 pc, as given in Table 2.4.

In all cases, the maximum emission arises at column densities $\geq 10^{25}$ cm^{-2}, and at $-2 < \log(\frac{F_X}{n}) < -1.5$. So our initial analysis with $n = 10^7$ cm^{-3} and $F_X = 10^5$ erg cm^{-2} s^{-1} already produced CO(40-39) very efficiently, and most grid points will therefore not be constrained by the upper limit. Sticking to a total column density of 10^{25} cm^{-2}, there are four grid points that produce observable amounts of CO(40-39) emission: those with $n = 10^8$ and $F_X = 10^6$, $n = 10^7$ and $F_X = 10^5$, $n = 10^6$ and $F_X = 10^4$, and $n = 10^5$ cm^{-3} and $F_X = 10^3$ erg cm^{-2} s^{-1}. We investigate here what sizes the gas structures with these parameters must have to match the CO(40-39) upper limit. The slab with $n = 10^5$ cm^{-3}
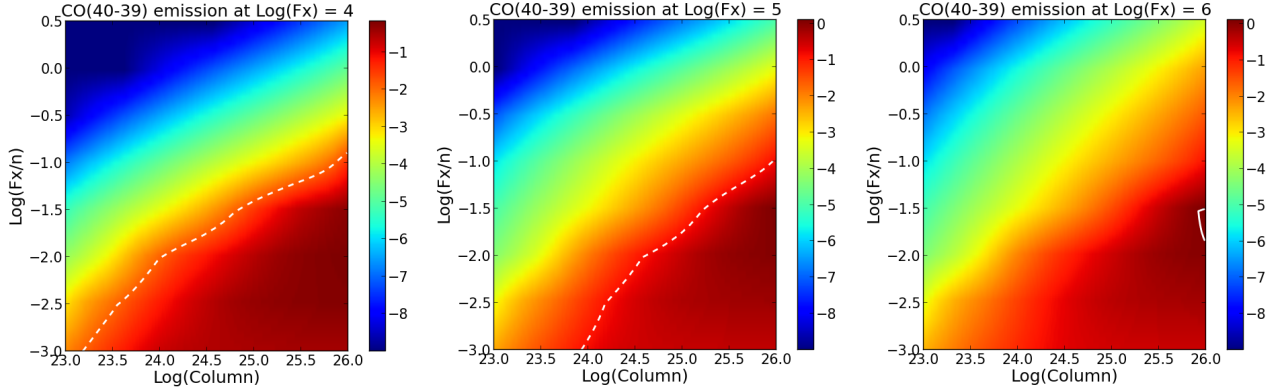
Figure 2.9: Cumulative CO(40-39) emission in $\mathrm{erg\,s^{-1}\,cm^{-2}\,sr^{-1}}$. The white broken line indicates where an object with area $4\pi r^2$, with $r = 5$ pc, 1.6 pc, or 0.5 pc respectively (see Table 2.4), matches the upper limit of $2 \times 10^{-17}\,\mathrm{W\,m^{-2}}$. Taking $N_H = 10^{25}\,\mathrm{cm^{-2}}$ and $\log(\frac{F_X}{n}) = -2$, the surface covering factor that is needed to match the upper limit is given in Table 2.4.

and $F_X = 10^3\,\mathrm{erg\,cm^{-2}\,s^{-1}}$ is however excluded from the analysis, because the CO lines become optically thick and the observed CO emission depends strongly on the position of the observer with respect to the slab.

Assuming a toroidal gas distribution, with $N_H = 10^{25}\mathrm{cm^{-2}}$, we calculate the surface covering factor (1 for a $4\pi\,r^2$ shell covered with gas) that is needed to match the CO(40-39) upper limit. The results are given in Table 2.4, and are interpreted as follows:

- A gas layer with $n = 10^8\,\mathrm{cm^{-3}}$ at 0.5 pc from the AGN needs a covering factor of 4.5 to be observable, which is not physical. Therefore, such a compact component could not be observed in CO rotational lines at the current sensitivity, even if it has a column high enough to completely block the X-rays from our view.

- The slabs placed at 1.6 and 5 pc do give reasonable covering factors of 0.4 and 0.06, respectively.

MIDI observations of the hot dust in the NGC 1068 nucleus are resolved in two central components with scales of 0.5-3 pc (López-Gonzaga et al., 2014), and a third component that is offset. If the gas is distributed at scales similar to these central components, the scenario with a radius of 5 pc is not valid. This leaves only one scenario left under which the CO(40-39) could be matched: the one that was presented in Section 2.5.2.

If the CO(40-39) line were detected at the upper limit value, it would trace gas between 1.6 and 5 pc from the AGN, with densities $\sim 10^6 - 10^7\,\mathrm{cm^{-3}}$, which covers at least 6% to 40% of a shell around the AGN. Column densities of $10^{25}\,\mathrm{cm^{-2}}$ are required. Only a few AGN satisfy this condition, and the detection of CO(40-39) in an XDR would point to very high column densities (although this line can be observed at lower column densities in shocks; Herczeg et al. (2012)). Currently, there are no instruments that can perform an

F_X $(\mathrm{erg\,cm^{-2}\,s^{-1}})$	n $(\mathrm{cm^{-3}})$	Inner radius (pc)	Outer radius (pc)	Covering factor (0-1)	Required emission $(\mathrm{erg\,s^{-1}\,cm^{-2}\,sr^{-1}})$
10^6	10^8	0.5	0.53	4.5	1.18
10^5	10^7	1.6	1.9	0.4	0.118
10^4	10^6	5	8.2	0.06	0.0118

Table 2.4: Surface covering factors required to fit the J = 40 upper limit face value (line absorption by dust is not taken into account). The third column in the table lists the inner radius of the torus, assuming that $L_{1-100\,\mathrm{keV}} = 10^{43.5}\,\mathrm{erg\,s^{-1}}$. The outer radius follows from a column of $10^{25}\,\mathrm{cm^{-2}}$. A $10^8\,\mathrm{cm^{-3}}$ density slab located at 0.5 pc from the AGN, needs a covering factor > 1 to be observable, which is not physical. The scenarios with $10^7\,\mathrm{cm^{-3}}$ and $10^6\,\mathrm{cm^{-3}}$ could be observable in CO(40-39).

even deeper observation of this line, but it may be possible with future observatories such as the Space Infrared Telescope for Cosmology and Astrophysics (SPICA).

2.7 Summary and Conclusion

The deep observation on the CO(40-39) line in the NGC 1068 central region resulted in an upper limit of 2×10^{-17} W m^{-2}, more than 10 times lower than the previous upper limit (HD12). The upper limit does not change the previous conclusions, as to what mechanism heats the highly excited component in the CO SLED (HD12): all models (shocks, PDR, XDR) that fit the highest excited component in the observed SLED, are consistent with the new J = 40 upper limit.

We extended an XDR code, used for protoplanetary disks, with densities up to 10^9 cm^{-3} and input fluxes up to $F_X = 10^6\,\mathrm{erg\,cm^{-2}\,s^{-1}}$ to investigate in how far the upper limit constrains the gas distribution around the AGN. The spectral index of the modeled X-ray spectrum is -1, and the slabs have column densities of $10^{26}\,\mathrm{cm^{-2}}$. In the semi-infinite slab model, the X-ray source and the observer are located on the same side of the slab. The observed CO(40-39) flux differs by at most 30% if the observer is placed at the opposite side of the slab, as long as $N_H \leq 10^{25}\,\mathrm{cm^{-2}}$. The difference increases however rapidly for higher column densities. We investigated the CO emission from a gas with a density of $10^7\,\mathrm{cm^{-3}}$, $F_X = 10^5\,\mathrm{erg\,cm^{-2}\,s^{-1}}$, which peaks around J = 40. The modeled CO(40-39) flux matches the upper limit for $N_H = 1.5 \times 10^{25}\,\mathrm{cm^{-2}}$.

A line detected at the upper limit value would trace gas with densities $\sim 10^6 - 10^7\,\mathrm{cm^{-3}}$, at 1.6-5 pc from the AGN, with column densities of at least $10^{25}\,\mathrm{cm^{-2}}$, and surface covering factors of at least $6\% - 40\%$. Especially because of the high column density required to be observable within the PACS sensitivity, we expect to see only few AGNs with CO(40-39) emission.

Because tori are thought to be clumpy structures rather than a smooth medium, we approximated a clumpy distribution with 10 slabs and volume filling factors 1, 0.5, and 0.2. This did not change the CO SLED at CO(40-39), because the increasing layer surface

compensates the geometrical dilution. A difference is only seen when $\Phi_V = 0.05$.

On the other hand, line absorption by dust is a very important effect. Dust attenuates the high-J CO lines, which makes a difference of a factor of 10 in the modeled CO(40-39) line flux at a column density $N_H = 10^{25}\,\mathrm{cm^{-2}}$.

In HD12 we speculated that there might be no molecular torus, based on the non-detection of several high-J CO lines. But we did not have an XDR code that addresses all the caveats and uncertainties that are described above. With our new model, which is adapted to the high densities and X-ray fluxes in an AGN torus, considering the position of the observer and line absorption by dust, we conclude that the non-detection of CO(40-39) is still consistent with the existence of a molecular torus.

2.8   Acknowledgements

Chapter 3

Broad [CII] line wings as tracer of molecular and multi-phase outflows in infrared bright galaxies

3.1   Introduction

Feedback via powerful winds is thought to play a critical role in galaxy evolution. Without any form of feedback, galaxy evolution models overpredict star formation in the early universe, and spheroid dominated remnants would predominate in the current universe, which is not observed (Cole, 1991). In order to match observations, current models implement, among other things, gas inflows from outside the halo and feedback from stars and active galactic nuclei (AGNs). The output is then compared to observables like the galactic stellar mass function, the Tully-Fisher relation, the mass-metallicity relation, and the apparent co-evolution of the central Black Hole (BH) mass with the stellar mass (Murray et al. (2005); Sales et al. (2010); Fabian (2012); Vogelsberger et al. (2013); Heckman & Best (2014), also see Silk (2011) for a short review on this topic). Negative feedback, in the form of winds or outflows, is usually required to match the observations.

In the local universe, outflows have been observed in all types of galaxies and in different gas phases. Ionized gas outflows have been observed in dwarf galaxies (Marlowe et al., 1995; Martin, 1998) and Seyfert 2 AGNs (Cecil et al., 1990; Harrison et al., 2014). In ultraluminous infrared galaxies (ULIRGs), outflows are observed in several phases: ionized (Spoon & Holt, 2009; Westmoquette et al., 2012; Arribas et al., 2014), molecular (Sakamoto et al., 2009; Fischer et al., 2010; Feruglio et al., 2010; Sturm et al., 2011a; Veilleux et al.,

2013; Spoon et al., 2013; Cicone et al., 2014) and atomic (Rupke & Veilleux, 2013b). Morganti et al. (2005) discuss neutral gas outflows in radio galaxies. Possible drivers of the outflows are stars and/or AGN. Theoretically, star formation has the power to remove significant amounts of gas from a Milky-Way sized galaxy (Efstathiou, 2000; Hopkins et al., 2012). Indeed, star formation has been observed to drive outflows in the form of H-alpha bubbles above disk galaxies (Rand, 1996). Blue-shifted absorption of Na I D and Mg II in star-forming galaxies may also be driven by star formation (Heckman et al., 2011; Diamond-Stanic et al., 2012), although the star formation rate must reach a certain threshold before any correlations with the outflow properties become apparent (Heckman et al., 2015). In massive galaxies however, star formation alone may not be sufficient to power the outflows which can reach velocities $>> 500\,\mathrm{km\,s^{-1}}$. In ULIRGs outflow velocities can reach $1500\,\mathrm{km\,s^{-1}}$ and AGN are the most probable driver (e.g. Sturm et al. (2011a); Cicone et al. (2014); Spoon et al. (2013); Veilleux et al. (2013)).

Detections of such outflows at high redshift would confirm that feedback also played an important role in the early universe. These outflows have been detected at $z > 1$, in type 2 AGN (Alexander et al., 2010; Nesvadba et al., 2011; Harrison et al., 2012; Cano-Díaz et al., 2012), in massive star-forming galaxies (Weiner et al., 2009; Banerji et al., 2011; Genzel et al., 2014; Förster Schreiber et al., 2014) and in radio galaxies (Nesvadba et al., 2008), however mostly in ionized or atomic gas. Since the molecular phase contributes significantly to the total mass, observations of molecular outflows at high redshift would be most helpful in constraining the role of feedback in the early universe. Candidates for these observations are CO rotational lines and OH rotational lines in absorption, preferably observed with sensitive telescopes like ALMA or NOEMA. However, molecular outflows have not yet been detected in high-J CO lines, and low-J CO lines quickly shift out of the ALMA and NOEMA bands.

The ground state OH $^2\Pi_{3/2}$ $5/2 \rightarrow 3/2$ transition at $119\,\mu\mathrm{m}$, or OH119 for short, probes molecular and to a lesser extent atomic gas (Meijerink & Spaans, 2005). OH119 becomes observable with ALMA at $z = 2$ (in the $450\,\mu\mathrm{m}$ atmospheric window in Band 9), but a high signal-to-noise ratio (S/N) and bright continuum is needed to detect the outflow in absorption. ULIRGs are intrinsically bright in the far infrared (FIR), providing the continuum for the OH119 absorption, but not all galaxies have such a bright FIR continuum. Detections of blue-shifted OH119 emission are possible but rare at high redshift (Riechers et al., 2014). Direct observations of molecular outflows at high redshift are therefore challenging.

As an alternative, the collisionally excited fine structure transition of C$^+$ ^{2}P$_{3/2}$ $\rightarrow^2$ P$_{1/2}$ at rest frame wavelength of 157.741 μm (hereafter [CII]) may be used. It is one of the brightest lines in spectra of star-forming galaxies, as it is the dominant coolant of the interstellar medium over a wide range of physical conditions. Most [CII] emission is thought to arise in Photodissociation Regions (PDRs) around starforming regions, where the intensity of $> 13.6\,\mathrm{eV}$ photons has dropped sufficiently for hydrogen to stay atomic, while carbon remains ionized (carbon has a slightly lower ionization potential of 11.26 eV). Pineda et al. (2013) find that in our galaxy about 50% of [CII] emission arises from these PDRs, about 30% arises from CO-dark H_2 gas, about 20% from atomic gas, and only very

little from hot ionized gas. [CII] shifts into the $450\,\mu$m windows of ALMA at redshifts $z = 1.85$, and in the $0.8\,mm$ band of NOEMA at $z = 4$. High velocity outflows appear as broad wings in the [CII] line profile, and such broad wings have been detected at high redshift, for example in the QSO SDSS J1148+5251 $z = 6.4$ (Maiolino et al., 2012; Cicone et al., 2015).

In this paper, we investigate how well [CII] traces the molecular outflows in ULIRGs, by comparing the outflow velocity and mass retrieved from *Herschel*[1]/PACS observations of [CII] and OH119. The ULIRGs are all gas-rich and most contain an AGN. A short description of the sample is given in Section 3.2. We then cover the PACS data reduction in Section 3.3. The [CII] line profiles have been fitted with Gaussian line profiles, and the FHWM of the broad component is compared to the OH blue-shifted velocity in Section 3.4. In the same section we compare the FWHM of the broad [CII] component with the AGN luminosity, with the Na I D blue-shifted absorption velocity and with CO(1-0) line profiles. A discussion of the outflow masses and possible connections between the different phases follows in Section 3.5. We adopt $H_0 = 70\,\mathrm{km\,s^{-1}\,Mpc^{-1}}$ throughout this paper.

3.2   Sample description

The sample consists of all 22 local ($z < 0.1$) ULIRGs from the IRAS Revised Bright Galaxy Sample (Sanders et al., 2003); these are objects with $L_{8-1000\,\mu m} \geq 10^{12}\,L_{\odot}$. IRAS F09111-1007 lies above this luminosity cutoff, but is faint in the PACS range and therefore excluded. We include, however, NGC 6240 and UGC 5101 which are formally slightly below this cutoff, but in any relevant aspect for this study have similar charateristics as the rest of the sample. See Table 3.1 for the redshifts, coordinates and AGN fractions of the sample. The AGN fractions are estimated using the ratio of the flux densities at 30 μm and 15 μm, f_{30}/f_{15}, as measured with the Spitzer Infrared Spectrograph, following Veilleux et al. (2009a).

Because ULIRGs represent the IR-bright phase of mergers of gas-rich galaxies (Sanders & Mirabel, 1996), several objects in our sample have resolved double nuclei related to interaction and merging. All known double nuclei are covered completely by our PACS observations.

3.3   Observations and data reduction

Observations were made with the Photodetector Array Camera and Spectrometer (PACS) (Poglitsch et al., 2010), on board the Herschel Space Observatory (Pilbratt et al., 2010). Both the OH $119\,\mu$m and the [CII] $158\,\mu$m spectra have been obtained as part of the *Herschel* guaranteed time key program SHINING (PI: E. Sturm). We reduced and analyzed the OH data in Veilleux et al. (2013), (V13). Because the OH119 line appears either in

---

[1]Herschel is an ESA space observatory with science instruments provided by European-led Principal Investigator consortia and with important participation from NASA.

Name	Alternative Name	z	R.A.	Decl.	α_{AGN} (%)	$\log(L_{\mathrm{AGN}})$
IRAS F05189-2524	...	0.0426	05:21:01.4	-25:21:46	72	12.07
IRAS 07251-0248	...	0.0876	07:27:37.5	-02:54:55	30	11.92
IRAS F08572+3915	...	0.0584	09:00:25.0	39:03:56	70	12.05
IRAS 09022-3615	...	0.0596	09:04:12.8	-36:27:02	55	12.09
UGC 5101	IRAS F09320+6134	0.0394	09:35:48.8	61:21:22	56	11.8
IRAS F10565+2448	...	0.0431	10:59:17.4	24:32:38	47	11.77
IRAS F12112+0305	...	0.0733	12:13:47.4	02:48:34	18	11.63
Mrk 231	IRAS F12540+5708	0.0422	12:56:15.0	56:52:17	81	12.51
IRAS 13120-5453	...	0.0308	13:15:06.2	-55:09:24	33	11.83
Mrk 273	IRAS F13428+5608	0.0378	13:44:41.8	55:53:14	34	11.74
IRAS F14348-1447	...	0.0830	14:37:37.3	-15:00:20	17	11.64
IRAS F14378-3651	...	0.0676	14:40:57.8	-37:04:25	21	11.5
IRAS F15250+3608	...	0.0552	15:26:59.9	35:58:34	42	11.73
Arp 220	IRAS F15327+2340	0.0181	15:34:57.1	23:30:10	5.8	10.98
NGC 6240	IRAS F16504+0228	0.0245	16:52:58.6	02:24:03	56	11.65
IRAS F17207-0014	IRAS 17208-0014	0.0428	17:23:21.4	-00:17:00	≤ 5	≤ 11.15
IRAS F19297-0406	...	0.0857	19:32:22.1	-04:00:02	23	11.81
IRAS 19542+1110	...	0.0624	19:56:35.4	11:19:03	26	11.52
IRAS F20551-4250	...	0.0430	20:58:27.4	-42:38:57	57	11.87
IRAS F22491-1808	...	0.0778	22:51:49.0	-17:52:27	14	12.05
IRAS F23128-5919	ESO 148-IG 002	0.0446	23:15:46.6	-59:03:14	63	11.89
IRAS F23365+3604	...	0.0645	23:39:01.7	36:21:14	45	11.87

Table 3.1: Redshifts, coordinates and AGN fractions and luminosities of the observed sample. AGN fractions are calculated from f_{30}/f_{15}, as described in Veilleux et al. (2009a).

pure absorption, pure emission, or as a P-Cygni profile, the spectra were fitted with an absorption component, an emission component, or both. (21/22) spectra have absorption features, which are mostly blue-shifted. We will use the velocities of the absorption features of OH in our analysis using the object's v_{50}(abs), v_{84}(abs) and v_{max}(abs) measured by V13 (see Table 3.2). v_{50}(abs) is the median velocity of the fitted absorption profile, i.e. 50% of the flux arises above (from velocities more positive than) v_{50}(abs), v_{84}(abs) is the velocity above which 84% of the absorption takes place, and v_{max}(abs) is the velocity, above which all absorption takes place. v_{max}(abs) however depends strongly on the fit to the continuum and the signal to noise ratio, and this introduces typical uncertainties of $\pm 200 \, \mathrm{km \, s^{-1}}$. We characterise the molecular outflows by their blue-shifted absorption of a FIR continuum. Therefore, only gas along our line of sight to the ULIRG center is traced. The P-Cygni profiles in OH119 and the large number of objects with blue-shifted OH absorption led Sturm et al. (2011a) and Veilleux et al. (2013) to the conclusion that the outflows are isotropic, or have at least a large opening angle. Because [CII] appears in emission, such an isotropic outflow would become visible as blue-shifted and red-shifted wings in the line profile.

The [CII] observations were made in PACS range scan mode with a $2600 \, \mathrm{km \, s^{-1}}$ velocity range. Because of the instanteneous coverage of $\sim 1650 \, \mathrm{km \, s^{-1}}$, the total spectral range is from -2950 to $+2950 \, \mathrm{km \, s^{-1}}$, with decreasing S/N toward the edges. The data reduction was done using the standard PACS reduction and calibration pipeline included in HIPE 13, with upsample and oversample set to 2 (resulting in $60 \, \mathrm{km \, s^{-1}}$ sampling in the spectral direction).

We extracted both the point source corrected spectrum from the central spatial pixel (spaxel; one spaxel covers $(9.4'')^2$ on-sky) and the point source corrected sum of the central 9 spaxels. Although the central spaxel has the best signal to noise ratio, the [CII] emission might be slightly extended, or the telescope badly pointed, in which case the central 9 spaxels were used (Table 3.3).

The pointing was verified with a footprint plot, where a raster of the spectroscopic observations is overlaid on a PACS photometry map with higher spatial resolution. The source was not well centered on the central spaxel in four cases (F10565+2448, F12112+0305, 19542+1110, F23128-5919). In five other cases the final spectrum was extracted from the central 9 spaxels because the broad wings in the [CII] line profile differ from the central spaxel, hinting at slightly extended [CII] emission. Among these are the sources with double nuclei 08572+3915, separated by $6''$, and IRAS 23128-5919, separated by $4.5''$ (Surace et al., 1998; Zenner & Lenzen, 1993). This choice does not affect the line fluxes much, because the central spaxel's flux is scaled to the (point source corrected) 9 spaxel flux, to account for the telescope Point Spread Function (PSF; $13''$ at 158 μm) and minor mispointings. The uncertainty in the line fluxes is 10% for flux densities > 1 Jy, but could be $\sim 30\%$ for any faint wings.

Name	OH v_{50} (km s^{-1})	OH v_{84} (km s^{-1})	OH $v_{\max}$ (km s^{-1})	Na I D range (km s^{-1})	OH mass ($10^8 M_\odot$)
IRAS F05189-2524	-327	-574	-850	-402 to -92 (2)	1.27
IRAS 07251-0248	-63	-255	-550	...	...
IRAS F08572+3915	-489	-832	-1100	700 to -1000 (3)	0.49
IRAS 09022-3615	-153	-297	-650	...	...
UGC 5101	-9	-225	-1200	-16 to 11 (1)	...
IRAS F10565+2448	-267	-489	-950	-309 to -141 (1)	2.99
IRAS F12112+0305	-117	-237	-400	...	...
Mrk 231	-237	-610	-1500	-386 (2)	6.66
IRAS 13120-5453	-195	-520	-1200	...	1.91
Mrk 273	-201	-495	-750	29 (2)	1.27
IRAS F14348-1447	-291:	-508	-900	...	15.2
IRAS F14378-3651	-219	-556	-1200	...	0.91
IRAS F15250+3608	189	-21	...	...	...
Arp 220	21	-153	-700	...	...
NGC 6240	-207	-544	-1200	-99 to -74 (1)	...
IRAS F17207-0014	51	-165	...	-298 to 27 (1)	...
IRAS F19297-0406	-231	-532	-1000	-413 to -114 (4)	...
IRAS 19542+1110	-93:	-489:	-700	...	...
IRAS F20551-4250	-381	-748	-1200	...	0.91
IRAS F22491-1808	99	3::	...	...	...
IRAS F23128-5919	...	...	...	...	...
IRAS F23365+3604	-243	-604	-1300	-384 $\pm$ 96 (4)	5.34

Table 3.2: OH data adopted from V13. Negative velocities indicate blue-shifted absorption, positive values indicate red-shifted absorption. The uncertainties on the OH velocities are typically $50\,\mathrm{km\,s^{-1}}$, unless the value is followed by a colon (when the uncertainty is $50-150\,\mathrm{km\,s^{-1}}$), or a double colon (when the uncertainty is larger than $150\,\mathrm{km\,s^{-1}}$). $v_{\max}$(abs) values have typical uncertainties of $200\,\mathrm{km\,s^{-1}}$. References for Na I D data: (1) Rupke et al. (2005b) (2) Rupke et al. (2005a) (3) Rupke & Veilleux (2013a) (4) Martin (2005) OH masses are preliminary, final results will be published in González-Alfonso (2016, submitted).

Name	OBSID	Extraction Spaxels	FWHM $(\mathrm{km\,s^{-1}})$	1σ error $(\mathrm{km\,s^{-1}})$	L_{outflow} $(10^8 L_\odot)$	M_{outflow} $(10^8 M_\odot)$
IRAS F05189-2524	1342219442	central	1213	412	0.68	1.45
IRAS 07251-0248	1342207825	central	...	502	...	...
IRAS F08572+3915	1342208952	3×3	1567	71	0.63	1.34
IRAS 09022-3615	1342209403	central	693	1	9.28	19.86
UGC 5101	1342208949	3×3	1158	394	0.6	1.28
IRAS F10565+2448	1342207788	3×3	882	1	2.01	4.29
IRAS F12112+0305	1342210832	3×3	...	161	...	...
Mrk 231	1342186811	central	940	8	1.48	3.18
IRAS 13120-5453	1342214629	central	1787	601	0.62	1.33
Mrk 273	1342207802	central	852	295	1.85	3.95
IRAS F14348-1447	1342224242	3×3	887	1	5.06	10.82
IRAS F14378-3651	1342204338	central	...	222	...	...
IRAS F15250+3608	1342213752	central	...	120	...	...
Arp 220	1342238930	central	...	173	...	...
NGC 6240	1342216623	3×3	934	29	8.23	17.62
IRAS F17207-0014	1342229693	central	...	177	...	...
IRAS F19297-0406	1342208891	central	1025	120	4.13	8.83
IRAS 19542+1110	1342208916	3×3	...	122	...	...
IRAS F20551-4250	1342208934	3×3	768	22	1.41	3.01
IRAS F22491-1808	1342211825	central	409	158	1.98	4.23
IRAS F23128-5919	1342210395	3×3	1027	18	2.27	4.87
IRAS F23365+3604	1342212515	central	...	106	...	...

Table 3.3: [CII] observations: PACS obsid, the spaxels from which the spectrum was extracted, the average [CII] broad component FHWM after subtracting $240\,\mathrm{km\,s^{-1}}$ in quadrature (see Appendix A), the error as explained in Section 3.4.1, the luminosity of the [CII] broad component and the total neutral gas mass as described in Section 3.5.1. If no broad component is found, the error is the FHWM of the narrow component divided by 3. Outflow masses above $10^9 M_\odot$ should be regarded as upper limits because the outflow emission is contaminated by emission from the host galaxy.

3.4   Analysis and results

More than half of all objects in our sample have broad wings in [CII] (14/22), as shown in the figures in Appendix A. Usually the wings appear both red-shifted and blue-shifted from the host galaxy, resulting in a symmetric line profile. This is expected if [CII] traces an outflow with a large opening angle, which looks rather like an expanding shell than a single blob. We will now assume that all OH outflows have a large opening angle, so that we can compare the blue-shifted velocity of the OH absorption with the full width at half maximum (FWHM) of the [CII] outflow.

3.4.1   Gaussian fits to the [CII] spectra

We have attempted to fit two Gaussian components (a narrow and a broad one) to the [CII] spectra. This should separate host galaxy emission from outflow emission. In most cases it is clear whether a broad component improves the fit or not. In case of doubt, we identify the best fit based on the reduced χ^2 value, i.e. we deem an outflow is present when the reduced χ^2 value of the two-component fit is lower than that of the one-component fit. We also visually inspect the fits to make sure that the second Gaussian fits the broad wings, not the central component. Figure 3.6 in Appendix A shows the fits overplotted on the [CII] line profiles, while Table 3.5 lists the Gaussian fits and their parameters.

The spectral resolution of PACS is $\sim 240\,\mathrm{km\,s^{-1}}$ at $158\,\mu\mathrm{m}$. Any Gaussian fit with a FWHM below $240\,\mathrm{km\,s^{-1}}$ is therefore rejected. The PSF in PACS is not perfectly Gaussian, but it has no wings that could be confused with an outflow. In some objects, the fit to the continuum significantly affects the FWHM of the second component. Ideally, one would like to take the continuum far away from the systemic velocity of the host galaxy, in order to prevent the removal of broad wings. But the signal to noise ratio drops at (absolute) velocities above $1300\,\mathrm{km\,s^{-1}}$. Faint wings extending to $> 1300\,\mathrm{km\,s^{-1}}$ can therefore not be reliably observed in the spectra. The fits have been done twice in order to estimate the error introduced in our method: once fitting the continuum close to the line, with the potential danger of removing the broad wings, and once fitting the continuum far away from the line, leaving plenty of room for the broad wings. We have adopted the average FWHM of these two fits to be the width of the [CII] broad component, and its difference to be the 3σ error. The difference can be very large in some cases: F05189-2524 and Mrk 273 are best fitted either with a second narrow Gaussian or with a broad component, while 07251-0248, 13120-5453, F14378-3651 and F22491-1808 can be fitted either with or without a broad component. In the first case, we take the FWHM of the broad component, to be consistent with the rest of our analysis. In the second case, we take the fit with the lowest reduced χ^2 value. The FWHM and error of the broad [CII] components are listed in Table 3.3.

There are some caveats in the analysis. Contamination by H_2O ($158.3\mu\mathrm{m}$) may be present at $1080\,\mathrm{km\,s^{-1}}$. It is not clear whether the bump around $1000\,\mathrm{km\,s^{-1}}$ in F19297-0406 is caused by red-shifted [CII] emission, or by H_2O emission. Two scenarios are fitted: one where the emission around $1000\,\mathrm{km\,s^{-1}}$ is a broad component, and another where this

emission is included in the continuum fit. The average of the two FHWMs is used.

Another complication is that NGC 6240, Mrk 273 and UGC 5101 are not well described by a combination of 2 Gaussians. NGC 6240 is an early stage merger in which the two nuclei are well separated by $1.8''$ in the I and r-band (Fried & Schulz, 1983). Both nuclei are visible in the 3 mm continuum, but the CO(1-0) and CO(2-1) line intensities peak between the two nuclei (Tacconi et al., 1999; Feruglio et al., 2013b). The high spatial resolution maps in CO show that the line emission consists of several components. Also the [CII] line profile requires three components for a good fit. The [CII] line profile of Mrk 273 is irregular with a non-Gaussian shape. Cicone et al. (2014) observe a similar line profile in CO(1-0), and fit the central line with two Gaussians. We also fit two Gaussians to the central line in the [CII] profile, and add a third Gaussian for the broad component. The [CII] line profile in UGC 5101 suggests self-absorption or a 'double horn' profile as is typical for a disk seen edge-on. It could well arise from the molecular disk that is observed in CO(1-0) at velocities similar to the ones in the [CII] line profile (Genzel et al., 1998). The central line profile is well fitted by two Gaussians, and adding a third component slightly improves the overall fit.

3.4.2 Comparison with OH

All fourteen objects with broad [CII] wings either have an OH outflow (11), or inflow (1), with two exceptions: IRAS 23128-5919 clearly has wings in [CII], but the OH119 spectrum is too noisy to be fitted reliably. A faint P-Cygni profile may however be present with an estimated OH $v_{50} \sim -500\,\mathrm{km\,s^{-1}}$. We present the [CII] spectra and fits of this object in Appendix A but exclude it from our analysis. UGC 5101 has a marginally detected broad [CII] component, while OH $v_{50} = -9\,\mathrm{km\,s^{-1}}$. Faint high-velocity wings are however observed in the OH119 spectrum, which are better represented in this case by v_{84} and v_{max}. The object with an OH inflow is IRAS F22491-1808. Hubble Space Telescope observations of IRAS F22491-1808 reveal bright tails, which extend to 16 kpc from the center, and two nuclei separated by 2.5 kpc (Surace et al., 2000). We cannot exclude the possibility that the line profiles reflect tidal effects of a merger rather than an inflow. Inflows are excluded from the sample during the analysis.

A comparison of the OH blue-shifted velocities and broad [CII] FWHM is given in Figure 3.1, which shows the absolute values of the OH119 velocities ($v_{50}, v_{84}, v_{\mathrm{max}}$) as function of the broad [CII] FWHM. The absolute value of the OH velocities is taken, because one can not distinguish an outflow from an inflow by observing only the [CII] wings. The three objects with an OH inflow ($v_{50} > 50\,\mathrm{km\,s^{-1}}$; F15250+3608, F17207-0014 and F22491-1808) are represented by small orange markers. Objects which do not require a broad component for a good fit to the [CII] spectrum are placed at $0\,\mathrm{km\,s^{-1}}$. We moreover added all three objects from Spoon et al. (2013) which have an outflow in both [CII] and OH119. Spoon et al. (2013) give the FWHM of the broad [CII] component and v_{max} of OH119. A blue-shifted and red-shifted component have been fitted to the OH119 spectra of 01003-2238 and 06035-7102, resulting in $v_{50} = -329$ and -171 km s^{-1} respectively. 20100-4156 has a blended and broad absorption component, which we do not attempt to fit, so we have no
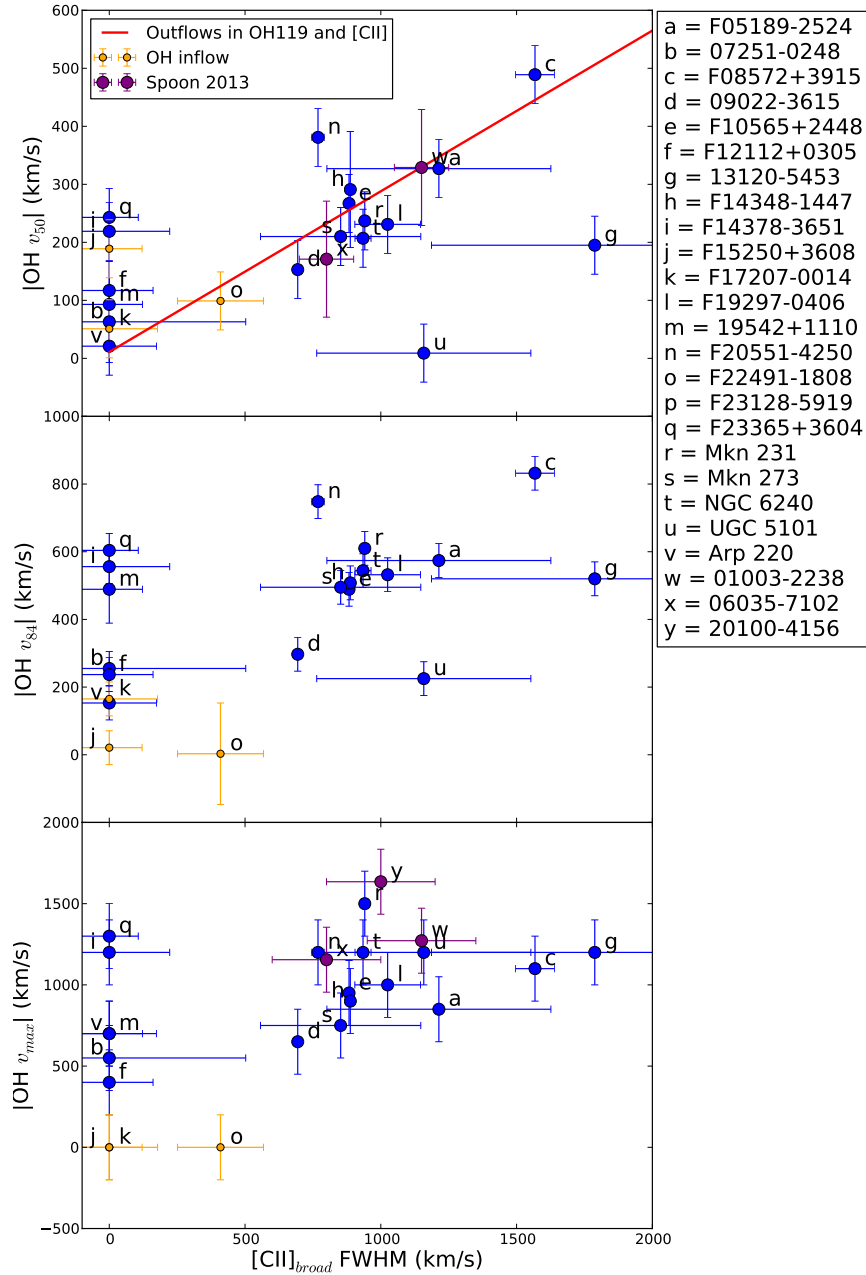
Figure 3.1: [CII] FWHM of the broad component plotted against the absolute value of the several OH velocities. Objects without a [CII] broad component are placed at $0\,\mathrm{km\,s^{-1}}$. The small orange markers represent objects with an inflow in OH119, having a red-shifted absorption ($v_{50} > 50\,\mathrm{km\,s^{-1}}$). Error bars for OH were adopted from V13, [CII] FWHM errors are listed in Table 3.3. Top panel: the red line is a weighted fit to all objects with detected outflows both in OH and C^+.

v_{50} for this object. These objects are represented by purple markers in Figure 3.1, and are taken into account during the line fit (Equation 3.1) and the statistical analysis in Table 3.4.

Sixteen objects in our sample have OH outflows, defined in V13 to be the objects with OH $v_{50} < -50\,\mathrm{km\,s^{-1}}$. Eleven out of these objects also have [CII] broad wings, while five do not. Of these five objects, IRAS 23365+3604 is a real outlier; it has a high-velocity P-Cygni profile in OH but no trace of broad wings in [CII]. Although there is a small bump on the red side of the line, the width of this bump is smaller than the spectral resolution of PACS, and the feature is not considered to be real. IRAS 19542+1110 and IRAS 17208-0014, have low velocity OH outflows. The corresponding expected [CII] FWHM is too small for any outflow to be separable from the emission from the host galaxy. Finally, 07251-0248 and F14378-3651 may well have broad wings in [CII], but the reduced χ^2 value is smaller for the one-component fit.

The objects with a low-velocity OH outflow and no broad [CII] component are consistent with our hypothesis that broad [CII] traces OH outflows, but that a certain minimum velocity is required in order to distinguish emission of the outflow from that of the host galaxy. More qualitatively, out of the eighteen objects which have detected OH119 velocities and no inflow (the blue points in Figure 3.1), fifteen are consistent with this hypothesis. Moreover, it is unlikely that a broad [CII] component traces an inflow: only one of the three objects with an OH inflow has a broad [CII] component, and it has a FWHM of only $409\,\mathrm{km\ s^{-1}}$, which is low compared to the objects with outflows. These findings suggest that a broad [CII] component with a FWHM of $> 500\,\mathrm{km\ s^{-1}}$ is a good indicator for the presence of an OH outflow.

We go one step further by comparing the actual outflow velocities. If C^+ traces an isotropic molecular outflow, a correlation is expected between the broad [CII] FHWM and the blue-shifted velocity of the OH absorption. [CII] seems to correlate with the absolute value of all OH velocities (Figure 3.1), in particular with v_{50}. A weighted least squares fit to $|\mathrm{OH}\ v_{50}|$, for all objects that have an outflow detected both in OH and in C^+, results in:

$$|\mathrm{OH}\ v_{50}| = 11\,(\pm 96) + 0.28\,(\pm 0.10) \times \mathrm{CII_{FWHM}} \qquad (3.1)$$

where all velocities are given in $\mathrm{km\,s^{-1}}$. Each observation is weigthed by $\max[\sigma_\mathrm{OH}, \sigma_\mathrm{[CII]}]^{-2}$, with σ_OH and $\sigma_\mathrm{[CII]}$ the errors in the OH velocity and broad [CII] FWHM respectively. Relation 3.1 is represented by the red line in the upper panel of Figure 3.1. The line goes through (0,0) within the uncertainties, as is expected when C^+ traces the OH outflow.

Is the apparent correlation in the upper panel of Figure 3.1 significant? We call a correlation statistically significant if the null hypothesis (the data points are randomly selected) can be rejected at a confidence level of 5%, using the Spearman rank coefficient and the Pearson correlation coefficient. When all objects with outflows in both OH and C^+ are included, only the Pearson correlation coefficient suggests a correlation. If IRAS 13120-5453 is removed from the sample, the correlation becomes tentative according to the Spearman rank coefficient and significant according to the Pearson correlation coefficient. Table 3.4 lists the correlation coefficients and confidence levels. The confidence levels

Parameter	N	ρ_s	P_ρ	r	P_r	$P_r(N<30)$
(1)	(2)	(3)	(4)	(5)	(6)	(7)
CII_{broad}-$|OHv_{50}|$ (*)	13	0.34	...	0.36	0.23	0.05
CII_{broad}-$|OHv_{84}|$ (*)	11	0.47	0.2	0.39	0.24	...
CII_{broad}-$|OHv_{50}|$ (**)	12	0.55	0.1	0.75	0.01	0.02
CII_{broad}-$|OHv_{84}|$ (**)	10	0.59	0.1	0.65	0.04	0.05
CII_{broad}-α_{AGN}	14	0.4	0.2	0.27	0.35	...
CII_{broad}-L_{AGN}	14	0.06	...	-0.04	0.89	...
$|OHv_{50}|$-α_{AGN}	16	0.45	0.1	0.54	0.03	0.05
$|OHv_{50}|$-L_{AGN}	16	0.29	...	0.29	0.28	...
CII_{broad}-$|Nav_{50}|$	8	0.48	...	0.74	0.04	0.05
OHv_{50}-Nav_{50}	10	0.7	0.05	0.74	0.01	0.02
OH mass-[CII] mass	8	0.61	0.2	0.9	0.01	0.01

Table 3.4: (1) quantities considered for the test, (2) number of objects, (3) Spearman rank coefficient ρ_s, (4) confidence level for rejection of the null-hypothesis (there is no correlation between the two parameters) P_ρ, (5) Pearson correlation coefficient, (6) two-sided area after a Fisher transformation P_r, (7) confidence level for rejection of the null-hypothesis, using the t-value from the Pearson correlation coefficient. Note that P_ρ and $P_r(N<30)$ have been retrieved from a table for low-number statistics, and are applicable to sample sizes of 4-30 data points. If no value is given, the confidence levels are >0.2 and not included in the tables for low-numbers statistics. * including all objects with a detected outflow in both OH and C^+. ** like * but excluding IRAS 13120-5453.

for a two-tailed test have been retrieved from a table for low-number statistics, and are applicable to sample sizes of 4-30 data points (Wall & Jenkins, 2003).

Although part of the lack of a strong correlation between the OH and C^+ velocities can be explained by the small sample, there is also intrinsic scatter in the relation. We assumed that each object has a large opening angle outflow, which is not necessarily the case. Moreover, there are uncertainties in the fits, in particular for objects with faint wings. And finally, C^+ and OH may trace different parts of the outflow. So although C^+ is in general a good tracer of the molecular outflow, significant deviations from the best fit in Equation 3.1 can remain in individual objects.

3.4.3   Correlation with AGN fraction and luminosity

In a previous analysis of 28 local ULIRGs, we found the OH v_{50} to correlate with the AGN fraction α_{AGN} and AGN luminosity, although with significant scatter (V13). Part of the scatter is caused by uncertainty in the AGN luminosity, part again by our assumption of a spherical outflow with a large opening angle, and a constant coupling efficiency. Even in the absence of these uncertainties, an intrinsic scatter is expected due to different driving mechanisms and variable AGN luminosities. Nevertheless, we compare the AGN luminosity and AGN fraction with the broad [CII] FHWM and OH v_{50}, in order to see whether our
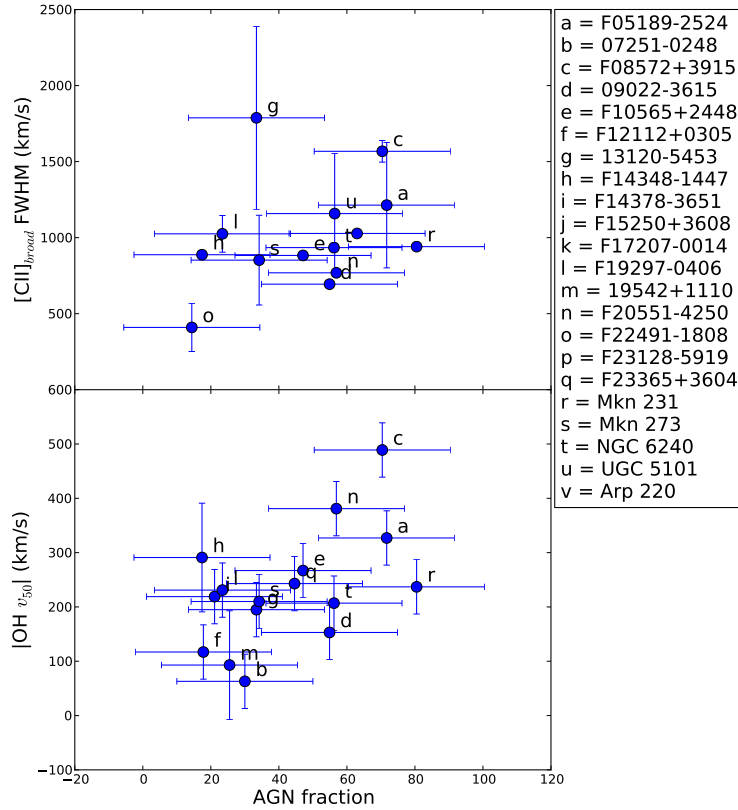
Figure 3.2: Upper panel: broad [CII] FWHM versus AGN fraction as listed in Table 3.1. Lower panel: OH v_{50} versus AGN fraction.

subsample of V13 is large enough to reveal the same correlation as found earlier. Table 3.1 lists the AGN luminosity and fraction for our sources. α_{AGN} has been calculated from f_{30}/f_{15} because these numbers are known for every object in the sample, and because this method shows the tightest relation with other methods to determine the AGN fraction (Veilleux et al., 2009a). The error on the AGN fraction is typically 20%.

Figure 3.2 shows the relation of both the broad [CII] FHWM and OH v_{50} with α_{AGN} for all objects with a detected outflow. There is no statistically significant correlation in any of the two plots, see Table 3.4. Figure 3.3 is similar to Figure 3.2, but now with the logarithm of the AGN luminosity on the x-axis. The uncertainties are taken to be 20% of the total luminosity. Also here, no statistically significant correlation is found with either the broad [CII] FWHM or OH v_{50}. We conclude that the current sample is too small, and covers too small a range in L_{AGN}, to find the same correlation as in V13.
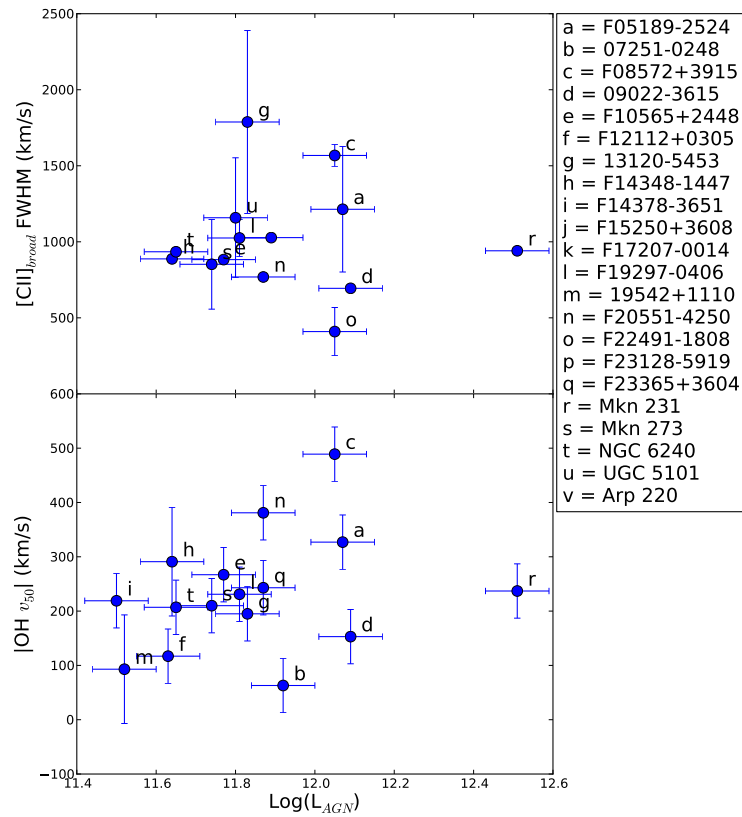
Figure 3.3: Upper panel: [CII] FWHM versus AGN luminosity as listed in Table 3.1. Lower panel: OH v_{50} versus AGN luminosity.
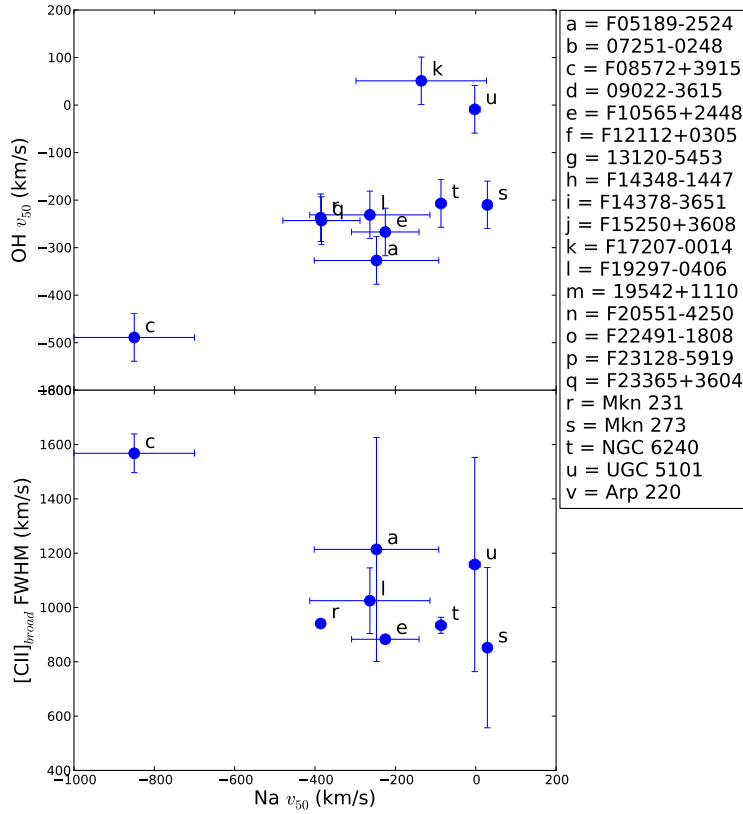
Figure 3.4: Na I D v_{50} compared to OH v_{50} (upper panel) and [CII] FHWM (lower panel). The upper panel shows objects with an OH inflow or outflow (we do not plot the absolute values here, in order to differentiate between inflows and outflows), the lower panel shows only objects with a detected [CII] outflow.

3.4.4 Additional observations: Na I D

Ten objects in our sample have additional observations of blue-shifted Na I D $\lambda\lambda 5890, 5896$ absorption, observed by Rupke et al. (2005b), Rupke et al. (2005a), Rupke & Veilleux (2013a) and Martin (2005). Because Na I D observations are often spatially resolved, several velocities are available for each object. Table 3.2 lists the largest and smallest v_{50} values for the outflowing neutral gas, which were averaged for our analysis here. Figure 3.4 compares Na I D v_{50} to OH v_{50} and the broad [CII] FWHM. F08572+3915 has by far the highest velocity in OH and Na, and the second highest velocity in [CII]. Also for the other objects, Na I D v_{50} shows a trend with with OH v_{50} (for all objects with a detection in both tracers), and with [CII] (for objects with a detection in Na I D and broad wings in [CII]). We give the Spearman rank coefficients and Pearson correlation coefficients in Table 3.4. Despite the small sample, the rejection levels suggest a significant correlation of OH v_{50} with Na v_{50}, which is however driven mostly by F08572+3915.

3.4.5   Additional observations: CO

Seven objects in our sample have CO(1-0) or CO(2-1) observations with sufficient S/N and velocity coverage to reveal broad wings. A comparison with [CII] is facilitated by CO and [CII] both appearing in emission and having similar critical densities. The critical density for the fine structure transition [CII] is $3.2 \times 10^3 \, \text{cm}^{-3}$ (using collision rates with atomic hydrogen at 100 K, Barinovs et al. (2005)). For CO(1-0) and CO(2-1), $n_{\text{crit}} = 2.1 \times 10^3 \, \text{cm}^{-3}$ and $n_{\text{crit}} = 2.2 \times 10^4 \, \text{cm}^{-3}$ respectively (using collision rates with para-H_2 at 100 K, Yang et al. (2010)).

Feruglio et al. (2010) present CO(1-0) observations of Mrk 231. The line profile has been fitted with two components: a narrow one and a broad one with a FWHM of $870 \, \text{km s}^{-1}$ (compared to $971 \, \text{km s}^{-1}$ in [CII]). At higher spatial resolution, the source is slightly resolved at 1.1-1.3 kpc scale (Cicone et al., 2012). NGC 6240 has been observed in CO(1-0) by Feruglio et al. (2013a), who find a line profile extending from $600 \, \text{km s}^{-1}$ to $+800 \, \text{km s}^{-1}$ (compared to $-1000 \, \text{km s}^{-1}$ to $+1500 \, \text{km s}^{-1}$ in [CII]).

Cicone et al. (2014) present CO(1-0) observations of F23365+3604, F10565+2448, Mrk 273 and F08572+3915 from our sample. F23365+3604 – with detected outflows in Na I D and OH but not in [CII] – clearly has broad CO wings, with flux densities of only 1% of the the peak emission. If the outflow is equally faint in the neutral gas traced by C^+, it would explain why no outflow was detected in [CII]: our PACS observations of [CII] do not reach the required sensitivity to detect such a faint component. The CO(1-0) profile for F10565+2448 has very bright wings, which is also the case in our [CII] spectra. F08572+3915 has the fastest CO outflow of the sample, with wings peaking around $-800 \, \text{km s}^{-1}$ and $+900 \, \text{km s}^{-1}$. In our sample, this object also has the highest outflow velocity in OH and Na I D, and the second highest velocity in [CII].

Recently, García-Burillo et al. (2015) published CO(2-1) spectra of IRAS F17207-0014, which revealed a complex line profile. After fitting it with three narrow line components, a residue is left between -700 and $-800 \, \text{km s}^{-1}$. There is however no obvious broad component, again in agreement with our findings from [CII].

The low-J CO and [CII] line profiles show many similarities, and we plan to provide a quantitative comparison in a future paper.

3.4.6   Uncertainties In The Fits And Alternative Velocity Determination

Some spectra in our sample have a [CII] line profile that can be fitted in different ways, resulting in large errors in the FWHM of the broad component. For example, 13120-5453 could either have an extremely broad component, or no broad component at all. The NGC 6240 line profile can be fitted with two or three components, which results in different values for the broad component FWHM. We therefore investigated alternatives. A more objective method is to take the velocities that enclose a certain fraction of the total (host galaxy + outflow) flux (the area-method). We applied this method at both 90% and 95% of the total flux, and found that 90% is a good compromise between being sensitive to

faint emission and being dominated by noise. However, the velocities derived from this method do not correlate at all with the broad [CII] FWHM, the OH velocities, the Na I D velocities or the AGN fraction.

This discrepancy arises because the area-method depends strongly on the emission from the host galaxy, but the luminosity of the host galaxy does not correlate with that of the outflow. An outflow may therefore not be caught when the central component is narrow, or its velocity may be overestimated if the central component is broad. Therefore, separating the host emission from the outflow emission seems necessary, even if this introduces large errors.

Another uncertainty lies in the decision to extract the spectrum from the central or the 3×3 spaxels. If all spectra are extracted from the central spaxel, the correlation between $[CII]_{broad}$ FWHM and the OH velocities weakens a bit. Most importantly, the $[CII]_{broad}$ FWHM of F08572+3915 decreases from $1586\,km\,s^{-1}$ to $898\,km\,s^{-1}$, which weakens the correlation between $[CII]_{broad}$ FWHM and Na I D v_{50}. Otherwise, the results remain the same.

3.5 Discussion

Studying a similar sample of 24 ULIRGs in OH119 and [CII], Spoon et al. (2013) and Farrah et al. (2013) only found four objects with broad wings in [CII]. In three objects the [CII] line width matches well with the line width of the blue-shifted OH absorption. The reason for finding only few [CII] broad components probably is, as the authors note themselves, that the observations do not have the required sensitivity to detect faint wings. The ULIRGs in their sample are fainter and at higher redshift ($z < 0.262$) than in our sample ($z < 0.1$).

3.5.1 Outflow Mass

The OH absorption only traces the molecular outflow along our line of sight to the FIR continuum. Calculation of the total outflow mass thus requires an assumption on the opening angle and geometry of the outflow. Moreover, the absorbed flux depends on the OH column density toward the source, on the covering factor of OH onto the FIR continuum, and on the FIR continuum intensity and spectral shape. A single OH transition is therefore not sufficient for mass determinations. We did however detect three or more OH transitions in some sources, and calculated the outflow mass for the nine sources which (1) have detections of at least three out of the four transitions: OH119, OH79 ($^2\Pi_{1/2}\,1/2 \rightarrow {}^2\Pi_{3/2}\,3/2$), OH84 ($^2\Pi_{3/2}\,7/2 \rightarrow 5/2$) and OH65 ($^2\Pi_{3/2}\,9/2 \rightarrow 7/2$), (2) with clear P-Cygni profiles or broad wings, and (3) for which the spectra and fits look normal.

The model is described in González-Alfonso et al. (2014), and final results will be published in González-Alfonso (2016, submitted). A short description of the model is given here. Each object is described by the sum of three components: two outflow components

(with different velocity, spatial extents and far-IR radiation sources) and one quiescent component. Free parameters of the model are: the inner- and outer- radius of the component, the dust temperature, the continuum optical depth at $100\,\mu$m, the gas velocity at R_{in}, the gas velocity at R_{out}, the OH column density, the impact parameter (giving the on-sky spatial extend of the outflow) and the scaling factor (related to the covering factor of OH with respect to FIR continuum). Each component is divided in at least 20 concentric shells. The statistical-equilibrium populations are calculated in each shell, and the emerging line shapes are calculated and convolved with the PACS spectral resolution. These modeled line profiles are then compared to the three or more available spectra in OH, and the best fit is used. The mass is derived from the outflow components only. Figure 3.5 compares these outflow masses based on OH absorption with those based on [CII] emission.

The mass of the neutral atomic outflow was derived from the [CII] broad component using the cooling law as described in the Appendix of Tielens & Hollenbach (1985), and assuming that [CII] is optically thin:

$$n^2\Lambda = \frac{g_u/g_l \exp[-h\nu_{ul}/kT]}{1 + n_{cr}/n + g_u/g_l \exp[-h\nu_{ul}/kT]}\, \chi_{C^+} n A_{ul} h\nu_{ul} \tag{3.2}$$

This equation describes the cooling of the ISM per unit volume due to line emission ($[n^2\Lambda] = \mathrm{J\,s^{-1}\,cm^{-3}}$). The ratio of the statistical weights of the upper and lower level $g_u/g_l = 2$, $h\nu_{ul}/k = 91$ K, the critical density $n_{cr} = 3.2 \times 10^3\,\mathrm{cm^{-3}}$ in neutral medium (Barinovs et al., 2005), the abundance $\chi_{C^+} = 1.4 \times 10^{-4}$, the Einstein coefficient for spontaneous emission $A_{ul} = 2.4 \times 10^{-6}\,\mathrm{s^{-1}}$, and the frequency $\nu_{ul} = 1.9 \times 10^{12}\,\mathrm{Hz}$. Filling in these constants results in the following equation:

$$\frac{M_N}{M_\odot} = 1.34 \frac{L_{\mathrm{CII}}}{L_\odot} \times \frac{1 + n_{cr}/n + 2\exp[-91\mathrm{K}/T]}{2\exp[-91\mathrm{K}/T]} \tag{3.3}$$

where we assumed that 25% of the mass is in helium, and that all broad [CII] emission arises from atomic gas.

In order to derive the density and temperature we need either a CO line SED or FIR SED plus density tracers, but these observations are not available for the outflows. Instead, we will use $n = 10^5\,\mathrm{cm^{-3}}$ and $T = 100\,\mathrm{K}$, which should be typical conditions in ULIRGs (Sanders & Mirabel, 1996; Veilleux et al., 2009a; Mashian et al., 2015). The fraction in Equation 3.3 becomes 2.28. This number is quite conservative, as it is less than twice as large as the factor retrieved for infinitely large density and temperature (1.5). With an uncertainty of 50% due to unknown temperature and density and a 30% flux calibration error, we adopt a total error of 80%. Table 3.3 lists the luminosities of the broad components and the derived total neutral gas masses. These masses are probably too high for NGC 6240, F14348-1447 and 09022-3615 ($M > 10^9 M_\odot$), because the outflow emission could not be separated well from the host galaxy emission.

There appears to be a tentative 1:1 relation between the derived outflow masses from OH and [CII], albeit within the large uncertainties (Figure 3.5). Together with the observed trend between the broad [CII] FWHM and OH $v50$, this supports our hypothesis that a
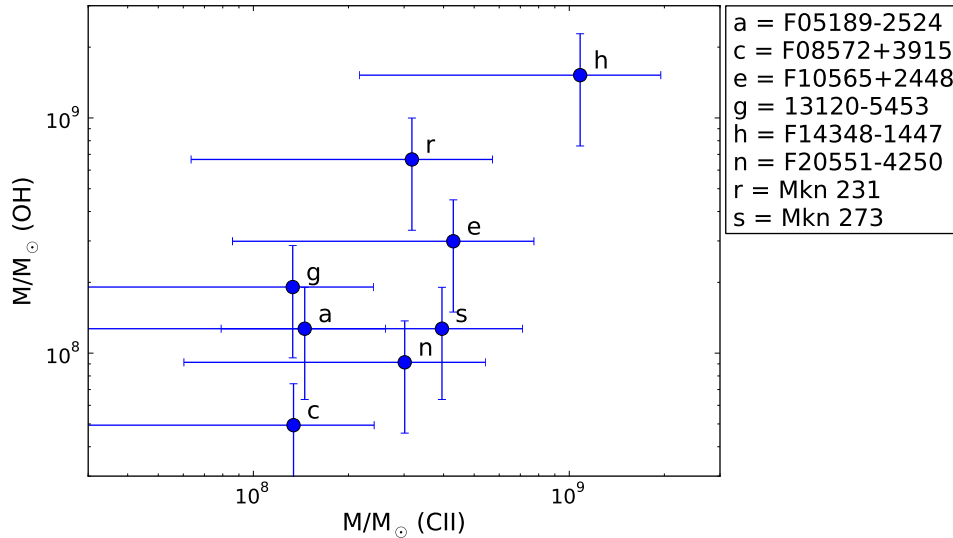
Figure 3.5: Total molecular outflow mass based on OH line modeling by González-Alfonso (2016, submitted) on the y-axis, and atomic outflow mass based on the luminosity of the [CII] broad component on the x-axis.

broad [CII] component is a plausible tracer of molecular outflows in galaxies. The mass has been calculated from OH by adopting an abundance of 2.5×10^{-6} relative to H nuclei and including a factor of 1.4 due to Helium. Both derivations should therefore result in similar masses if the same amount of particles is involved. An exact 1:1 relation is not necessarily expected. OH absorption arises predominantly from the molecular gas while C^+ emission arises from atomic and molecular gas. Some overlap between the two tracers is expected, but it is not known how much. Yet, within these uncertainties, the mass derived from the luminosity of the broad [CII] component seems to agree well with the outflow mass derived from OH. The relation is significant according to the Pearson correlation coefficient, but not if the Spearman rank coefficient is used (Table 3.4). However, we stress here that the OH masses are preliminary results, and that the correlation is driven by the large mass in IRAS F14348-1447 ($1\text{-}2 \times 10^9 \, M_\odot$).

3.5.2   Origin of the [CII] broad wings

The P-Cygni profiles and blue-shifted absorptions in OH are clear signs of outflowing gas. Broad wings in [CII] on the other hand, can be caused by outflows, inflows, turbulence, or a high velocity rotation disk. However, the OH spectra have shown that the ULIRGs in our sample contain molecular outflows more often than inflows (16 outflows versus 3 inflows). Furthermore, all outflow masses derived from OH and [CII] lie along a 1:1 relation within the uncertainties. Adding to that the trend of the broad [CII] FWHM with OH v_{50}, leads us to the conclusion that [CII] traces and is likely entrained in the OH outflow.

This does not mean that [CII] broad wings exclusively trace molecular outflows: the broad [CII] FWHM also shows a trend with Na I D blue-shifted velocity (Figure 3.4, Table 3.4), suggesting an origin in atomic gas. V13 already found a correlation between Na I D v_{50} and OH v_{50}, showing that the atomic and molecular outflow are mixed or that OH absorption arises mostly from the atomic gas.

Multi-phase outflows have been observed before, although the connection between the different phases is not always clear (Shih & Rupke, 2010; Westmoquette et al., 2013; Kreckel et al., 2014; Morganti et al., 2015). Gas phases with similar outflow velocities can be explained by gas mixing. For example, Contursi et al. (2013) explain the similar velocities of [OIII] $\lambda 88\mu$m, [OI] $\lambda 63\,\mu$m and $\lambda 145\,\mu$m, [CII], and CO(1-0) in M82, by assuming that the outflow consists of small molecular cloudlets which are ionized on the outside, but remain molecular inside. In this way, the different phases do not only have the same velocity, but are also cospatial. Spatially resolved observations of the outflows would therefore help to explain the connection between the gas phases.

Rupke & Veilleux (2013b) present spatially resolved IFU observations of Na I D and H α of the following ULIRGs in our sample: F08572+3915, F10565+2448, Mrk 231, Mrk 273 and F17207-0014 (F17207-0014 only has Na I D detected). All of them have extended outflows with a radius $\geq 1\,$kpc. These kpc-scales may be hard to unite with the scale of the OH absorption. PACS did not resolve the OH absorption, but there are several indications that the absorption arises from scales ≤ 1 kpc:

- Using the model as described in Section 3.5.1, Sturm et al. (2011a) find inner radii of 100-200 pc for the OH outflow for five objects in our sample, and outer radii of a few hundred pc.

- Spoon et al. (2013) use the anti-correlation between OH119 equivalent width and the silicate strength to argue that the OH119 absorption arises in the buried nucleus.

- Rupke & Veilleux (2013a) present spatially resolved observations of the H$_2$ outflow in F08572+3915 (NW) at 400 pc. The outflow velocities correspond well with those observed in OH.

There is however a bias in the determination of the spatial scale at which OH absorption takes place, because a bright FIR continuum is needed. If this continuum has a smaller spatial extent than the OH outflow, a significant part of the OH outflow will not be illuminated. Lutz et al. (2015) recently published the Herschel/PACS FIR radii at 70 μm for our objects, and provided us with the radii at 100 μm (private communication). These radii range from below 0.5 kpc to 2.8 kpc, and are typically around 1 kpc for our sample. The OH outflow could therefore be more extended than what we infer from the PACS observations.

If the outflow is located at a kpc from the nucleus, would it be able to escape the gravitational potential of the galaxy? Based on the widths of the narrow components of the [CII] line profile (deconvolved with the spectral PACS PSF), we estimate the dynamical mass from $M_{dyn} = K\sigma^2 R/G$ assuming $R = 1$ kpc and K a factor that depends on the

galaxy's geometry. For $K = 3$, the typical dynamical mass in our sample is $10^{10} M_\odot$. For a central mass of $10^{10} M_\odot$, the escape velocity is $\sim 300\,\mathrm{km\,s^{-1}}$, which is reached by most C^+ outflows. Part of the gas could therefore escape the central kiloparsec of the galaxy, although it may not escape the halo.

3.6   Summary and conclusion

We address the question of whether [CII] at $158\,\mu\mathrm{m}$ is a good tracer of outflows in general, and molecular outflows in particular. The sample consists of 22 local and bright ULIRGs, of which 16 objects have molecular outflows as traced by OH $119\,\mu\mathrm{m}$ absorption at velocities $< -50\,\mathrm{km\,s^{-1}}$. Because [CII] appears in emission, any isotropic and spatially unresolved outflow becomes visible as broad wings in the line profile. We fitted the [CII] line profiles with two Gaussians, in order to separate host emission from outflow emission, and use the FWHM of the broad component to estimate the outflow velocity. The main results are:

1. Fourteen objects in our sample show broad [CII] wings. Eleven of these objects contain an OH outflow, one contains an inflow, one object has a noisy OH spectrum and is removed from the analysis, and one has a faint outflow which is not traced by OH v_{50} (the median velocity of the blue-shifted absorption). If all objects with an outflow in [CII] and OH119 are taken into account, the FWHM of the broad [CII] component shows a tentative correlation with OH v_{50} and v_{84}.

2. Observations of Na I D are available for 10 sources in the sample. The FWHM of the broad [CII] component shows a trend with the Na I D v_{50}. This is not surprising, since Na I D v_{50} was already found to correlate with the OH v_{50} in V13. [CII] may thus trace both the molecular and atomic gas in the neutral outflow, and part of the OH absorption could arise from the atomic gas as well.

3. The broad [CII] FWHM does not show a correlation with either the AGN luminosity or the AGN fraction. This might be caused by a combination of large uncertainties in the AGN luminosity and fraction, intrinsic scatter, and the small sample: no correlation is found between OH v_{50} and AGN fraction or luminosity either, although such a correlation was found when using a larger sample.

4. Preliminary estimates of the molecular outflow mass, based on at least three OH line profiles, are given for nine objects. These masses lie roughly on a 1:1 relation with the outflow mass derived from the broad [CII] component, and can be up to $10^9 M_\odot$. This shows that both OH and C^+ trace the same (or similar fractions of the) massive outflows observed in ULIRGs.

5. We conclude that the broad [CII] wings are a good tracer of both the molecular and atomic phases of the outflow, and that the outflow mass based on [CII] is a good estimate of the molecular outflow mass.

3.7   Appendix A: Gaussian fits

Figure 3.6 shows the [CII] spectra for each source in our sample. Each subfigure lists the FHWM of the broad component and the reduced χ^2 value for the fit. The fit has been done to the normal (linearly scaled) flux density, but here the y-axis is shown in a logarithmic scale, to increase the visibility of the low signal wings. The residual plot below each figure is shown in linear scale. Shaded areas mark the range that was chosen for the continuum fit. The [CII] spectra for each source in our sample are plotted twice, in order estimate the error on the FWHM of the broad component. In the first subfigure, the continuum was fitted close to the line, at good signal to noise, but potentially removing broad lines and minimizing the FWHM of the broad component. In the second figure, the continuum was fitted far away from the line, at the edges where the signal to noise ratio was low, but leaving plenty of room for a broad component. Because the spectra are only fully covered from $-1300\,\mathrm{km\ s^{-1}}$ to $+1300\,\mathrm{km\ s^{-1}}$, and the part outside this region has been scanned less frequently, the noise steadily increases at velocities $< -1300\,\mathrm{km\ s^{-1}}$ and $> 1300\,\mathrm{km\ s^{-1}}$. We therefore avoid fitting the continuum in high-velocity regions with sudden peaks and dips in the spectrum. After continuum subtraction, we attempted to fit two Gaussians (and in exceptional cases three Gaussians) to the line profile. Table 3.5 contains all the parameters of the Gaussian fits.
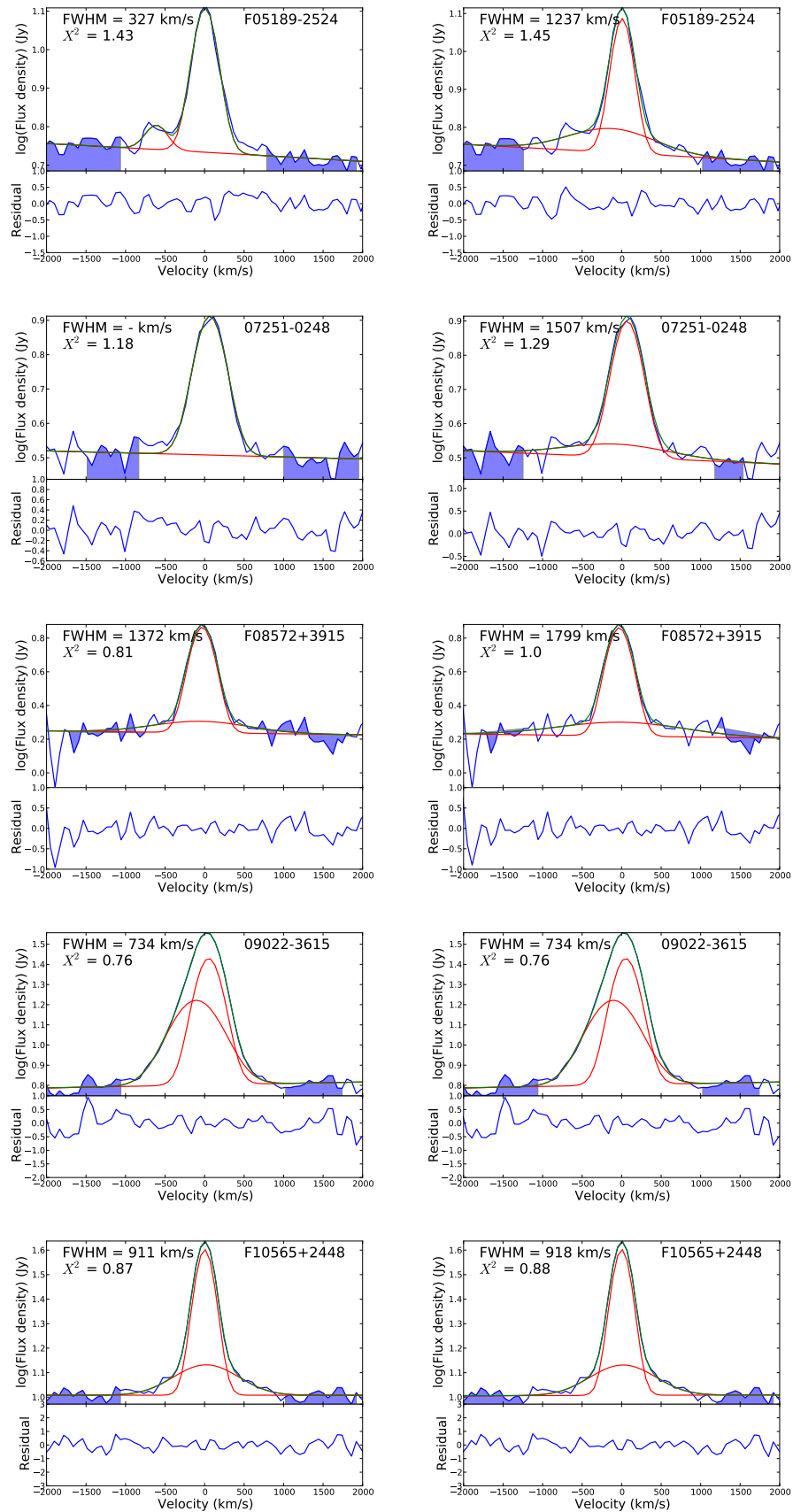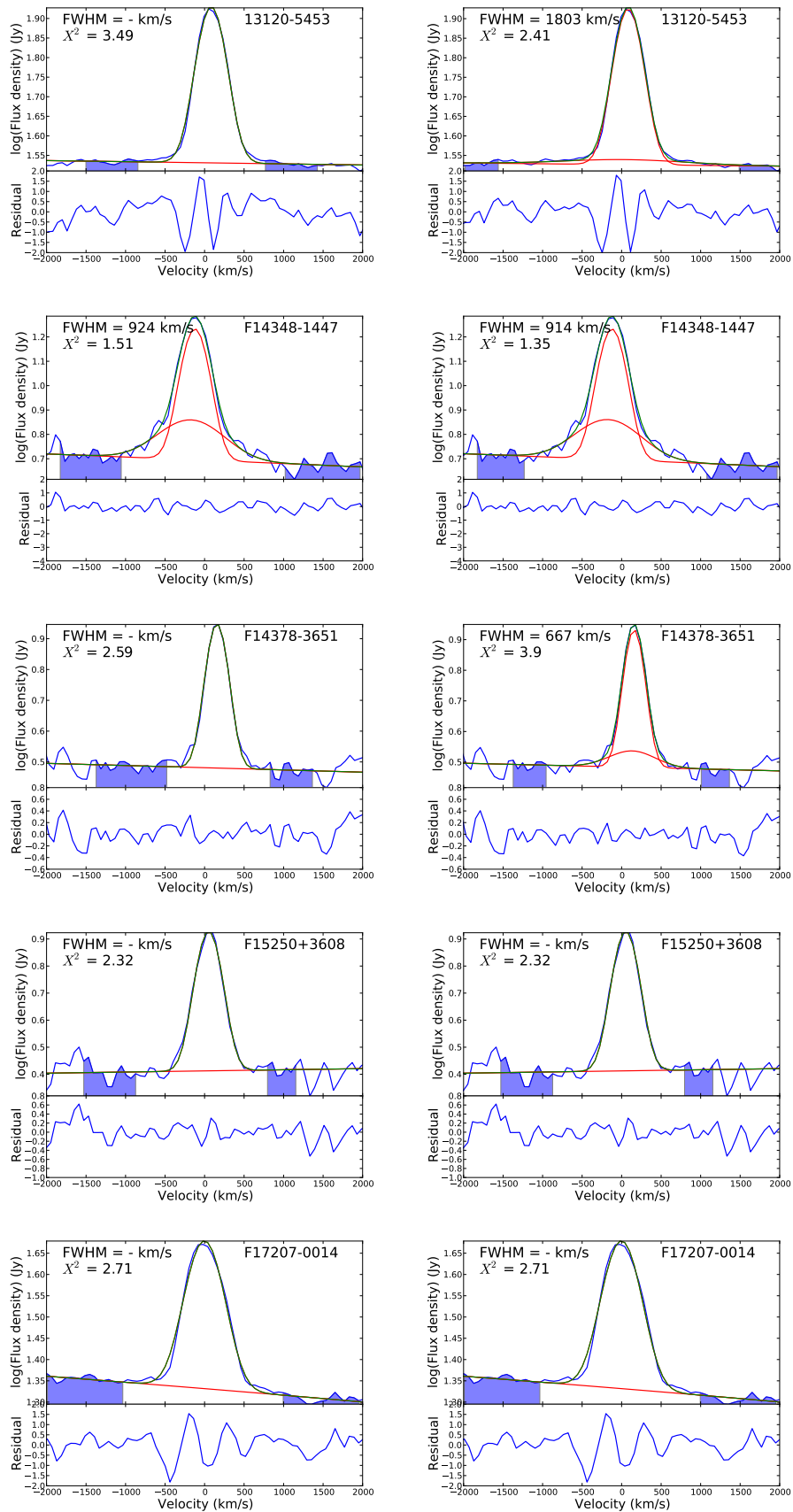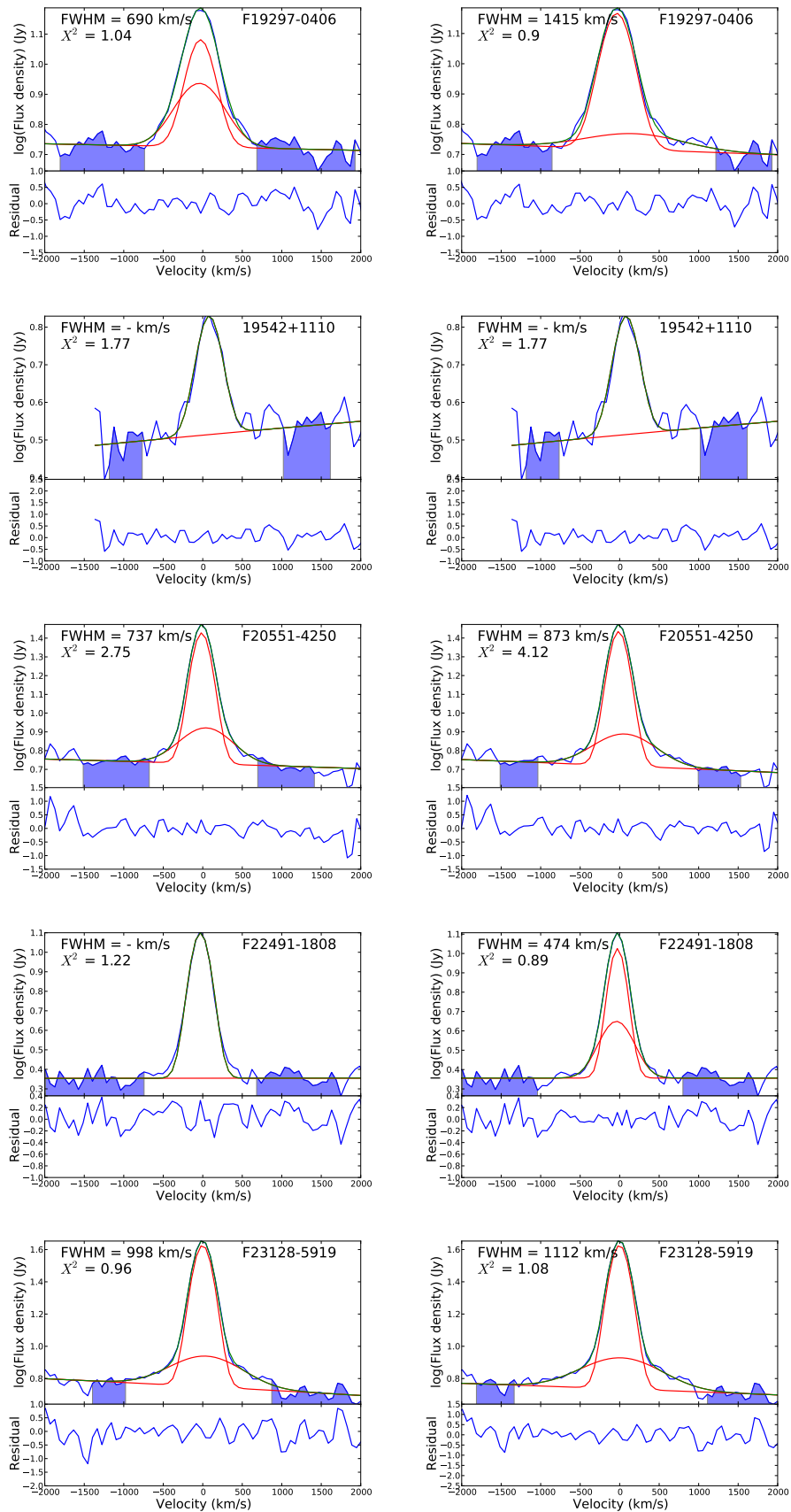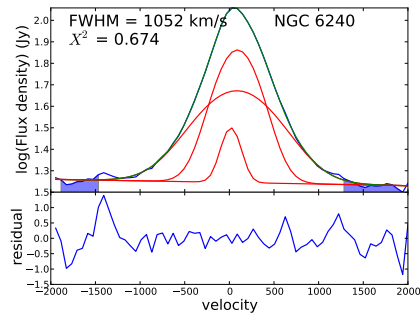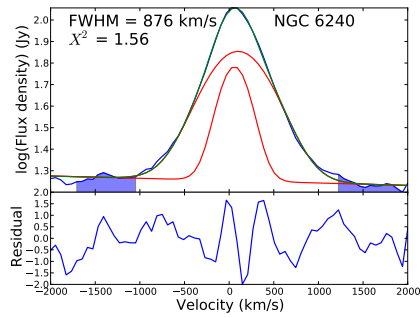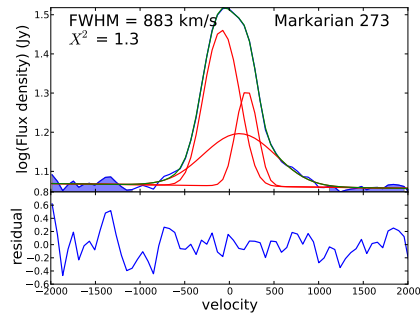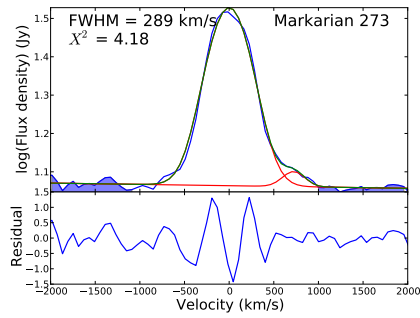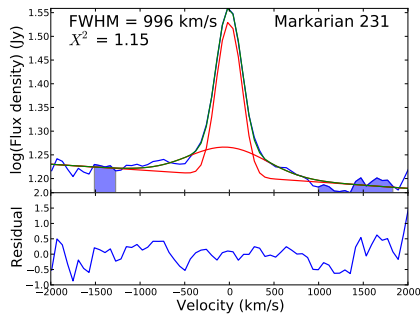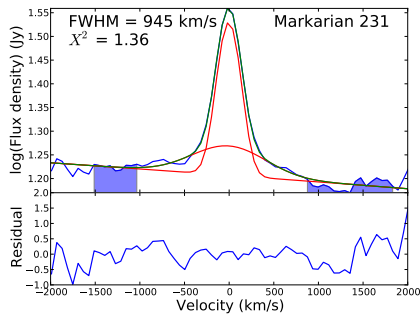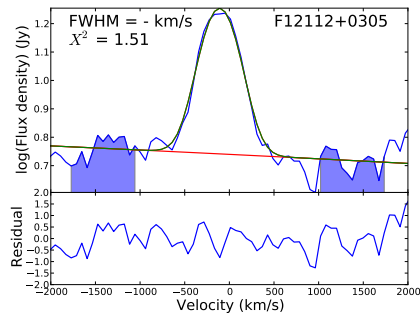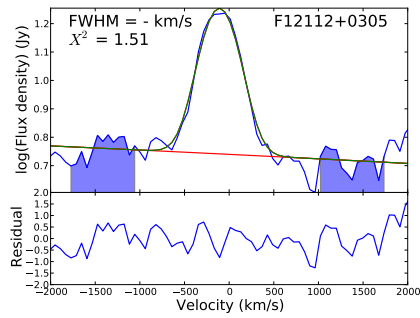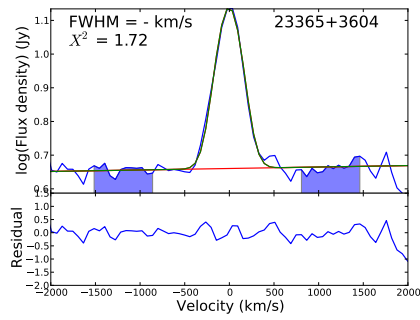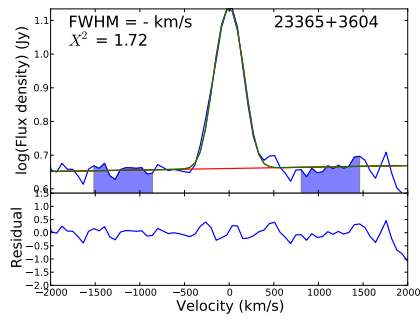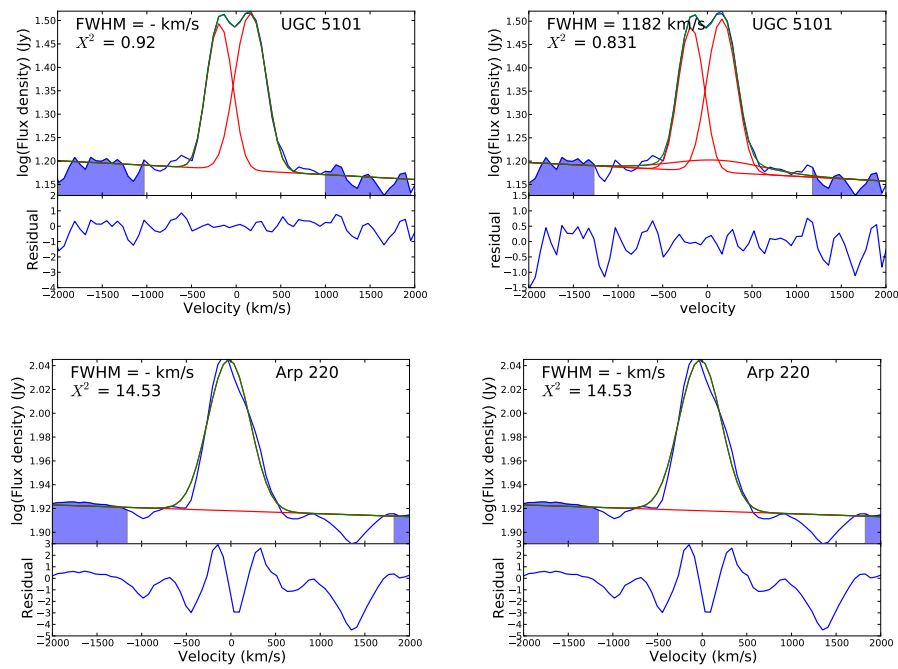
Figure 3.6: Gaussian fits to [CII] spectra: the flux density in the upper panel is shown in logarithmic scale, to make the faint wings stand out. The residual in the lower panel is given in linear scale. The FWHM of the broad component and the reduced χ^2 value is given in the figure. The PACS spectral resolution is 240 km s^{-1} FWHM. Each source has been fitted twice with different placements of the continuum, as shown by the shaded area.

Name	h_1	m_1	FWHM$_1$	h_2	m_2	FWHM$_2$	h_3	m_3	FHWM$_3$	χ^2
F05189-2524	7.43	6	363	0.86	-609	327	...	...	...	1.43
F05189-2524	6.82	7	319	0.84	-131	1237	...	...	...	1.45
07251-0248	4.95	66	449	...	...	...	...	...	...	1.18
07251-0248	4.76	69	426	0.29	-78	1507	...	...	...	1.29
F08572+3915	5.6	-31	351	0.29	-52	1372	...	...	...	0.81
F08572+3915	5.62	-31	352	0.34	-9	1799	...	...	...	1.0
09022-3615	20.58	51	410	10.35	-106	734	...	...	...	0.76
F10565+2448	29.89	0	301	3.37	20	911	...	...	...	0.87
F10565+2448	29.91	0	301	3.36	16	918	...	...	...	0.88
13120-5453	51.24	84	414	...	...	...	...	...	...	3.49
13120-5453	50.72	84	408	1.01	45	1803	...	...	...	2.41
F14348-1447	12.15	-122	383	2.27	-174	924	...	...	...	1.51
F14348-1447	12.13	-122	383	2.28	-174	914	...	...	...	1.35
F14378-3651	5.87	156	308	...	...	...	...	...	...	2.59
F14378-3651	5.53	157	286	0.4	132	667	...	...	...	3.9
F15250+3608	5.9	51	362	...	...	...	...	...	...	2.32
F17207-0014	26.32	-1	533	...	...	...	...	...	...	2.71
F19297-0406	6.76	-28	413	3.33	-40	690	...	...	...	1.04
F19297-0406	9.46	-35	472	0.67	178	1415	...	...	...	0.9
19542+1110	3.5	81	366	...	...	...	...	...	...	1.77
F20551-4250	21.44	-14	302	2.98	41	737	...	...	...	2.75
F20551-4250	22.0	-13	307	2.52	59	873	...	...	...	4.12
F22491-1808	10.33	-30	300	...	...	...	...	...	...	1.22
F22491-1808	8.34	-28	259	2.19	-40	474	...	...	...	0.89
F23128-5919	36.73	-1	307	3.08	38	998	...	...	...	0.96
F23128-5919	36.92	-1	308	3.04	14	1112	...	...	...	1.08
F23365+3604	9.18	-2	320	...	...	...	...	...	...	1.72
F12112+0305	12.46	-108	483	...	...	...	...	...	...	1.51
Mrk 231	17.79	-3	291	2.47	-8	945	...	...	...	1.36
Mrk 231	17.9	-3	292	2.4	-20	996	...	...	...	1.15
Mrk 273	22.19	0	561	1.09	722	289	...	...	...	4.18
Mrk 273	17.33	-85	394	8.74	194	258	4.17	114	885	1.3
NGC 6240	42.82	59	415	53.63	100	876	...	...	...	1.56
NGC 6240	14.04	17	248	55.25	90	570	29.45	86	1053	0.67
UGC 5101	15.91	-186	298	17.65	160	357	...	...	...	0.92
UGC 5101	15.69	-181	295	16.96	161	340	0.91	118	1182	0.83
Arp 220	28.15	-22	521	...	...	...	...	...	...	14.53

Table 3.5: Parameters of Gaussian fits to the [CII] spectra. The units are Jansky for the height and km s^{-1} for the mean and FWHM. $\chi^2 = \frac{1}{N-n-1}\Sigma_{i=1}^{N}(obs_i - fit_i)^2/\sigma^2$, with N the number of data points in the spectrum, n the number of free parameters during the fit, and σ the RMS in the continuum. Each source has been fitted twice with different placements of the continuum, and appears therefore twice in the table.

Chapter 4

Spatially resolving the molecular outflow in IRAS F08572+3915

This chapter presents results that have not yet been published.

4.1 Introduction

Chapter 3 has shown that most local ULIRGs host molecular outflows, as traced by both blue-shifted absorption of OH 119 and broad wings in [CII]. However, the PACS observations do not spatially resolve the outflows: the spatial point spread function of the spectrometer is $\sim 12''$ at $158\,\mu$m (rest wavelength of [CII]) and $\sim 9.5''$ at $119\,\mu$m (rest wavelength of OH), which corresponds to about 10 kpc in our objects. In order to derive reliable values for the mass outflow rate, it is essential to know where the outflow is located with respect to the galaxy's center. Moreover, spatially resolved observations of the molecular outflow would reveal whether our assumption of a spherically symmetric outflow is reasonable, and may give insights on the outflow driving mechanism. Unfortunately these observations are not possible in the far-infrared, because it requires a space telescope with a large mirror or several mirrors (of the order of 35 meter diameter or separation, in order to get $1''$ spatial resolution). Therefore, the CO(1-0) transition is often used, which can well be observed from the ground with sensitive interferometers like ALMA and NOEMA, and also reveals outflows through broad wings in the line profile. This way, outflows have been detected for some objects in our sample, as discussed in Chapter 3.

In this chapter, deep and high spatial resolution CO(1-0) observations of IRAS F08572+3915 are presented. IRAS F08572+3915 is an interacting system, with the main galaxy located in the north west (NW) and the secondary galaxy in the south east (SE), as is clear from the I-band and B-band Hubble Space Telescope images (Surace et al. (1998) ; see also Figure 4.1). The left panel of Figure 4.1 shows the logarithm of the intensity in the interacting galaxy at 435 nm, taken from the Hubble Legacy Archive. The peak of CO(1-0) emission is marked with a cross, and the two windows mark the regions from which the CO(1-0) spectra were extracted. The NW galaxy hosts the fastest (unambiguous)

Name	Date	Configuration (# Antennas)	Time on-source	P.I.
v026	May-Oct 2011	C+D (5 or 6)	20 hr	Sturm
w088	Feb-March 2013	A (6)	10 hr	Sturm
w14ch	March 2015 - Feb. 2016	A+B (6 or 7)	20 hr	Janssen

Table 4.1: Details of the NOEMA observations.

molecular outflow from our sample (Section 3.2), as well as fast neutral outflows (as traced by blue-shifted Na I D absorption; Section 3.4.4) and ionized outflows (as traced by broad Hα wings, Rupke & Veilleux (2013b)). These outflows are thought to be AGN-driven, as discussed in Section 4.4.1.

Previous compact configuration NOEMA observations of CO(1-0) clearly revealed the molecular outflow with velocities of $\sim 1000\,\mathrm{km\,s^{-1}}$, a mass of $10^{8.61}\,M_{\odot}$ (for a conversion factor $\alpha_{\mathrm{CO}} = 0.8\,M_{\odot}\,(\mathrm{K\,km\,s^{-1}\,pc^2})^{-1}$) and outflow rate $1210\,M_{\odot}$/year (Cicone et al., 2014). We now expand this dataset with extended configuration observations, which improve the sensitivity and spatial resolution. As a result, we find that the most probable geometry of the outflow is a biconical shape, aligned with the kinematic major axis of the rotation disk. Moreover, the red-shifted part of the outflow is resolved in two components, where the second component is located at ~ 6 kpc from the NW galaxy and has a velocity decreasing with distance to the galaxy's center. The blueshifted part of the CO outflow is found to overlap spatially with blueshifted outflows in Hα, H$_2$ and Na I D. And finally, the second galaxy is detected in CO(1-0) for the first time.

These new results will be used to constrain the source of the outflows; are they driven by the AGN, by star formation, or are they tidally induced streams? Also the geometry and the revised outflow mass, mass rate, momentum rate and energy rate can be compared to theoretical models of (AGN-) driven feedback.

We adopt a cosmology with $H_0 = 70\,\mathrm{km\,s^{-1}\,Mpc^{-1}}$ and $\Omega_M = 0.3$, which results in a luminosity distance $D_L = 262$ Mpc and a scale of $1.21\,$kpc/arc second for a source at $z = 0.0582$. The bolometric luminosity is assumed to be $1.15 L_{8-1000\mu m}$ (Sanders & Mirabel, 1996), resulting in $L_{bol} = 10^{12.2} L_{\odot}$ (Veilleux et al., 2013). All maps are given with the North at the top and the East on the left.

4.2   Data reduction

In total, there have been three NOEMA (formerly Plateau de Bure Interferometer) observing programmes that target the CO(1-0) outflow in IRAS F08572+3915. Table 4.1 lists observing dates, configuration, number of antennas and on-source time for these programmes. The WideX observations have a band width of 3.6 GHz (corresponding to 9884 km s^{-1} at the observed frequency of 108.93 GHz) and a resolution of 1.95 MHz (corresponding to 5.35 km s^{-1}).

The data were calibrated in CLIC[1] with help from the staff in Grenoble. After calibra-

---

[1]CLIC is part of the GILDAS package: http://www.iram.fr/IRAMFR/GILDAS

tion, separate uv tables were created for the configuration C+D, A+B, and A+B+C+D observations. We then used the MAPPING[2] software for cleaning and imaging. The synthesized beam size is $2.95'' \times 2.56''$ with a Position Angle of $61°$ for the C+D configuration, $1.08'' \times 0.82''$ with a P.A. of $34°$ for the A+B configuration, and $1.4'' \times 1.13''$ with a P.A. of $43°$ for the A+B+C+D configuration. Configuration A+B+C+D observations will be used for further analysis, because of the highest sensitivity.

The data were binned in 40 km s^{-1}, which balances a good signal-to-noise ratio and spectral resolution. The continuum is taken to be the average over the velocity range $-3500\,\mathrm{km\,s^{-1}}$ to $-2000\,\mathrm{km\,s^{-1}}$, and $2000\,\mathrm{km\,s^{-1}}$ to $4000\,\mathrm{km\,s^{-1}}$. It was detected at 1.5 mJy, and has been subtracted from the spectra before any analysis on them was done.

4.3 Analysis and Results

The right panel of Figure 4.1 shows the log of the CO(1-0) emission, with the two regions from which spectra are extracted: a $4'' \times 4''$ region centered at R.A. 9:00:25.6, Dec. +39:03:50 (corresponding to (2.8 ,-4.2) in the map) for the secondary galaxy, and a $4.5'' \times 8.0''$ region, stretched towards the North in order to capture the redshifted emission, centered at R.A. 09:00:25.35 Dec. 39:03:56.3 (corresponding to (-0.3,2.1) in the map). Note that these windows do not capture any faint emission around $\Delta\mathrm{R.A.} = -1'', \Delta\mathrm{Dec.} = -3''$, which coincides with a tail connecting the two galaxies. This region is not included in any of the spectra, because it is not clear to which galaxy this emission belongs, and because it could be contaminated by residual sidelobe emission from the main galaxy.

Figure 4.2 shows the spectra extracted from the two areas described above. Broad wings are clearly visible in the spectrum of the NW galaxy, as shown in the left panel. The SE galaxy is much fainter in CO(1-0), and has now been detected for the first time. Its line profile is narrow and has a central velocity similar to that of the NW galaxy; a Gaussian fit to the spectrum peaks at 30 km s^{-1}.

Extended emission might be missed when the telescope is used in extended (A+B) configuration. But because all analysis is done on the A+B+C+D observations, our fluxes are the same as those presented in Cicone et al. (2014). There is one exception though: Cicone et al. (2014) note that there may be extended emission in the blue component, that may not be caught even in the compact configuration, based on an extrapolation of the uv radius versus amplitude plot towards a uv radius = 0 m. Here we will use the detected flux, rather than the extrapolated one (1.3 instead of 1.7 Jy km s^{-1}). Table 4.2 lists the fluxes, noise levels, coordinates, and masses of the galaxies and the outflows.

We use the following to retrieve the CO total line flux in K km s^{-1} pc^2 from the flux in Jy km s^{-1}:

$$L'_{CO} = 3.25 \times 10^7 S_{CO}\Delta v \nu_{obs}^{-2} D_L^2 (1+z)^{-3} \tag{4.1}$$

with $S_{CO}\Delta v$ the flux in Jy km s^{-1}, ν_{obs} the observed frequency in GHz, D_L the luminosity distance in Mpc and z the redshift (Solomon & Vanden Bout, 2005).

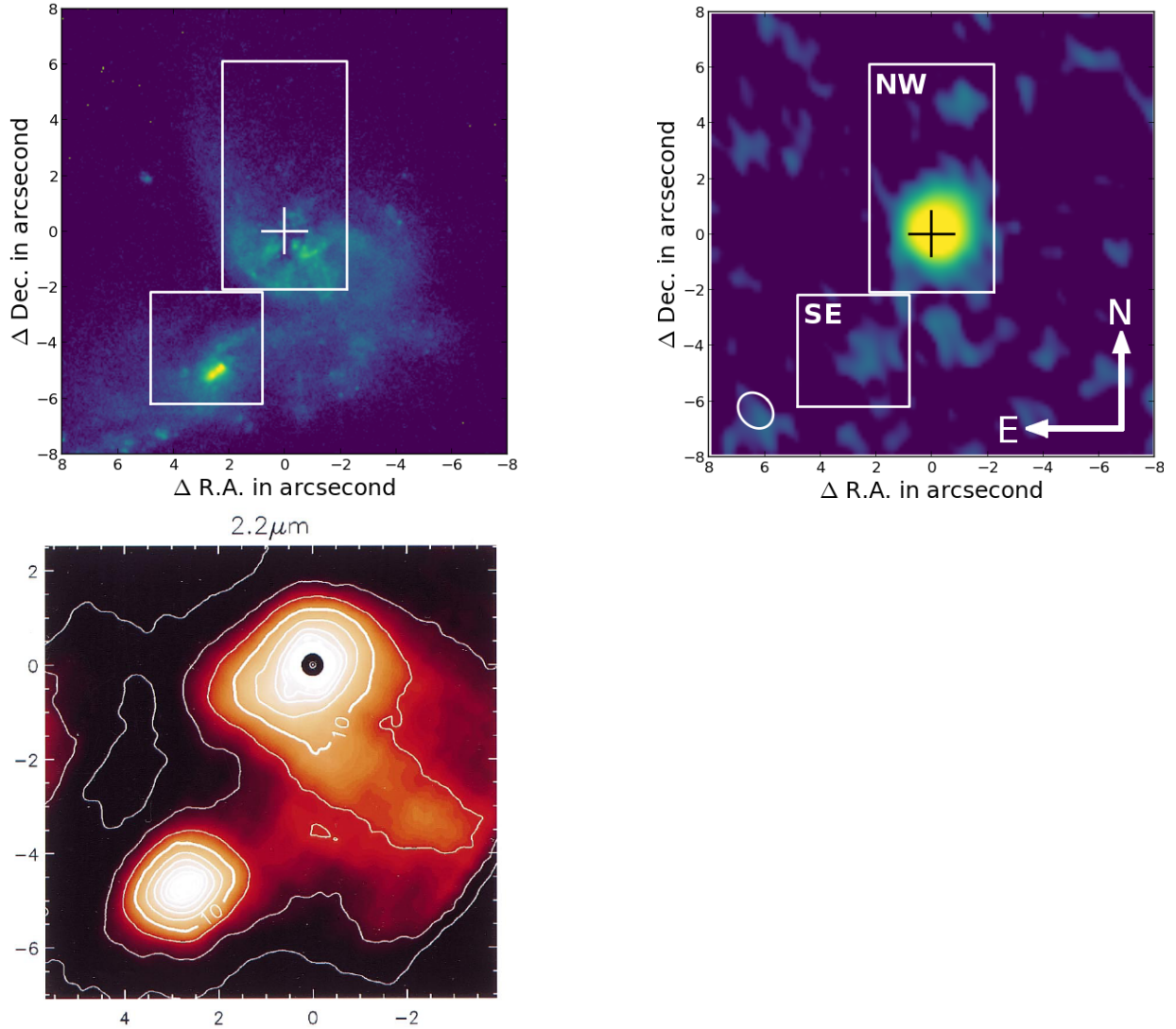[2]MAPPING is also part of the GILDAS package.

Figure 4.1: Upper Left: log intensity plot of an HST ACS WFC F435 image. The image is centered at the peak of CO(1-0) emission: this position is marked with a cross (see Section 4.3.1 for details). The boxes show the regions from which the CO spectra were extracted. Upper Right: log intensity plot of CO(1-0) with the same cross and regions as in the HST image. Note that the peak of CO emission is offset with respect to the lower isophotes. The ellipse shows the synthesized beam size of the new, configuration A+B+C+D, observations. Lower left: H-band image at $2.2\,\mu$m, showing where star formation takes place. Image adapted from Scoville et al. (2000).
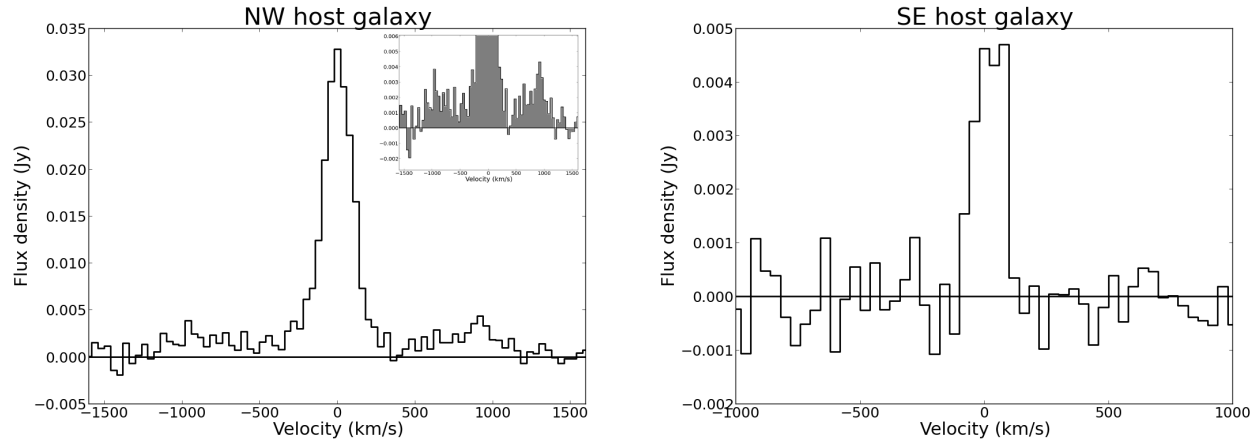
Figure 4.2: Spectra of the NW galaxy (left) and the SE galaxy (right). Figure 4.1 shows the windows from which these spectra were extracted. In both cases, the data were binned to 40 km s^{-1}.

Finally, the CO line flux is converted to H$_2$ gas mass, using a conversion factor $\alpha_{CO} = 0.8 M_{\odot} (\text{K km s}^{-1} \text{pc}^2)^{-1}$. This value is chosen in order to stay consistent with Cicone et al. (2014), and is considered appropriate for ULIRGs (Bolatto et al., 2013). Because α_{CO} enters linearly in the gas mass (on which most conclusions will depend), and is an uncertain number (in particular for the outflow), we discuss this parameter further in Section 4.3.3.4.

Maps of the different velocity ranges are shown in Figure 4.3, with the blueshifted wing on the left, the line center in the center, and the redshifted wing on the right. In each panel, the contours are placed at multiples of 3σ levels of the panel, with 1σ corresponding to the Noise level given in Table 4.2. The red wing separates into two components: an outflow at $\approx 1''$ North West of the center, and a second outflow at $\approx 5''$ North of the center (right panel of Figure 4.3). The first component will be refered to as 'the biconical outflow', assuming that the blueshifted outflow is its counterpart. We will refer to the second redshifted component as 'the second outflow'. This second, fainter, outflow has been detected before by Cicone et al. (2014), but only now it is clear that this is not just an extension of the first outflow, but a different component.

The next sections treat the different components mentioned above.

4.3.1 Main galaxy (NW)

The NW galaxy has frequently been observed and detected in CO(1-0) (Solomon et al., 1997; Evans et al., 2002; Cicone et al., 2014), and hosts a rotating disk. A spectrum of the main host, including the outflows, is given in the left panel of Figure 4.2. The integrated flux between -400 km s^{-1} and 400 km s^{-1} is 8.2 Jy km s^{-1}. The position, velocity range, flux, molecular gas mass and size of the NW galaxy is given in Table 4.2.

An elliptical Gaussian fit to the uv table of the ABCD observations gives the peak
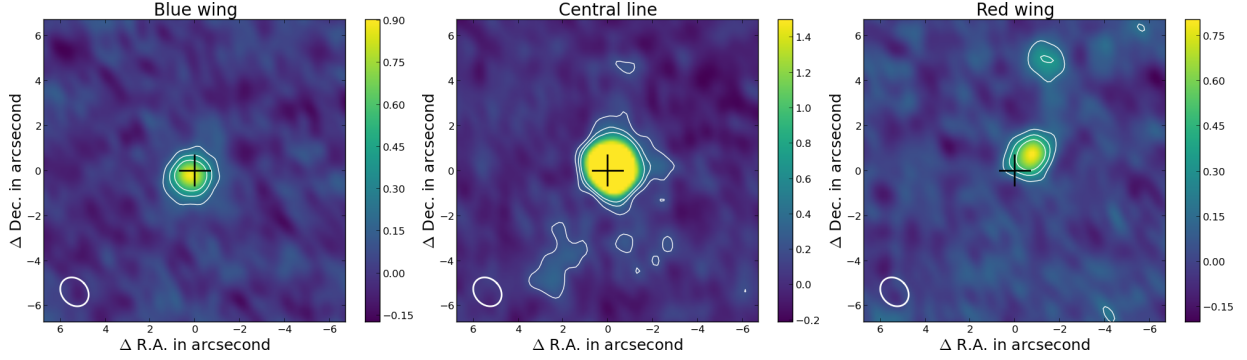
Figure 4.3: CO(1-0) maps integrated over the following velocity ranges: on the left the blue wing from -1200 to -400 km s^{-1}, in the center the central line from -400 to 400 km s^{-1}, and on the right the red wing from 400 to 1200 km s^{-1}. The contours are placed at multiples of 3σ levels. Some of the 3σ signals could be residual sidelobes from the main galaxy, except for the extended feature in the central map, which is the SE galaxy. The color bar gives the flux in mJy/beam, and has been cut at 1.5 in the central map, in order to highlight the fainter features.

	R.A. 9:00:..	Dec 39:03:..	Velocity range (km s^{-1})	Noise mJy/beam	Flux (Jy km s^{-1})	Molecular Mass ($10^9\,M_\odot$)	FWHP kpc	dM/dt $M_\odot$/year
Blue	25.40	53.9	-400 to -1200	0.056	1.3	0.17	0.92	310
NW galaxy	25.38	54.2	-400 to 400	0.065	8.2	1.04	0.70	...
SE galaxy	25.6	49	-400 to 400	0.065	0.8	0.1	1.6	...
Red 1	25.32	54.8	400 to 1200	0.055	0.9	0.1	0.98	170
Red 2	25.26	58.9	400 to 1200	0.055	0.4	0.05	0.7	120

Table 4.2: Fluxes and gas masses for the individual outflows and galaxies. $\alpha_{CO} = 0.8 M_\odot (\mathrm{K\,km\,s^{-1}\,pc^2})^{-1}$. All Full Width Half Power (FWHP) values have been derived from the uv data, except for the SE galaxy and the Red outflow 2, for which the size is estimated in the image plane.
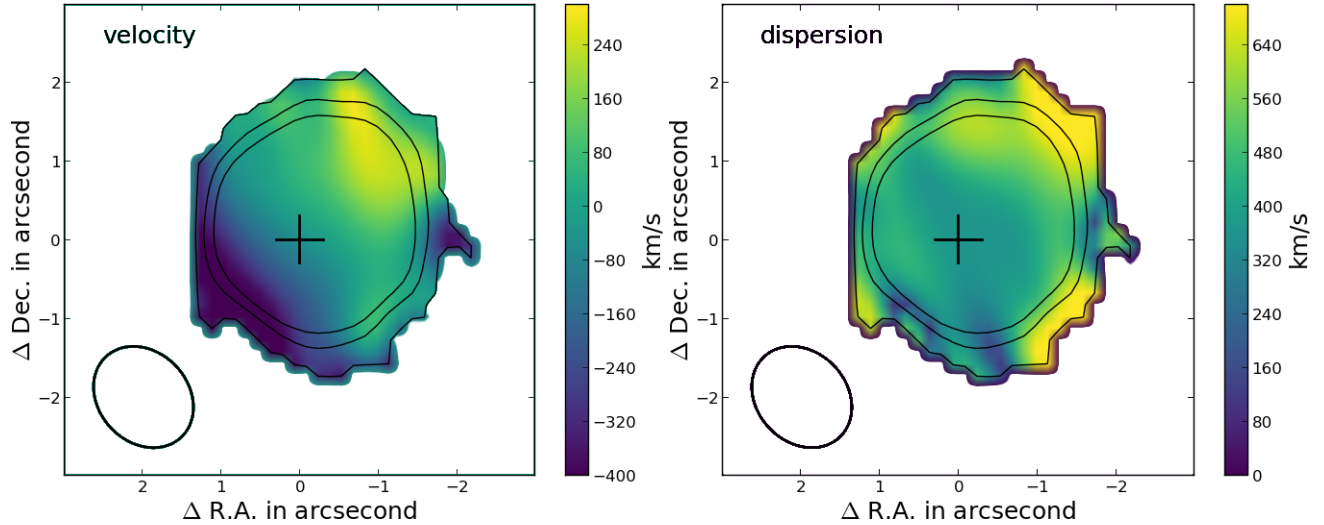
Figure 4.4: Velocity map (left) and dispersion map (right) of the NW galaxy. Contours have been placed at 3σ, 6σ and 9σ. The maps were based on the -400 to 400 km s^{-1} range, but the color bars only cover the range of velocities that appear in the maps. The kinematic major axis has a position angle of roughly $-45°$ degrees, based on the velocity gradient in the left panel.

of emission at R.A. 09:00:25.38 DEC. 39:03:54.2. The galaxy's emission is not perfectly symmetric around this point, but is more extended towards the West. Therefore the galaxy's center is offset from the lower isophotes, as can be seen in Figure 4.1 and 4.3. Still the derived position is probably a good indication of the disk's center, since it coincides within 0.1″ with the radio center at 8.44 GHz found by Condon et al. (1991). All maps were therefore centered at the peak of CO emission. The best elliptical Gaussian fit has a major FWHM of $0.61 \pm 0.2''$ and a minor FWHM of $0.54 \pm 0.2''$, corresponding to 0.74 by 0.65 kpc, with a P.A. of $-10 \pm 10°$. The disk is thus slightly elongated towards the north / north west, but because the length of the major and minor axes differ only little, the P.A. is not used here to constrain the orientation and inclination of the disk.

A Gaussian fit to the central line in the spectrum (excluding the broad wings) has a peak of 0.032 Jy, and a σ of 98 km s^{-1}. Because the redshift (0.0582) is derived from CO observations by Evans et al. (2002), the mean is 0 km s^{-1} by definition.

Figure 4.4 shows a velocity map of the disk (left panel) and the dispersion map (right panel), taken between -400 and 400 km s^{-1}. Only regions with $> 3\sigma$ detections are shown. Contours have been placed at 3σ, 6σ and 9σ. The velocity map shows a convincing but slightly disturbed rotating disk with a position angle of approximately $-45°$ degrees.

The velocity map in Figure 4.4 contains velocities from -400 km s^{-1} to 300 km s^{-1}. Part of the ~ -400 km s^{-1} emission could be due to the onset of the outflow, rather than rotational motion. Because the outflow and the disk are aligned (see Section 4.3.3), they cannot be clearly separated kinematically. There is however a significant drop in flux around the 9σ contour, which we will take as the outer radius of the disk in the derivation

of the dynamical mass. For a Position Angle of $-45°$ degrees, this results in an average velocity of $v = 320$ km s^{-1} at an average distance of $R = 1.6$ kpc. This results in a dynamical mass:

$$M_{dyn} = \frac{v^2 R}{G} = 3.7 \times 10^{10} \, M_{\odot} \tag{4.2}$$

Inclination effects have not been taken into account, so the real dynamical mass is larger. Previous estimates of the dynamical mass based on CO(1-0) by Solomon et al. (1997) and Evans et al. (2002) are a factor 10 smaller, because the disk was not spatially resolved, and a 10 times smaller radius was assumed based on radio (8.4 GHz) emission. As a comparison, Rodríguez Zaurín et al. (2009) estimate the stellar mass in the NW galaxy to be on the order of $10^{10} \, M_{\odot}$, based on fits of templates of young stellar populations to the optical spectrum.

4.3.2 Second galaxy (SE)

The central panel of Figure 4.3 shows extended CO emission at the location of the second galaxy. The peak of the CO emission, at R.A. 9:00:25.6, Dec. 39:03:49, coincides with the position of the SE galaxy in SDSS i-band images, and the molecular gas around this position displays rotational motion. The line profile of the SE galaxy has a regular shape, is narrow and peaks at $v = 30$ km s^{-1} (right panel in Figure 4.2). The line has a flux of 0.8 Jy km s^{-1}, which corresponds to a molecular gas mass of $\sim 10^8 \, M_{\odot}$ if $\alpha_{CO} = 0.8 \, M_{\odot}$ (K km s^{-1} pc^2)$^{-1}$ (Table 4.2). There is a substantial uncertainty in the flux (estimated to be $\sim 20\%$), because it is contaminated by residual side lobes from the main source, and because the emission is extended. Moreover, the CO conversion factor may be too low for this galaxy, so the molecular gas mass could be higher. A Gaussian fit to the emission in the image plane results in a FWHM of 1.8″. With an average beam size of 1.25″, the estimated (deconvolved) FWHP of the SE galaxy is 1.3″ or 1.6 kpc. The size has been fit in the image plane, because a fit in uv plane was not successful.

4.3.3 The biconical outflow of the NW galaxy

Previous observations already showed that the outflow components are spatially offset from the center of the NW galaxy (Cicone et al., 2014). The redshifted component is centered at R.A. 9:00:25.32 Dec. 39:03:54.8, at a Position Angle of $-49°$ degrees (see Table 4.2 for the position, flux, mass, and outflow rate of the outflow). The Position Angle is 0 for an object North of the image center, and increases towards the East. The blueshifted component is centered at R.A. 9:00:25.4 Dec. 39:03:53.9, at a Position Angle of 142° degrees. The two outflowing components thus lie on a line through the center of the NW galaxy, and are aligned along the disk. The redshifted part of the outflow and the receding part of the disk are on one side, while the blueshifted part of the outflow and the approaching part of the disk on the other side. This makes it a challenge to disentangle the disk rotation from the outflow.

This is illustrated in Figure 4.5 as a series of channel maps, in bins of 200 km s^{-1}. The top panel of Figure 4.5 shows the four channel maps of the blueshifted wing: the blueshifted outflow is located SE of the cross. The central panel of Figure 4.5 shows the four channels from -400 to 400 km s^{-1}; the outflow smoothly transits into the rotating disk, moving to the Northwest with increasing velocity. Then in the lower panel (400 to 1200 km s^{-1}), the redshifted outflow appears on the NW of the cross.

Note further that the blueshifted outflow is centered at the same position in all four bins from -1200 to -400 km s^{-1}; no velocity gradient is visible. Also the redshifted part of the biconical outflow remains at one position, except for the bin at 900 km s^{-1}. At this velocity, the second redshifted outflow arises, which is further discussed in Section 4.3.4. Figure 4.6 shows the velocity- and dispersion-maps of the biconical outflow and the second redshifted outflow. Also here, there is no velocity gradient in the biconical outflow. The velocities are around 800 km s^{-1}, and the dispersion is ~ 250 km s^{-1} in all parts of the outflow. In the southern tip of the blueshifted outflow the velocity decreases to -900 km s^{-1}, but a spectrum of that region looks noisy and does not provide convincing evidence for an accelerating outflow.

4.3.3.1 Geometry of the outflow

As mentioned above, no velocity gradients are observed either in the blueshifted or in the redshifted part of the outflow (Figure 4.5 and 4.6). The absence of a velocity gradient, the spatial position and extent of the outflow, and the large range of velocities observed in the outflow constrain the geometry.

Consider three possible geometries: a spherically symmetric shell (with the full 4π coverage), a bicone (a shell with an opening angle), and two individual blobs. In all cases, the outflow has a maximum velocity v_{max}, and is only slightly resolved spatially.

- A spectrum of the shell will be broad with emission at velocities ranging from $-v_{\mathrm{max}}$ to $+v_{\mathrm{max}}$. Because the outflow is hardly resolved and perfectly symmetric, the channel maps of all velocities are centered at the same point. For the same reasons, it will be hard to detect any acceleration or deceleration of the shell.

- In the case of a bicone, the spectrum may still be broad if the opening angle is large (approaching a shell), or if the bicone is directed toward the observer. But the maps do look differently from those of the shell-like outflow. Unless the outflow is pointed directly toward us, the blueshifted and redshifted emission is offset from the center of the outflow, in opposite directions. Acceleration and deceleration may be observed, depending on the opening angle θ.

- In the case of individual clouds, the observed velocity range is caused by turbulence within the clouds, rather than projection effects. Unless the cloud moves directly toward us, it should be clearly offset from the driving source. Velocity gradients can be observed when the cloud accelerates or decelerates.
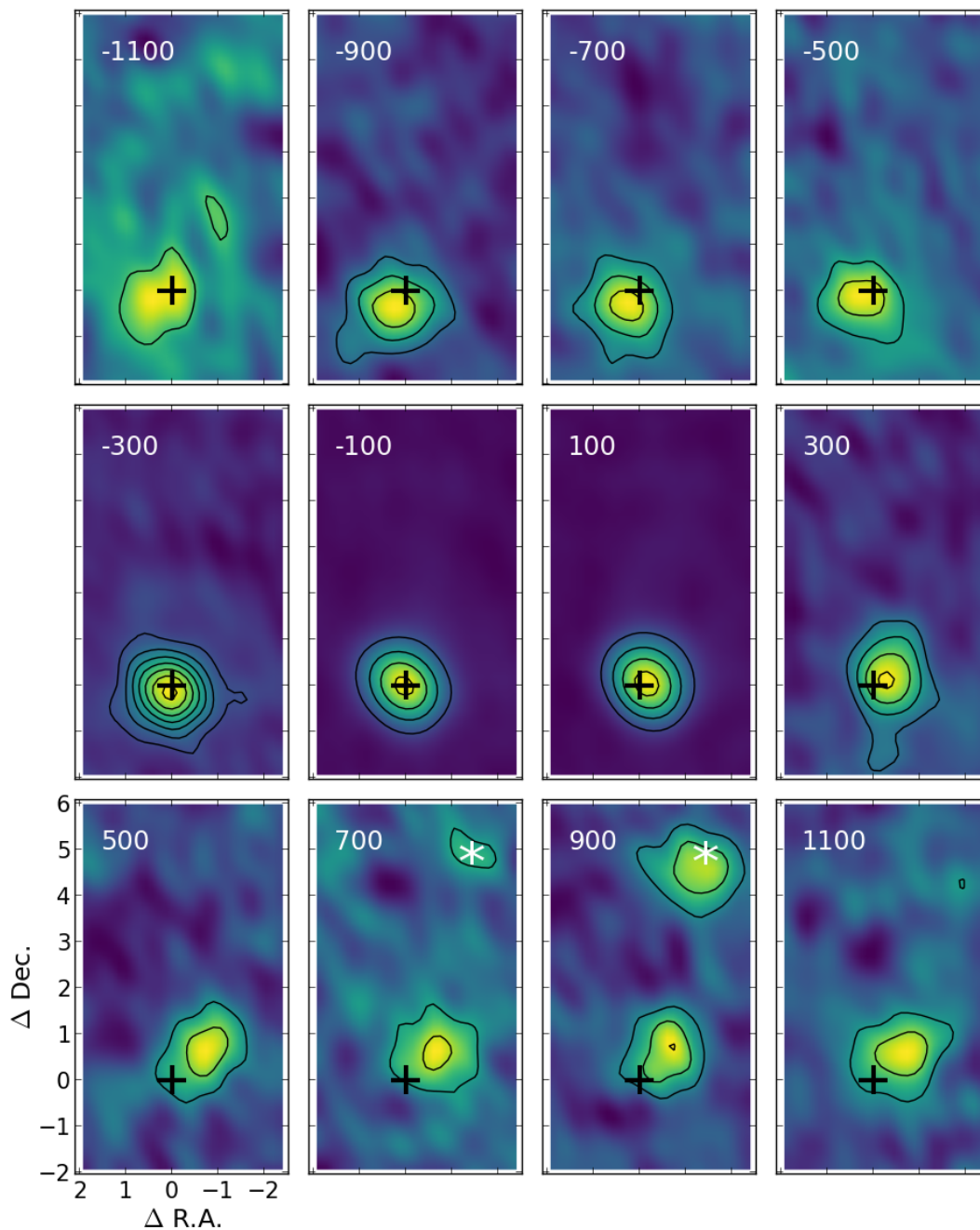
Figure 4.5: Channel maps in 200 km s^{-1} bins. The central velocity of each map is printed in white. Contours are placed at multiples of 3σ levels, except for the bins centered at -100 and +100 km s^{-1} where the contours are placed at multiples of 25σ. Each map has its own color scale, in order to make both bright and faint features well visible. Several things can be observed from these channel maps: 1) the outflow is aligned with the kinematic major axis of the disk (roughly going from the SE to the NW), 2) there is no velocity gradient in the biconical outflow (except for a shift to the north at 900 km s^{-1}), 3) the second redshifted outflow is brightest around 900 km s^{-1} and slows down with distance from the NW galaxy (Section 4.3.4). A white star is placed at the center of the second outflow in the 700 and 900 km s^{-1} maps as reference.
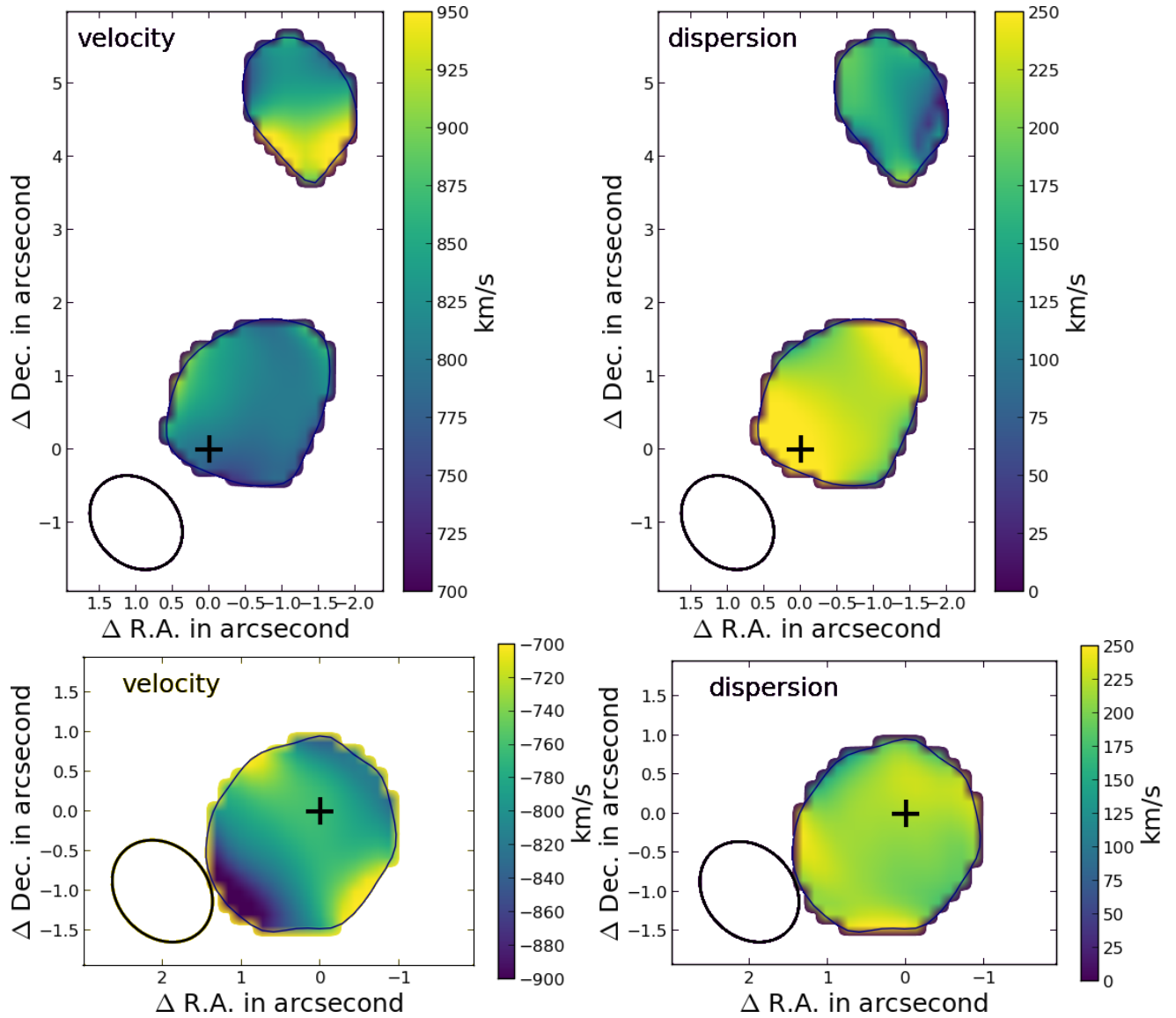
Figure 4.6: Moment 1 and moment 2 maps of the red wing (400 to 1200 km s^{-1}; upper panels) and the blue wing (-1200 to -400 km s^{-1}; lower panels). The velocity range in the color bar has been adapted to bring out the structure in the outflow. Only those areas are plotted where the total intensity $> 3\sigma$. The biconical outflow has no velocity gradient, and a high velocity dispersion. In contrast, the second redshifted outflow decelerates with distance from the NW galaxy, and has a low velocity dispersion.

The differences between these geometries is illustrated in Figure 4.7. The main outflow, that is discussed in this section, matches best with the description of the biconical outflow with a large opening angle, directed not exactly toward us but making an angle with the line-of-sight. Because of the large opening angle, we expect v_{max} to be close to the maximum observed velocity in the outflow, which is 1200 km s^{-1}. The second redshifted outflow (Section 4.3.4) matches the description of the individual cloud.

We now estimate the observed spectrum from a physically infinitely thin shell, in order to justify the choice of $v_{\text{max}} = 1200$ km s^{-1}. The right panel of Figure 4.8 shows an illustration of this simplified scenario. The radius of the shell is taken to be 1. The observed velocity and flux of gas moving under a certain angle θ with respect to the Line of Sight (L.O.S.) is:

$$v(\theta) = v_{\text{max}} \cos{(\theta)} \tag{4.3}$$

$$F(\theta)_{\text{thin}} = F_0 2\pi \sin{(\theta)} d\theta \tag{4.4}$$

$$F(\theta)_{\text{thick}} = F_0 2\pi \sin{(\theta)} \cos{(\theta)} d\theta \tag{4.5}$$

where F_0 is a normalization factor to match the observed flux, and $r(\theta) = \sin{(\theta)}$ the radius of a ring, as seen by the observer. The observed flux depends on how optically thick the outflow is. For an optically thin outflow, emission from the whole shell can reach the observer, whereas only the surface facing the observer is taken into account in the optically thick case (adding a factor $\cos{(\theta)}$ to the observed flux). Taking $v_{\text{max}} = 1200$ km s^{-1}, and scaling F_0 to the observations, results in a good correspondence between the high-velocity end of the observed spectrum and the expected emission from a physically thin shell (Left panel of Figure 4.8). Although the optically thick outflowing shell compares best to the observed spectrum, it requires the exteme assumptions of a physically thin and optically thick outflow. Instead, the drop in flux at velocities below ~ 600 km s^{-1} could also be the result of a biconical outflow with little gas flowing at angles $> 45°$ degrees from the line of sight.

4.3.3.2   Projected size of the outflow

The sizes of the two components in the biconical outflow are retrieved from Gaussian fits to the uv data. The Full Width at Half Power (FWHP) of the blueshifted part is 0.77″ or 0.92 kpc, in comparison to the 1.36 kpc found in Cicone et al. (2014): adding visibilities at larger uv radii resulted in a better fit with a slightly more compact source. For the redshifted component, the difference between our FWHP and that found in Cicone et al. (2014) is larger because the second redshifted outflow is now resolved, and not included in the Gaussian fit. This results in a FWHP of the redshifted part of 0.82″ or 0.98 kpc (compared to 1.91 kpc found previously). The FWHP is added to Table 4.2.

Compare these sizes to the projected distances to the center of the NW galaxy. This distance is 0.38″ or 0.5 kpc for the blue component, and 0.92″ or 1.1 kpc for the red

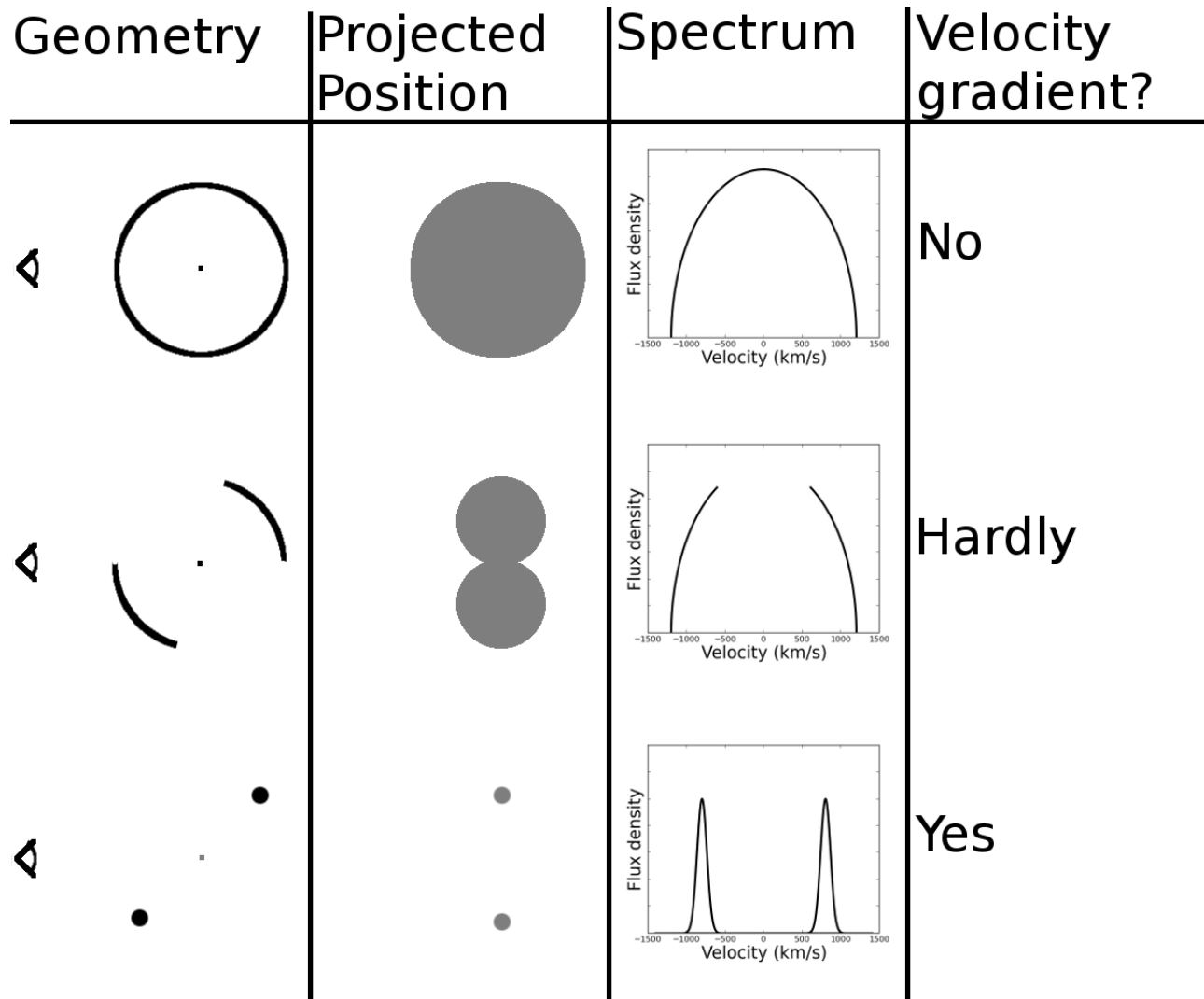| Geometry	Projected Position	Spectrum	Velocity gradient?
			No
			Hardly
			Yes

Figure 4.7: A sketch to illustrate the 3 different geometries, from top to bottom: a shell, a bicone, and individual clouds. The spectral shape is the 'optically thin' spectrum in Figure 4.8. The last column states whether any velocity gradient would be observable if the outflow is only marginally resolved spatially.
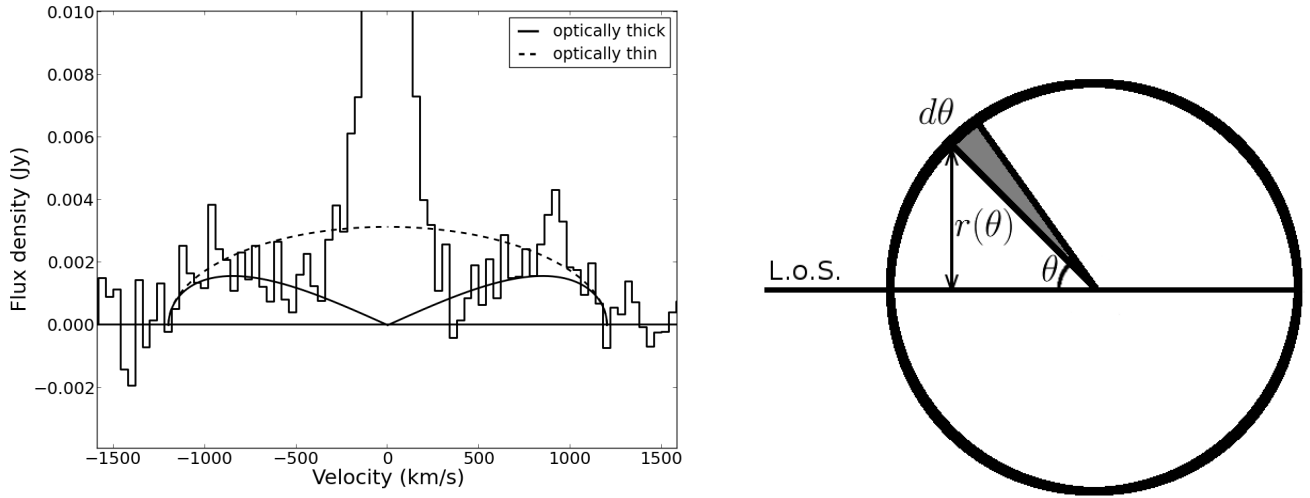
Figure 4.8: Expected emission from a physically thin shell. Left panel: the observed spectrum compared to the expected spectrum from a shell with velocity 1200 km s^{-1}, either optically thin (Equation 4.4) or optically thick (Equation 4.5). The emission around +900 km s^{-1} comes mostly from the second outflow. Right panel: illustration of the assumed geometry (full 4π covering).

component. Since the size of the red component is smaller than its distance to the galaxy, the outflow seems detached from the galaxy, as if it is not replenished with new gas (see also the channel maps in Figure 4.5). This observation suggests *that the outflow is a bursty rather than a continuous process.* This has consequences for the calculation of the outflow mass. Maiolino et al. (2012) derive the mass outflow rate for a spherical outflow that is continuously replenished with new gas, to be $\dot{M}_{\mathrm{out}} = 3Mv_{\mathrm{max}}/R$. This changes to $\dot{M}_{\mathrm{out}} = Mv_{\mathrm{max}}/\Delta R$ for a bursty outflow. In the latter case, the thickness of the outflowing shell, ΔR, is of interest. This value is hard to derive observationally in a biconical outflow, but the FWHP as given in Table 4.2 is the best approximation. Since ΔR is probably overestimated, the mass outflow rate given in Table 4.3 is a conservative value.

4.3.3.3 Comparison of the molecular, atomic and ionized outflow

The improved spatial resolution of the CO observations makes a comparison with other ISM phases of the outflow possible; earlier CO observations, OH, Na I D, Hα, [CII] and warm H$_2$.

Table 4.3 summarises the outflow properties of the different phases: the total mass in the outflow, the average (or typical) velocity, and the outflow radius in kpc (if known). When the radius is known, also the mass outflow rate ($\dot{M}_{\mathrm{out}}$), momentum rate ($\dot{M}_{\mathrm{out}}v$) and energy rate ($1/2\dot{M}_{\mathrm{out}}v^2$) are given. There are different approaches among the authors in defining the radius and outflow rate. For example Rupke & Veilleux (2013b) give the

Tracer	Mass $M_\odot$	v km/s	Radius kpc	dM/dt $M_\odot$/year	$c \times v \times dM/dt$ $10^{12} \times L_\odot$	$0.5v^2 dM/dt$ 10^{43} erg/s	Reference
1	2	3	4	5	6	7	8
Hα	8.5×10^6	1524	≤ 2	7.6	0.69	1.3	1
Na I D	7.6×10^7	403	≤ 2	24.5	0.89	0.63	1
OH	1.2×10^8	500-950	0.11	650	22	10	2
H$_2$	5.2×10^4	1000	0.4	0.13	0.006	0.004	3
[CII]	1.4×10^8	800	...	...	...	...	4
CO(1-0)$_{\mathrm{CD}}$	4.1×10^8	800	0.82	1210	47.8	24.5	5
CO(1-0)$_{\mathrm{ABCD}}$	2.7×10^8	1200	0.95	360	21	16	6

Table 4.3: Outflow properties of different ISM phases. As a comparison, the SFR is 61 $M_\odot$/year (Section 4.4.1.2). 1) Tracer 2) Total gas mass in the outflow 3) average or typical outflow velocity 4) radius in kpc 5) Outflow rate 6) outflow momentum rate 7) kinetic power in the outflow 8) References 1: Rupke & Veilleux (2013b), 2: González-Alfonso (in preparation), 3: Rupke & Veilleux (2013a), 4: Janssen et al. (2016), 5: Cicone et al. (2014), 6: this chapter. The differences between the newest CO observations (CO(1-0)$_{\mathrm{ABCD}}$) and those presented earlier (CO(1-0)$_{\mathrm{CD}}$) are mostly caused by new insights in the outflow geometry. See Section 4.3.3.2 and 4.3.3.3 for details.

largest observed projected radius of the ionized and neutral outflow, whereas Cicone et al. (2014) give the radius of the outflow extent. This can cause differences of a factor of a few in the outflow rates.

With the newest CO observations, we find a 3 times smaller mass outflow rate than derived previously by Cicone et al. (2014). This is caused by three changes: (1) the second redshifted outflow is excluded from the analysis, resulting in a smaller outflow mass. (2) the maximum observed velocity is used, rather than the average velocity. This is appropriate if the outflow is a bicone with a constant velocity and a large opening angle. (3) The outflow rate is calculated as $\dot{M}_{\mathrm{out}} = M v_{\mathrm{max}}/\Delta R$ rather than as $\dot{M}_{\mathrm{out}} = 3 M v_{\mathrm{max}}/R$, based on new insights that the outflow is bursty rather than continuous.

Sturm et al. (2011a) presented observations of the OH outflow, including a preliminary model to constrain its size and mass. Following up on this, a detailed modeling of the OH observations is done based on the line profiles of OH119, OH79, OH65 and OH84 (González-Alfonso et al. 2016, submitted), resulting in estimates for the outflow mass and size. The outflow is modeled as two expanding shells, with average velocity of 500 and 950 km s^{-1}, effective radii of 110 and 110 pc, covering factor of the FIR continuum of 0.33 and 0.2, outflow mass of 88 $\times 10^6$ and 28 $\times 10^6 M_\odot$, and outflow rates of 410 and 240 $M_\odot$/year respectively. The OH observations trace a compact outflow with a radius ~ 8 times smaller than found in CO(1-0)$_{\mathrm{ABCD}}$ (Table 4.3 lists details of the OH outflow). But with an outflow mass two times smaller than in CO and a smaller velocity, the mass outflow rate, Momentum outflow rate and Energy outflow rate are remarkably similar.

The OH observations trace only the central part of the outflow: because the blueshifted wings in the OH lines are observed in absorption, a FIR continuum background is required

in order to see the outflow. In IRAS F08572+3915, this continuum has a half-light radius as small as 0.403 ± 0.108 kpc at 70 micron, and 0.697 ± 0.128 kpc at 100 micron (Lutz et al., 2016). The OH observations are therefore not sensitive to a kpc scale blue-shifted outflow. However, the receding part of the outflow may be visible in emission when it is not covered by the optically thick disk. Indeed there is emission in the OH84 and OH65 spectra around 800 to 1000 km s^{-1}. This could be either the receding part of the biconical outflow, or the second red outflow as discussed in Section 4.3.4. In the OH model, the red part of the biconical outflow is located behind the disk, and does not contribute much to the redshifted emission.

Do OH and CO trace the same outflow? The similar outflow characteristics listed in Table 4.3 suggest that this is the case, yet the derived scale is different. This different scale may be explained as follows: the OH model is based mostly on the blueshifted absorption, because the redshifted component is located behind the disk and its emission is attenuated. In CO, the blueshifted component is located closer to the NW galaxy than the redshifted component: at a distance of 0.56 kpc (Section 4.3.3.2), it falls well within the radius of the 100 μm continuum of ~ 0.7 kpc. Therefore, if any OH is present in the CO outflow, it is expected to contribute to the observed absorption in OH119. The OH outflow radius listed in Table 4.3 is an 'effective radius', but the real radius is larger by a factor $f_c^{-0.5}$, where f_c is the covering factor. This brings the real radius of the OH model to 0.25 kpc (for $f_c = 0.2$). The radius of the CO outflow is probably overestimated, because it is taken to be the size of the outflow, which seems a reasonable approach for the redshifted component but may not be so for the blueshifted component. If the distance to the peak of the blueshifted component is taken instead, the difference between the OH model and the CO observations is only a factor 2. Considering the uncertainties, this is a small difference, so OH and CO may indeed trace the same outflow.

Rupke & Veilleux (2013a) present OSIRIS/Keck observations of the warm H$_2$ outflow, which has velocities of -700 km s^{-1} to -1000 km s^{-1}. The warm H$_2$ outflow is aligned with the kinematic major axis of the disk, like the outflow detected in CO(1-0) (Figure 4.9). Because the FoV of the H$_2$ observations is only $1'' \times 2.9''$, the observations do not cover the whole outflow. The outflow mass and outflow rate in warm H$_2$ is $\sim 10^{-4}$ times the mass and outflow rate traced by CO (Table 4.3). The same mass ratio between warm H$_2$ and cold H$_2$ (traced by CO(1-0)) was found in M82 by Veilleux et al. (2009b).

The warm molecular outflow may also have been detected in the CO band-heads of the v = 1-0 vibrational transition at 4.7 μm (Geballe et al., 2006; Shirahata et al., 2013). Blueshifted absorption is detected in rotational transitions up to J = 17. The observations imply a shell-like expansion with a velocity of 350 km s^{-1} and a temperature of ~ 270 K. This must come from a region with a diameter of at most 260 pc, based on the extent of the continuum in the NIR and MIR (Soifer et al., 2000).

The outflow is also detected in the atomic phase, with a factor 3.5 lower mass than that traced by CO, and the ionized phase, with a factor 32 lower mass than in that traced by CO (Rupke & Veilleux, 2013b). The derived outflow rate of ionized and atomic gas, as given in Table 4.3, is much smaller the molecular outflow rate. This is partly because of the lower outflow mass, but also because of the larger outflow radius which has been
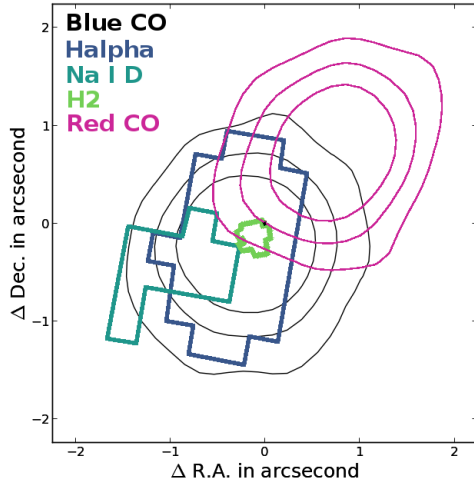
Figure 4.9: Several ISM phases in the blueshifted outflow overplotted, all are aligned with the kinematic major axis of the disk. The FoV of the H_2 observations was too small to capture the full extent of the outflow. Absorption by the galaxy's disk is probably the reason that the redshifted outflow is only detected in CO.

defined as the maximum distance from the center by Rupke & Veilleux (2013b). Both the ionized and atomic outflows trace the blueshifted molecular outflow well, and are aligned with the kinematic major axis (see Figure 4.9). Note that these observations were centered on the NIR nucleus, while the CO observations were centered on the peak of CO(1-0) emission. Because the disk is observed both in Hα and in CO(1-0), we compared the velocity plots, and conclude that the offset is certainly below $0.5''$ (0.6 kpc). The FoV of these observations is $5'' \times 7''$ and covers both components of the biconical outflow. Still, only the blueshifted part of the atomic and ionized outflow is detected, probably because the redshifted part is obscured by the disk.

Summarizing, the cool molecular gas, as traced by OH, C$^+$ and CO(1-0), is the dominant phase in the outflow, followed by the atomic gas and the ionized gas. All tracers are detected along the kinematic major axis of the disk, and overlap with the blueshifted part of the biconical outflow.

4.3.3.4 Uncertainties in the outflow mass

Uncertainties in the outflow mass arise mostly from the conversion from CO luminosity to the total molecular gas mass. Because the CO(1-0) line quickly becomes optically thick, the molecular gas mass cannot be calculated directly from the CO luminosity, but relies on a conversion factor: α_{CO}. This factor assumes CO traces optically thick virialized molecular clouds. In our galaxy, $\alpha_{CO} \approx 4.6\,M_\odot$ (K km s^{-1} pc^2)$^{-1}$ (Solomon et al., 1987), but for ULIRGs a value of 0.8 is typically used in order to make the gas mass consistent with the dynamical mass (Bolatto et al., 2013). In principle the gas in the outflow could be optically thin, in which case the conversion factor becomes $0.34\,M_\odot$ (K km s^{-1} pc^2)$^{-1}$

(for $\chi_{CO} = 10^{-4}$ and $T_{ex} = 30$ K; Bolatto et al. (2013)). Here we use $\alpha_{CO} = 0.8 \, M_{\odot}$ (K km s^{-1} pc^2)$^{-1}$ in order to stay consistent with Cicone et al. (2014).

How do the outflow masses derived from CO, OH and [CII] compare? The outflow mass derived from CO(1-0) is a factor ~ 2 larger than that from OH or [CII] (Tabel 4.3). Every tracer has however its own limitations. The major uncertainty in the CO measurements is α_{CO}. OH is sensitive to the innermost regions of the galaxy, because it appears most strongly in absorption of a FIR background with limited extent (Section 4.3.3.3). Moreover, the OH abundance is now taken to be $X_{OH} = 2.5 \times 10^{-6}$, but is uncertain by a factor ~ 3. The [CII] outflow mass has been calculated from the total area under a Gaussian fit to the line wings, and therefore also includes emission from $-400 < v < 400$ km s^{-1} (Janssen et al., 2016). The reason is that the outflow could not be spatially resolved, and was assumed therefore to be spherically symmetric. Moreover, C$^+$ traces different gas than CO(1-0), and is therefore not expected to result in exactly the same mass. Also here, an abundance had to be assumed; $X_{C^+} = 1.4 \times 10^{-4}$. Taking all these limitations into account, it is reassuring that three independent detections of the molecular outflow result in the same total outflow mass within a factor of ~ 2. Gas masses that were found using $\alpha_{CO} = 0.8 \, M_{\odot}$ (K km s^{-1} pc^2)$^{-1}$ should therefore be a reliable estimate of the molecular gas mass in the outflow.

4.3.3.5   Depletion time scale

In order to calculate the depletion time scale, it is assumed that only the biconical outflow is removing gas from the galaxy. The second redshifted outflow, observed at 4.9″ North of the NW host, is considered an earlier outflow phase that no longer plays a role in depleting the galaxy of gas. The total molecular gas mass of the NW galaxy plus the biconical outflow is $1.31 \times 10^9 \, M_{\odot}$ (Table 4.2), and with a mass outflow rate of 360 $M_{\odot}$/year (Table 4.3), this results in a depletion time scale of 3.6 Myr. An even shorter time scale of 1.3 Myr was found from OH in Sturm et al. (2011a) (2 Myr in the newest OH models). Since the depletion time scales from OH scale roughly inversely proportional to the AGN luminosity, Sturm et al. (2011a) concluded that the extreme outflows represent a short-lived, AGN dominated, stage in the evolution of the galaxy. Another indication that driving the outflow is a non-continuous process, is the presence of the second redshifted outflow, which is discussed below.

4.3.4   The second red-shifted outflow 4.9″ NW of the host

The second part of the redshifted outflow is located at R.A. 9:00:25.26 Dec. 39:03:58.9, at 4.9″ or 5.9 kpc from the NW galaxy. It has a flux of 0.4 Jy km s^{-1}, corresponding to $5 \times 10^7 M_{\odot}$. No optical counterparts for this outflow have been found. The size of the outflow cannot be retrieved from a Gaussian fit in the uv-plane, because it is faint and close to the biconical outflow. We therefore estimate the size from a Gaussian fit in the image plane, deconvolved with the beam size. The FWHM = 0.7 kpc.

The gas in this outflow has a higher velocity than in the biconical outflow. Velocities range from 600 to 1100 km s^{-1}, with the peak of emission at 920 km s^{-1}. At this velocity, the redshifted part of the biconical outflow is displaced with respect to other velocities: it is spatially shifted toward the second outflow (See Figure 4.5). Possibly there is some connection between the two outflows, confirming that the second blob of redshifted emission is a real outflow and not a distant galaxy.

Although the outflow is barely resolved, it seems to have a velocity gradient. The side facing the galaxy has the largest velocity, ranging from 800 to 1100 km s^{-1}. The velocity decreases to about 600 km s^{-1} with increasing distance to the host. This velocity gradient can be see in the channel maps of 700 and 900 km s^{-1} in Figure 4.5: the position of the outflow has shifted. More precisely, Δ R.A. = 0.05$''$±0.03$''$, and ΔDec = 0.52$''$±0.03$''$. The projected distance range is thus 0.63 kpc, over a projected velocity range of 200 km s^{-1}, resulting in a gradient of $\sim 300\,$km s^{-1} kpc^{-1}. Possibly the velocity gradient is extended to the 1100 km s^{-1} bin, but the outflow does not look as concentrated/Gaussian any more at these velocities, so we do not discuss this velocity bin further. We checked that the observed velocity gradient is not a coincidence that appears only at a certain bin size. The gradient is seen in all channel maps, regardless of their bin-size or telescope configuration. Moreover, the shift is observed in spectra taken at different distances from the host. We therefore conclude that the velocity gradient is real. Since there is no clear obstacle in the way of the outflow, the gas might simply slow down as a result of gravitational pull and the lack of an ongoing driving mechanism.

If projection effects in the velocity and distance from the NW galaxy cancel out, the flow time of the outflow is $t = R/v = 6\,$Myr, assuming the gas has been driven out all the way from the center at a constant velocity of 900 km s^{-1}. This time scale is consistent with episodic AGN driven outflow, as discussed further in Section 4.4.2.3.

4.4   Discussion

The new observations increase our understanding of the powerful outflows observed in local ULIRGs. Although the sample presented in Chapter 3 has been studied in great detail, there are still open questions like 'is the molecular phase the dominant phase in the outflow (compared to ionized and atomic phase)?' and if so, 'do the molecules survive the acceleration to 1000 km s^{-1}, or do they form later in the fast moving gas?'. Other questions are: 'is the outflow mostly momentum- or energy-driven?', and 'what is the outflow geometry?'. Answering these questions requires deep observations of the different outflow phases, which is time consuming, and has therefore only been possible for a few objects. With all available observations, IRAS F08572+3915 is now a good example of hosting an (AGN-driven) outflow, which can be used for detailed studies.

Arguably, the only outflow in the ULIRG sample that has been studied in more detail is the one in Markarian 231. This outflow has not only been detected in CO(1-0), OH, C$^+$, Na I D and Hα (Feruglio et al., 2010; Fischer et al., 2010; Sturm et al., 2011a; Rupke & Veilleux, 2013b; González-Alfonso et al., 2014; Janssen et al., 2016), but also in X-rays, CO(2-1),

CO(3-2), HCN, HCO$^+$, HNC and HI (Cicone et al., 2012; Aalto et al., 2012; Feruglio et al., 2015; Morganti et al., 2016; Lindberg et al., 2016). The outflow velocity derived from CO observations is only half the velocity in IRAS F08572+3915. The redshifted and blueshifted component in the CO(2-1) observations by Cicone et al. (2012) and Feruglio et al. (2015) are centered at the same position, ~ 0.2 kpc off the nucleus. Probably the outflow is more spherically symmetric than the one in IRAS F08572+3915, and it shows signs of deceleration in OH and in CO(2-1) (González-Alfonso et al., 2014; Feruglio et al., 2015).

The next Sections discuss whether the biconical outflow in IRAS F08572+3915 is driven by the AGN, star formation, or whether it could be merger-induced tidal tails. Finally, we discuss the outflow energy rate and momentum rate, the duration of the second outflow in terms of AGN variability, and the origin of the molecular gas in the outflow.

4.4.1   Driving mechanisms

4.4.1.1   Merger-induced streams

The optical image from the Hubble Space Telescope, presented in Figure 4.1, clearly shows tidal arms. The galaxies have passed first pericenter, and the gas is disturbed. Could tidal interactions explain the fact that the two galaxies are aligned with the outflows and the rotation pattern of the disk? In other words; is it possible that the SE galaxy happened to fall onto the NW galaxy along the rotational direction of the NW disk, hereby stripping gas off the rotation disk? And could this explain the observed outflows?

We consider this scenario unlikely. First of all, the arms in Figure 4.1 suggest that the merging is taking place in a plane roughly perpendicular to our line of sight. This is confirmed by the central velocity of the second host, which is only 30 km s^{-1} red-shifted with respect to the NW galaxy. The gas in the tidal arms is therefore most likely moving perpendicular to our line of sight, and would need to have very high velocities in order to be observed with a radial velocity of 1000 km s^{-1}.

Even if the deprojected velocity is 'only' 1000 km s^{-1}, this is rather high for a tidal tail. Consider a particle at infinity, falling frictionless onto a pointmass of 10^{11} $M_\odot$ (a plausible total mass for a spiral galaxy). If all the gravitational potential energy ($-GMm/r$) is transformed to kinetic energy ($0.5mv^2$), then the particle attains a velocity of $v = \sqrt{2M_{dyn}G/R} = 943$ km s^{-1} at 1 kpc distance. This velocity is almost as high as the observed velocity, and if the SE galaxy already had a velocity of a few 100 km s^{-1} towards the NW galaxy before the merger started, then the maximum velocities of 1200 km s^{-1} can be explained. However, in this case the infalling galaxy would easily reach the escape velocity, and would not end up next to the NW galaxy with a similar radial velocity.

Second, the rotation disk looks little affected by the merger. Shapiro et al. (2008) present velocity maps and velocity dispersion maps of modelled mergers. The disks of merging systems are asymmetric compared to the 'undisturbed' disks. The velocity distribution in IRAS F08572+3915 is symmetric and regular (Figure 4.4). The dispersion is high compared to a normal rotating disk, and reach velocities as high as > 600 km s^{-1} in

the NW where the redshifted outflow is located. Such high velocity dispersions are not found in the 'fast rotating gas rich mergers' in Naab et al. (2014), and are probably due to a 'real outflow' rather than the merger.

And finally, the P-Cygni profile in OH119 is hard to explain by streams of gas, and favours a shell-like outflow (González-Alfonso et al., 2016, submitted).

In summary, although the merger certainly has its effects on the gas kinematics of the NW galaxy, it is probably not the main cause of the observed molecular outflow.

4.4.1.2 Star formation

Another possible driver of the outflows is star formation. We calculate the SFR from Kennicutt (1998):

$$SFR(M_\odot/\text{year}) = 4.5 \times 10^{-44} L_{8\text{-}1000,SF}(\text{erg/s}) \tag{4.6}$$

where we take for $L_{8\text{-}1000,SF}$ the NIR+FIR luminosity produced by star formation. This fraction of the total NIR+FIR luminosity is estimated from $(1 - \alpha)L_{8\text{-}1000}$, with α the AGN fraction. Veilleux et al. (2009a) presents six methods to estimate the contribution of the AGN to the total FIR luminosity of almost 100 ULIRGs and Quasars, as observed with the Spitzer Infrared Spectrograph. The methods include the [O IV]/[Ne II] and [Ne V]/[Ne II] ratio, the PAH 7.7 μm equivalent width, the 5-25μm to FIR continuum ratio, the f_{30}/f_{15} ratio. All methods give an AGN fraction of > 0.5 for IRAS 08572+3915; $\alpha_{agn} = [0.592, 0.945]$ with an average of 0.72, which we will use for further calculations. Since $L_{FIR} = 10^{12.1} L_\odot$, the star formation rate is 61 $M_\odot$/year. Note that the derived outflow rates from CO and OH are respectively 5.9 and 11 times larger than the SFR (Table 4.3). Can star formation drive winds with these mass loading factors ($\dot{M}_{OF}/$ SFR)?

Hopkins et al. (2012) model the effect of stellar feedback in several types of galaxies (no AGN feedback is considered). The model includes: 1) local momentum deposition from radiation pressure, SNe and stellar winds, 2) Supernova and stellar wind shock heating, 3) gas recycling, 4) Photoheating of HII regions and 5) Long-range radiation pressure. In a small starforming galaxy, the mass loading can become ~ 5, which is hardly enough to explain the observed mass loading. Moreover, at more massive galaxies with larger SFRs, the mass loading is expected to drop, rather than to rise. For high-z galaxies and ULIRGs the mass loading factor is estimated to be < 2. Star formation alone is therefore probably not enough to drive the observed outflows.

4.4.1.3 AGN

The center of the NW galaxy hosts a dust-obscured AGN, possibly in combination with a central star cluster. Indications for this scenario come from all wavelength ranges.

- Iwasawa et al. (2011) detect the source in X-rays, using the Chandra telescope. In the 0.5-2 keV range, the detection rate is $(0.12 \pm 0.09) \times 10^{-3}$ counts s^{-1} (the detection is thus less than 2σ significant, and because most of the emission comes from the SE

host, it is considered a non-detection for the NW host). The detection rate in the 2 to 8 keV range is $(0.45 \pm 0.18) \times 10^{-3}$ counts s^{-1}. Iwasawa et al. (2011) present the object as a compton-thick AGN candidate. In the hard X-rays, the NW galaxy is not detected with Nustar (3-79 keV) after 24.1×10^3 s (Teng et al., 2015). But the observation is too shallow to impose strong constraints on the intrinsic AGN luminosity.

- In the radio, compact emission is observed, with FWHM $0.09'' \times 0.07''$ (100 pc by 80 pc) at 8.44 GHz (Condon et al., 1991). This can be caused either by an AGN or a nuclear star cluster.

- The [OIII]/Hβ, [NII]/Hα, [SII]/Hα, and [OI]/Hα optical line ratios appear in the composite- or Seyfert-regime in a BPT diagram (Veilleux et al., 1995; Yuan et al., 2010).

- Efstathiou et al. (2014) fits the SED from the NIR to the FIR with a torus model + a starburst model. Although one of the two models is sufficient for a reasonable fit to the SED, the best fit is a combination of both models, in which the AGN contributes 90% to the total luminosity of the object.

- Deep silicate absorption is observed in the mid-infrared spectrum (Dudley & Wynn-Williams, 1997; Spoon et al., 2007), hinting at a compact energy source, surrounded by dust. At 8.7 μm, the source is unresolved in Canaricam observations, with a FHWM of $\sim$ 330 pc (Alonso-Herrero et al., 2016). Veilleux et al. (2009a) find from further MIR diagnostics that the AGN dominates the IR luminosity (as described above in the Section 4.4.1.2).

That an AGN is not only present, but is also the main driver of the outflow, is suggested by the plots of AGN luminosity vs. outflow rate (Cicone et al., 2014) and outflow velocity (Veilleux et al., 2013). In both cases, a trend with AGN luminosity is seen for objects with a powerful AGN, and IRAS F08572+3915 follows this trend (also when the lower outflow rate from the CO(1-0)$_{\mathrm{ABCD}}$ observations is used). Therefore, we consider the AGN as the main driver of the outflows.

4.4.2   Comparison with models and other observations

Large-scale hydrodynamical simulations of galaxy formation, like the Illustris and EAGLE simulations, implement stellar and AGN feedback in order to match the observed stellar masses of galaxies (Vogelsberger et al., 2014; Crain et al., 2015; Schaye et al., 2015). Because of the large range in scales, it is computationally impossible to model a representative volume of the universe and simultaneously resolve the pc-scales at which feedback originates. The effect of these processes are therefore calculated in a simplified way. In the case of AGN feedback, typically 10% of the accreted mass is assumed to be transformed to radiation, and 5-15% of that radiation is coupled to the gas and drives outflows (Springel

et al., 2005; Booth & Schaye, 2009). However, subresolution models are required for detailed studies of complex processes like star formation, radiative cooling, and feedback processes. The presented observations will be compared to some of these detailed studies, and could provide input for some of them.

4.4.2.1 Molecular gas at 1000 km s^{-1}

The high velocities of the molecular outflow need explanation, since molecular clouds are expected to disrupt before reaching a velocity of 1000 km s^{-1}, if they are accelerated by a hot wind. Scannapieco & Brüggen (2015) and Brüggen & Scannapieco (2016) perform 3D hydrodynamical simulations of cold ($T \approx 10^4$ K), spherical clouds in a hot wind. The clouds hardly reach 100 km s^{-1} within the disruption time scale (for the maximum values modelled for $v_{hot} = 3000$ km s^{-1} and Mach number 11.4).

How do feedback models explain the existence of molecular gas at 1000 km s^{-1}? Zubovas & King (2014) model a spherically symmetric energy-driven outflow, caused by a fast (0.1c) wind from the accretion disk around the SMBH that shocks against the ISM. Although the temperature ahead of the shock front is of the order of 10^7 K, part of the gas cools through bremsstrahlung and metal line cooling to 10^4 K, after which (atomic and molecular) hydrogen and metal line cooling bring the temperature further down. The resulting molecular gas is in pressure equilibrium with the hot, tenuous gas, and moves at speeds of a thousand km s^{-1}. In this particular model, the inner radius of the molecular outflow is $R_{in} \sim 0.5 \, M_8/\sigma_{200}$ kpc. This is the same order of magnitude of the observed CO outflow, but we can not do a detailed comparison since the black hole mass M_8 is unknown.

The molecular gas in the outflow should even be able to form stars. We see no clear signs of star formation in the outflow. The redshifted outflow blob at 4.9″ North of the NW galaxy does not have an optical counterpart, so the presence or absence of stars cannot be confirmed. The Hα emission from the biconical outflow, mentioned in Section 4.3.3.3, has velocities of over 2000 km s^{-1} (Rupke & Veilleux, 2013b), and probably arises from the ionized outflow rather than from stars imbedded in the molecular outflow.

4.4.2.2 Outflow geometry

Zubovas & King (2014) also suggest that the spherical symmetry is too simplified, and that the cold phase may be more prominent along the disc, while the hot ionized gas moves perpendicular to the disc. This could well be the case in IRAS F08572+3915: if the molecular outflow moved perpendicular to the disk, it would appear in projection along the minor kinematic axis of the disk. Instead, the outflow appears along the major kinematic axis, and could therefore be equatorial. Do we detect the hot phase that is expected perpendicular to the disk? Probably not, because the Hα outflow aligns well with the molecular and atomic outflow, and is thus part of the 'cold phase'; Figure 4.9. Dugan et al. (2016) find a similar result: they model a biconical wind perpendicular to the disk, at 45 degree angle with the disk, and directly into the disk. Most mass was picked up by the outflow in the last case, confirming that massive outflows can be formed by gas

stripping off the disk.

4.4.2.3   An outflow burst $\sim$ 6 Myr earlier

The redshifted blob at 4.9″ N of the NW galaxy could be the result of an earlier outflow phase. If deprojection effects in velocity and radius cancel out (as assumed in Section 4.3.4), the flow time from the center of the galaxy is 6 Myr. With a typical size of 0.7 kpc, the duration of the outflow is 0.7 Myr (at a velocity of 900 km s^{-1}). Although these numbers are only very rough estimates, they complement other evidence that AGN flicker. According to Schawinski et al. (2015), galaxies that host a bright central X-ray source but no narrow line region (optically elusive AGN) might contain AGN that have just switched on. Combining the time it takes to ionize the Narrow Line Region with the fraction of observed optically elusive AGN, results in an estimate of the typical time an AGN is switched on. Something similar can be done when the AGN switches off, in which case the X-ray source disappears but the NLR remains visible for a while (Keel et al., 2012). These methods result in active times of the AGN on the order of 10^5 years. There are many methods to find AGN variability, each with its own caveats. For a good overview of observational evidences for AGN variability, see Hickox et al. (2014). Note here that our observations are not sensitive to time scales $< 10^6$ year, because we do not have the spatial resolution to resolve the individual blobs. The longer time scale we find is thus not in contradiction with earlier findings: it rather implies that AGN are variable over several time scales, in particular in the case of mergers.

Theoretical arguments can be found to explain AGN variability of time scales ranging from 10^5 to 10^8 years. King & Nixon (2015) derive a typical time scale of 10^5 years for an accretion disk with Height/Radius $= 10^{-3}$. Simulations of the evolution of galaxies where both AGN and stellar feedback are taken into account, by Hopkins et al. (2016), find strong AGN variability at the 10^6 year time scale. This time scale is also found by Gaspari et al. (2013), who model accretion onto an AGN, including the effects of heating, cooling and turbulence. Springel et al. (2005) explicitly model a galaxy merger, and find an increase of a factor 100 in accretion rate in 10^8 years, but there may also be strong variation at smaller time-scales, which are not resolved in this particular model. Our Myr-time scales are therefore consistent with other observations and theoretical models.

4.4.2.4   Momentum-driven or energy-driven

There are two ways to drive an outflow; through energy conservation (energy-driven) and through momentum conservation (momentum-driven). If gas around stars or AGN heats up faster than it cools (energy-conserving), it will exert pressure onto the surrounding ISM and drive an outflow. Alternatively, the stars and AGN may inject momentum in the surrounding ISM through fast particles and photons (momentum-conserving). An extensive discussion on these two mechanisms in the context of stellar feedback is given by Dyson (1984). One may distinguish between the mechanisms, by comparing the observed momentum rate and energy rate in the outflow to the momentum output rate and radiative

luminosity of the stars and AGN.

The molecular gas, traced by CO(1-0) and OH, has a larger outflow rate, momentum rate and energy rate than the atomic or ionized gas, by a factor > 10 (Table 4.3). Therefore the molecular outflow puts the strongest constraints on the driving mechanism. Because the energetics of OH and CO are similar, it does not matter which tracer is used: CO will be used here, but similar results are found from OH in González-Alfonso et al. (2016, submitted).

The kinetic power in the outflow is 2.6% of the galaxy's bolometric luminosity, while the momentum rate in the outflow is ~ 13 times the total momentum flux L_{bol}/c. If only the AGN luminosity is taken into account, these numbers become 3.6% and 19. Momentum-driven models can explain momentum boosts of a factor a few, if photons are absorbed and re-emitted by dust grains, effectively depositing their momentum several times (Ishibashi & Fabian, 2015). But a momentum boost of a factor 19 is rather large, and suggests that the outflow is energy-driven. Energy-conserving models explain momentum boosts of a factor 10-20 by a fast nuclear wind ($v = 30.000$ km s^{-1}) that sweeps up ambient material to $v = 1000$ km s^{-1} (Faucher-Giguère & Quataert, 2012).

Regardless of whether the outflow is momentum-driven or energy-driven, a nuclear wind (close to the AGN) is expected to have a momentum rate of $\sim L_{AGN}/c$. Observations of nuclear ultra-fast outflows in Markarian 231 and IRAS F11119+3257 suggest that this is indeed the case in some objects (Tombesi et al., 2015; Feruglio et al., 2015).

Of course, the outflow need not be purely momentum- or energy- driven, and a combination of both mechanisms is likely at play (Zubovas & Nayakshin, 2014).

4.5   Conclusion

We have spatially resolved the molecular outflow in the NW galaxy of the merging ULIRG IRAS F08572+3915, using NOEMA observations of the CO(1-0) rotational line. The massive molecular outflow was already detected in CO, but not with high enough spatial resolution to derive the outflow geometry. This is now possible with new observations, due to improved sensitivity ($\sigma = 0.055$ mJy/beam) and spatial resolution ($1.4'' \times 1.13''$). Although the derived outflow rate, kinetic power and outflow moment rate have dropped by a factor 3, this does not change the conclusions found in Cicone et al. (2014). From the new observations we find the following:

- The outflow geometry is a bicone with a large opening angle, a maximum velocity of 1200 km s^{-1}, and is aligned (in projection) with the kinematic major axis of the disk of the NW galaxy. The alignement with the disk suggests a coplanar outflow.

- The SE galaxy of the merger is very faint in CO, but has been detected now for the first time. Its spectrum peaks at 30 km s^{-1} redshifted with respect to the NW host. This confirms that the two galaxies lie in a plane almost perpendicular to our line of sight, as is suggested already by optical images of the merger.

- Star formation, the merger and the AGN probably all contribute to the outflow. Based on the presence of a powerful AGN and the location of the object in L_{AGN} versus outflow rate plots, we conclude that the AGN is the main driver of the outflow. The main reasons for not considering star formation as the main driver, is the high outflow rate ($360\,M_\odot$/year) compared to the SFR ($61\,M_\odot$/year) and the high outflow velocity. Moreover, the outflow is bursty (on Myr time scales) rather than continuous, which suggests a variable driving source like an AGN. As for the merger, the high outflow velocity is hard to explain in a merger that takes place in a plane perpendicular to our line of sight.

- Positions of the outflow detected in the other ISM phases (atomic, ionized), agree well with the position of the CO outflow. The blueshifted part of the biconical outflow overlaps spatially with outflows detected in Hα, warm H$_2$ and Na I D. These optical tracers are not detected at the redshifted outflow, probably due to obscuration.

- A second outflow component is detected at $4.9''$ North of the NW host, possibly due to an earlier outflow phase. It has a projected velocity of 600 to 1100 km s^{-1}. If projection effects in position and velocity cancel out, the flow time from the NW galaxy is 6 Myr, and the width of the outflow corresponds to 0.7 Myr. These numbers are consistent with a 'flickering AGN'.

- The second outflow component mentioned above has a velocity gradient of $\sim 300\,\mathrm{km\,s^{-1}\,kpc^{-1}}$, with the velocity decreasing with increasing distance from the galaxy. Since no obstacle is detected in the optical, this decreasing velocity might be the result of gravitational pull in combination with the lack of an ongoing driving mechanism.

- Despite high uncertainties in the conversion factor α_{CO}, the kinematics derived from CO are consistent with those found from OH and [CII] (within a factor 2.3) for $\alpha_{CO} = 0.8\,M_\odot\,(\mathrm{K\,km\,s^{-1}\,pc^2})^{-1}$, which is the value used in Cicone et al. (2014) and is considered appropriate for ULIRGs.

- The biconical outflow has a momentum rate of 13 (19) times the momentum rate based on L_{bol} (L_{AGN}), and an energy rate of 2.6% (3.6%). The momentum seems rather large for a purely momentum-driven outflow, so energy-conserving phases are probably part of the driving mechanism.

4.6 Acknowledgements

Space Telescope, and obtained from the Hubble Legacy Archive, which is a collaboration between the Space Telescope Science Institute (STScI/NASA), the Space Telescope European Coordinating Facility (ST-ECF/ESA) and the Canadian Astronomy Data Centre (CADC/NRC/CSA).

Bibliography

Aalto, S., Garcia-Burillo, S., Muller, S., et al., 2012, A&A, 537, A44

Alexander, D.M., Swinbank, A.M., Smail, I., McDermid, R., & Nesvadba, N.P.H., 2010, MNRAS, 402, 2211

Alonso-Herrero, A., Esquej, P., Roche, P.F., et al., 2016, MNRAS, 455, 563

Antonucci, R.R.J. & Miller, J.S., 1985, ApJ, 297, 621

Arribas, S., Colina, L., Bellocchi, E., Maiolino, R., & Villar-Martín, M., 2014, A&A, 568, A14

Banerji, M., Chapman, S.C., Smail, I., et al., 2011, MNRAS, 418, 1071

Barinovs, Ğ., van Hemert, M.C., Krems, R., & Dalgarno, A., 2005, ApJ, 620, 537

Bauer, F.E., Arevalo, P., Walton, D.J., et al., 2014, ArXiv e-prints

Bland-Hawthorn, J., Gallimore, J.F., Tacconi, L.J., et al., 1997, Ap&SS, 248, 9

Bolatto, A.D., Wolfire, M., & Leroy, A.K., 2013, ARA&A, 51, 207

Booth, C.M. & Schaye, J., 2009, MNRAS, 398, 53

Briggs, F.H., Sorar, E., Kraan-Korteweg, R.C., & van Driel, W., 1997, PASA, 14, 37

Bruderer, S., 2013, A&A, 559, A46

Bruderer, S., van Dishoeck, E.F., Doty, S.D., & Herczeg, G.J., 2012, A&A, 541, A91

Brüggen, M. & Scannapieco, E., 2016, ApJ, 822, 31

Burlon, D., Ajello, M., Greiner, J., et al., 2011, ApJ, 728, 58

Burton, W.B., Elmegreen, B.G., & Genzel, R., editors, 1992, *The galactic interstellar medium*

Cano-Díaz, M., Maiolino, R., Marconi, A., et al., 2012, A&A, 537, L8

Cecil, G., Bland, J., & Tully, R.B., 1990, ApJ, 355, 70

Cicone, C., Feruglio, C., Maiolino, R., et al., 2012, A&A, 543, A99

Cicone, C., Maiolino, R., Gallerani, S., et al., 2015, A&A, 574, A14

Cicone, C., Maiolino, R., Sturm, E., et al., 2014, A&A, 562, A21

Cole, S., 1991, ApJ, 367, 45

Condon, J.J., Huang, Z.P., Yin, Q.F., & Thuan, T.X., 1991, ApJ, 378, 65

Contursi, A., Poglitsch, A., Grácia Carpio, J., et al., 2013, A&A, 549, A118

Crain, R.A., Schaye, J., Bower, R.G., et al., 2015, MNRAS, 450, 1937

Diamond-Stanic, A.M., Moustakas, J., Tremonti, C.A., et al., 2012, ApJL, 755, L26

Draine, B.T., 2003, ARA&A, 41, 241

Dudley, C.C. & Wynn-Williams, C.G., 1997, ApJ, 488, 720

Dugan, Z., Gaibler, V., & Silk, J., 2016, ArXiv e-prints

Dyson, J.E., 1984, Ap&SS, 106, 181

Efstathiou, A., Pearson, C., Farrah, D., et al., 2014, MNRAS, 437, L16

Efstathiou, G., 2000, MNRAS, 317, 697

Elvis, M. & Lawrence, A., 1988, ApJ, 331, 161

Evans, A.S., Mazzarella, J.M., Surace, J.A., & Sanders, D.B., 2002, ApJ, 580, 749

Fabian, A.C., 2012, ARA&A, 50, 455

Farrah, D., Lebouteiller, V., Spoon, H.W.W., et al., 2013, ApJ, 776, 38

Faucher-Giguère, C.A. & Quataert, E., 2012, MNRAS, 425, 605

Feruglio, C., Fiore, F., Carniani, S., et al., 2015, A&A, 583, A99

Feruglio, C., Fiore, F., Maiolino, R., et al., 2013a, A&A, 549, A51

Feruglio, C., Fiore, F., Piconcelli, E., et al., 2013b, A&A, 558, A87

Feruglio, C., Maiolino, R., Piconcelli, E., et al., 2010, A&A, 518, L155

Fischer, J., Sturm, E., González-Alfonso, E., et al., 2010, A&A, 518, L41

Flower, D.R. & Pineau Des Forêts, G., 2010, MNRAS, 406, 1745

Förster Schreiber, N.M., Genzel, R., Newman, S.F., et al., 2014, ApJ, 787, 38

Fried, J.W. & Schulz, H., 1983, A&A, 118, 166

Gallimore, J.F., Baum, S.A., O'Dea, C.P., Brinks, E., & Pedlar, A., 1996, ApJ, 462, 740

Gallimore, J.F., Elitzur, M., Maiolino, R., et al., 2016, ApJL, 829, L7

García-Burillo, S., Combes, F., Ramos Almeida, C., et al., 2016, ApJL, 823, L12

García-Burillo, S., Combes, F., Usero, A., et al., 2015, A&A, 580, A35

García-Burillo, S., Usero, A., Fuente, A., et al., 2010, A&A, 519, A2

Gaspari, M., Ruszkowski, M., & Oh, S.P., 2013, MNRAS, 432, 3401

Geballe, T.R., Goto, M., Usuda, T., Oka, T., & McCall, B.J., 2006, ApJ, 644, 907

Genzel, R., Förster Schreiber, N.M., Rosario, D., et al., 2014, ApJ, 796, 7

Genzel, R., Lutz, D., Sturm, E., et al., 1998, ApJ, 498, 579

González-Alfonso, E., Fischer, J., Graciá-Carpio, J., et al., 2012, A&A, 541, A4

González-Alfonso, E., Fischer, J., Graciá-Carpio, J., et al., 2014, A&A, 561, A27

Hailey-Dunsheath, S., Sturm, E., Fischer, J., et al., 2012, ApJ, 755, 57

Häring, N. & Rix, H.W., 2004, ApJL, 604, L89

Harrison, C.M., Alexander, D.M., Mullaney, J.R., & Swinbank, A.M., 2014, MNRAS, 441, 3306

Harrison, C.M., Alexander, D.M., Swinbank, A.M., et al., 2012, MNRAS, 426, 1073

Heckman, T.M., Alexandroff, R.M., Borthakur, S., Overzier, R., & Leitherer, C., 2015, ApJ, 809, 147

Heckman, T.M. & Best, P.N., 2014, ARA&A, 52, 589

Heckman, T.M., Borthakur, S., Overzier, R., et al., 2011, ApJ, 730, 5

Herczeg, G.J., Karska, A., Bruderer, S., et al., 2012, A&A, 540, A84

Hickox, R.C., Mullaney, J.R., Alexander, D.M., et al., 2014, ApJ, 782, 9

Ho, L.C., 2008, ARA&A, 46, 475

Hönig, S.F., Beckert, T., Ohnaka, K., & Weigelt, G., 2006, A&A, 452, 459

Hopkins, P.F., Quataert, E., & Murray, N., 2012, MNRAS, 421, 3522

Hopkins, P.F., Torrey, P., Faucher-Giguère, C.A., Quataert, E., & Murray, N., 2016, MNRAS, 458, 816

Ishibashi, W. & Fabian, A.C., 2015, MNRAS, 451, 93

Iwasawa, K., Sanders, D.B., Teng, S.H., et al., 2011, A&A, 529, A106

Janssen, A.W., Christopher, N., Sturm, E., et al., 2016, ApJ, 822, 43

Kaufman, M.J. & Neufeld, D.A., 1996, ApJ, 456, 611

Keel, W.C., Chojnowski, S.D., Bennert, V.N., et al., 2012, MNRAS, 420, 878

Kennicutt, Jr., R.C., 1998, ARA&A, 36, 189

Kessler, M.F., Steinz, J.A., Anderegg, M.E., et al., 1996, A&A, 315, L27

King, A. & Nixon, C., 2015, MNRAS, 453, L46

Kormendy, J. & Ho, L.C., 2013, ARAA, 51, 511

Kreckel, K., Armus, L., Groves, B., et al., 2014, ApJ, 790, 26

Krips, M., Martín, S., Eckart, A., et al., 2011, ApJ, 736, 37

Krolik, J.H. & Begelman, M.C., 1988, ApJ, 329, 702

Krolik, J.H. & Lepp, S., 1989, ApJ, 347, 179

Lawson, P.R., editor, 2000, *Principles of Long Baseline Stellar Interferometry*

Lepp, S. & Dalgarno, A., 1996, A&A, 306, L21

Lindberg, J.E., Aalto, S., Muller, S., et al., 2016, A&A, 587, A15

López-Gonzaga, N., Jaffe, W., Burtscher, L., Tristram, K.R.W., & Meisenheimer, K., 2014, A&A, 565, A71

Lutz, D., Berta, S., Contursi, A., et al., 2015, ArXiv e-prints

Lutz, D., Berta, S., Contursi, A., et al., 2016, A&A, 591, A136

Maiolino, R., Gallerani, S., Neri, R., et al., 2012, MNRAS, 425, L66

Malizia, A., Stephen, J.B., Bassani, L., et al., 2009, MNRAS, 399, 944

Maloney, P.R., Hollenbach, D.J., & Tielens, A.G.G.M., 1996, ApJ, 466, 561

Marlowe, A.T., Heckman, T.M., Wyse, R.F.G., & Schommer, R., 1995, ApJ, 438, 563

Martin, C.L., 1998, ApJ, 506, 222

Martin, C.L., 2005, ApJ, 621, 227

Mashian, N., Sturm, E., Sternberg, A., et al., 2015, ApJ, 802, 81

McConnell, N.J. & Ma, C.P., 2013, ApJ, 764, 184

Meijerink, R. & Spaans, M., 2005, A&A, 436, 397

Meijerink, R., Spaans, M., & Israel, F.P., 2007, A&A, 461, 793

Morganti, R., Oosterloo, T., Oonk, J.B.R., Frieswijk, W., & Tadhunter, C., 2015, A&A, 580, A1

Morganti, R., Tadhunter, C.N., & Oosterloo, T.A., 2005, A&A, 444, L9

Morganti, R., Veilleux, S., Oosterloo, T., Teng, S.H., & Rupke, D., 2016, ArXiv e-prints

Müller Sánchez, F., Davies, R.I., Genzel, R., et al., 2009, ApJ, 691, 749

Murray, N., Quataert, E., & Thompson, T.A., 2005, ApJ, 618, 569

Naab, T., Oser, L., Emsellem, E., et al., 2014, MNRAS, 444, 3357

Nenkova, M., Ivezić, Ž., & Elitzur, M., 2002, ApJL, 570, L9

Nesvadba, N.P.H., Lehnert, M.D., De Breuck, C., Gilbert, A.M., & van Breugel, W., 2008, A&A, 491, 407

Nesvadba, N.P.H., Polletta, M., Lehnert, M.D., et al., 2011, MNRAS, 415, 2359

Netzer, H., 2013, *The Physics and Evolution of Active Galactic Nuclei*

Peterson, B.M., 1997, *An Introduction to Active Galactic Nuclei*

Pier, E.A., Antonucci, R., Hurt, T., Kriss, G., & Krolik, J., 1994, ApJ, 428, 124

Pilbratt, G.L., Riedinger, J.R., Passvogel, T., et al., 2010, aap, 518, L1

Pineda, J.L., Langer, W.D., Velusamy, T., & Goldsmith, P.F., 2013, A&A, 554, A103

Poglitsch, A., Waelkens, C., Geis, N., et al., 2010, aap, 518, L2

Rand, R.J., 1996, ApJ, 462, 712

Riechers, D.A., Carilli, C.L., Capak, P.L., et al., 2014, ApJ, 796, 84

Rodríguez Zaurín, J., Tadhunter, C.N., & González Delgado, R.M., 2009, MNRAS, 400, 1139

Röllig, M., Abel, N.P., Bell, T., et al., 2007, A&A, 467, 187

Rupke, D.S., Veilleux, S., & Sanders, D.B., 2005a, ApJ, 632, 751

Rupke, D.S., Veilleux, S., & Sanders, D.B., 2005b, ApJS, 160, 87

Rupke, D.S.N. & Veilleux, S., 2013a, ApJL, 775, L15

Rupke, D.S.N. & Veilleux, S., 2013b, ApJ, 768, 75

Ryter, C.E., 1996, Ap&SS, 236, 285

Sakamoto, K., Aalto, S., Wilner, D.J., et al., 2009, ApJL, 700, L104

Sales, L.V., Navarro, J.F., Schaye, J., et al., 2010, MNRAS, 409, 1541

Sanders, D.B., Mazzarella, J.M., Kim, D.C., Surace, J.A., & Soifer, B.T., 2003, AJ, 126, 1607

Sanders, D.B. & Mirabel, I.F., 1996, ARA&A, 34, 749

Scannapieco, E. & Brüggen, M., 2015, ApJ, 805, 158

Schawinski, K., Koss, M., Berney, S., & Sartori, L.F., 2015, MNRAS, 451, 2517

Schaye, J., Crain, R.A., Bower, R.G., et al., 2015, MNRAS, 446, 521

Schinnerer, E., Eckart, A., Tacconi, L.J., Genzel, R., & Downes, D., 2000, ApJ, 533, 850

Scoville, N.Z., Evans, A.S., Thompson, R., et al., 2000, AJ, 119, 991

Seyfert, C.K., 1943, ApJ, 97, 28

Shapiro, K.L., Genzel, R., Förster Schreiber, N.M., et al., 2008, ApJ, 682, 231-251

Shih, H.Y. & Rupke, D.S.N., 2010, ApJ, 724, 1430

Shirahata, M., Nakagawa, T., Usuda, T., et al., 2013, PASJ, 65

Silk, J., 2011, in C. Carignan, F. Combes, & K.C. Freeman, editors, *IAU Symposium*, volume 277 of *IAU Symposium*, 273–281

Soifer, B.T., Neugebauer, G., Matthews, K., et al., 2000, AJ, 119, 509

Solomon, P.M., Downes, D., Radford, S.J.E., & Barrett, J.W., 1997, ApJ, 478, 144

Solomon, P.M., Rivolo, A.R., Barrett, J., & Yahil, A., 1987, ApJ, 319, 730

Solomon, P.M. & Vanden Bout, P.A., 2005, ARA&A, 43, 677

Spinoglio, L., Pereira-Santaella, M., Busquet, G., et al., 2012, ApJ, 758, 108

Spoon, H.W.W., Farrah, D., Lebouteiller, V., et al., 2013, ApJ, 775, 127

Spoon, H.W.W. & Holt, J., 2009, ApJL, 702, L42

Spoon, H.W.W., Marshall, J.A., Houck, J.R., et al., 2007, ApJL, 654, L49

Springel, V., Di Matteo, T., & Hernquist, L., 2005, MNRAS, 361, 776

Sturm, E., González-Alfonso, E., Veilleux, S., et al., 2011a, ApJL, 733, L16

Sturm, E., Poglitsch, A., Contursi, A., et al., 2011b, in M. Röllig, R. Simon, V. Ossenkopf, & J. Stutzki, editors, *EAS Publications Series*, volume 52 of *EAS Publications Series*, 55–61

Surace, J.A., Sanders, D.B., & Evans, A.S., 2000, ApJ, 529, 170

Surace, J.A., Sanders, D.B., Vacca, W.D., Veilleux, S., & Mazzarella, J.M., 1998, ApJ, 492, 116

Tacconi, L.J., Genzel, R., Tecza, M., et al., 1999, ApJ, 524, 732

Teng, S.H., Rigby, J.R., Stern, D., et al., 2015, ApJ, 814, 56

Tielens, A.G.G.M., 2005, *The Physics and Chemistry of the Interstellar Medium*

Tielens, A.G.G.M. & Hollenbach, D., 1985, ApJ, 291, 722

Tombesi, F., Meléndez, M., Veilleux, S., et al., 2015, Nature, 519, 436

Usero, A., García-Burillo, S., Fuente, A., Martín-Pintado, J., & Rodríguez-Fernández, N.J., 2004, A&A, 419, 897

Veilleux, S., Kim, D.C., Sanders, D.B., Mazzarella, J.M., & Soifer, B.T., 1995, ApJS, 98, 171

Veilleux, S., Meléndez, M., Sturm, E., et al., 2013, ApJ, 776, 27

Veilleux, S., Rupke, D.S.N., Kim, D.C., et al., 2009a, ApJS, 182, 628

Veilleux, S., Rupke, D.S.N., & Swaters, R., 2009b, ApJL, 700, L149

Vogelsberger, M., Genel, S., Sijacki, D., et al., 2013, MNRAS, 436, 3031

Vogelsberger, M., Genel, S., Springel, V., et al., 2014, MNRAS, 444, 1518

Wall, J.V. & Jenkins, C.R., 2003, *Practical Statistics for Astronomers*

Weiner, B.J., Coil, A.L., Prochaska, J.X., et al., 2009, ApJ, 692, 187

Westmoquette, M.S., Clements, D.L., Bendo, G.J., & Khan, S.A., 2012, MNRAS, 424, 416

Westmoquette, M.S., Smith, L.J., Gallagher, J.S., & Walter, F., 2013, MNRAS, 428, 1743

Woltjer, L., 1959, ApJ, 130, 38

Yang, B., Stancil, P.C., Balakrishnan, N., & Forrey, R.C., 2010, ApJ, 718, 1062

Young, E.T., Becklin, E.E., Marcum, P.M., et al., 2012, ApJL, 749, L17

Yuan, T.T., Kewley, L.J., & Sanders, D.B., 2010, ApJ, 709, 884

Zenner, S. & Lenzen, R., 1993, A&AS, 101, 363

Zubovas, K. & King, A.R., 2014, MNRAS, 439, 400

Zubovas, K. & Nayakshin, S., 2014, MNRAS, 440, 2625

Abbreviations

AGN	Active Galactic Nucleus
ALMA	Atacama Large Millimeter Array
BH	Black Hole
BLR	Broad Line Region
BPT	Baldwin-Philips-Terlevich (diagram)
CND	Circumnuclear disk
ESA	European Space Agency
FIR	Far-infrared
FWHM	Full Width at Half Maximum
FWHP	Full Width at Half Power
HE	Highly excited (component)
HIPE	Herschel Interactive Processing Environment
HST	Hubble Space Telescope
IFU	Integral Field Unit
IRAM	Institut de radioastronomie millimétrique
IRAS	Infrared Astronomical Satellite
ISM	Interstellar Medium
ISO	Infrared Space Observatory
LINER	Low-Ionization Nuclear Emission-line Region galaxy
LVG	Large Velocity Gradient
ME	Moderately excited (component)
MIDI	Mid-infrared interferometric instrument
MIR	Mid-infrared
NIR	Near-infrared
NLR	Narrow Line Region
NOEMA	NOrthern Extended Millimeter Array
PACS	Photodetector Array Camera and Spectrometer
PDR	Photodissociation Region
PSF	Point Spread Function
SLED	Spectral Line Energy Distribution
SMA	Submillimeter Array
SMBH	Supermassive Black Hole
SOFIA	Stratospheric Observatory for Infrared Astronomy
ULIRG	Ultra Luminous Infrared Galaxy
UV	Ultraviolet
VLTI	Very Large Telescope Interferometer
XDR	X-ray Dominated Region

Acknowledgements